Glauber de Freitas Lima

A MODIFIED FLYBACK CONVERTER APPLIED IN CAPACITIVE POWER TRANSFER FOR ELECTRIC VEHICLE BATTERY CHARGER

Florianópolis
2019

Glauber de Freitas Lima

A MODIFIED FLYBACK CONVERTER APPLIED IN CAPACITIVE POWER TRANSFER FOR ELECTRIC VEHICLE BATTERY CHARGER

Dissertação submetida ao Programa de Pós-Graduação em Engenharia Elétrica da Universidade Federal de Santa Catarina para a obtenção do Grau de Mestre em Engenharia Elétrica.

Orientador: Prof. Dr. Ivo Barbi, Ing.

Florianópolis
2019

Glauber de Freitas Lima

A MODIFIED FLYBACK CONVERTER APPLIED IN CAPACITIVE POWER TRANSFER FOR ELECTRIC VEHICLE BATTERY CHARGER

Esta Dissertação foi julgada adequada para obtenção do Título de Mestre em Engenharia Elétrica e aprovada em sua forma final pelo Programa de Pós-Graduação em Engenharia Elétrica da Universidade Federal de Santa Catarina.

Florianópolis, 29 de março de 2019.

Prof. Bartolomeu Ferreira Uchoa-Filho, Dr.
Coordenador do Programa de Pós-Graduação
em Engenharia Elétrica
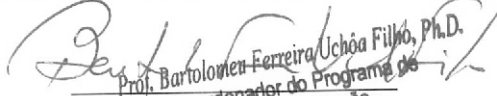
Banca Examinadora:

Prof. Ivo Barbi, Dr. Ing.
Orientador
Universidade Federal de Santa Cataria – UFSC
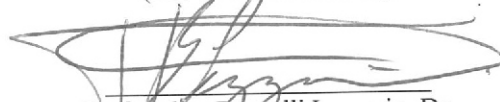
Prof. Ruben Barros Godoy, Dr.
Universidade Federal de Mato Grosso do Sul – UFMS
(Por videoconferência)

Prof. Telles Brunelli Lazzarin, Dr.
Universidade Federal de Santa Catarina – UFSC

Este trabalho é dedicado aos meus queridos pais.

AGRADECIMENTOS

"Eu não sou mais um ser humano, eu sou uma ideia". (Ex-presidente Luiz Inácio Lula da Silva, 2018)

RESUMO

Esta dissertação de mestrado apresenta a análise matemática, o dimensionamento, simulação e resultados experimentais de um Conversor Flyback Modificado (200 W), operando em Modo de Corrente Contínua (MCC), usando Transferência de Energia Capacitiva para implementação de um carregador de bateria sem fio especificado a um Veículo Elétrico (VE) de 58 V. O protótipo possui uma eficiência global de 86%, é comutado a 300 kHz e é composto por dois estágios: o primário, off-board, conectado à rede elétrica de 220 V; e o secundário, on-board, conectado à bateria. Estes estágios são acoplados por dois pares de placas metálicas de cobre (500 mm x 500 mm) distanciados através de uma camada de fibra de vidro com espessura de 1,5 mm, que atuam como capacitâncias de acoplamento entre os dois estágios na ordem de *nanofarads* (nF). O ganho estático encontrado, que não negligencia ondulações de tensão ou corrente, juntamente com a característica de carga, foram importantes para precisamente limitar e entender regiões de operação não tão comuns na literatura, causadas pelo baixo acoplamento capacitivo que resulta em uma alta excursão de tensão e uma elevada frequência de ressonância pelo circuito. De fato, o estudo é válido ou pode ser facilmente adaptado para qualquer conversor PWM clássico de quarta ordem, e, portanto, discussões fundamentais e significantes podem surgir.

Palavras-chave: Carregador de Bateria. Conversor Flyback Modificado. Transferência de Energia sem Fio. Transferência de Energia Capacitiva. Veículo Elétrico.

RESUMO EXPANDIDO

Introdução

Questões e desafios importantes sobre veículos tradicionais e elétricos são abordadas, tais como autonomia e eficiência energética. A implementação de um carregador com transferência de energia sem fio (*Wireless Power Transfer* – WPT) é então proposta como uma forma de motivar o uso e a pesquisa de veículos elétricos, bem como eletromobilidade.

Objetivos

Revisar e avaliar os sistemas por acoplamento capacitivo (*Capacitive Power Transfer* – CPT) e propor uma análise orientada a projeto de um conversor Flyback Modificado, operando em Modo de Condução Contínuo (MCC) e aplicado em um sistema CPT, destacando suas principais características e peculiaridades, como ganho estático e característica de carga. Outro objetivo a ser cumprido nesta dissertação é o de divulgar e incentivar mais linhas de pesquisas na área WPT, mostrando sua importância à sociedade.

Metodologia

A estrutura do banco de baterias do Twizy é modelada para definir as especificações do conversor proposto. São em seguida descritas algumas aplicações e conceitos básicos sobre WPT, e uma breve revisão teórica do campo elétrico associado à capacitância de placas metálicas é apresentada. A partir de uma revisão bibliográfica, as principais topologias e conversores aplicados em *CPT* são descritos e comparados. Com o projeto topológico e o design das placas metálicas definidos, é feita uma análise orientada ao projeto do conversor CC-CC. O dimensionamento de todos os elementos é detalhadamente descrito nesta dissertação. Para se obter frequência de comutação elevada, é construído um *gate driver*, cujo os resultados e dimensionamento é apresentado em apêndice. É construído um protótipo que possui as seguintes especificações: conectado à rede elétrica de 220 V, potência de 200 W, frequência de comutação de 300 kHz, capacitância de acoplamento na ordem de *nanofarads* (nF), distanciamento entre as placas na ordem milimétrica (mm) e eficiência global de 86%. Os resultados obtidos são apresentados ao final.

Resultados e Discussão

São apresentadas as características e dimensionamento de conversor Flyback CC-CC modificado para transferência de energia sem fio (*WPT*) através de transferência de energia por acoplamento capacitivo (*CPT*)

com grampeamento passivo. É verificado que frequências de comutação elevadas são fundamentais para vencer a impedância provocada pela baixa capacitância dos capacitores de acoplamento. Além disso, conclui-se que as tensões de entrada e saída refletidas ao capacitor de acoplamento do conversor devem também se manter elevadas para haver maior transferência de energia. Além disso, é verificado que o baixo acoplamento capacitivo, naturalmente esperado de um sistema *CPT*, resulta em frequências de ressonâncias pelo circuito comparadas à frequência de comutação; e um alta execurção da tensão pelo circuito que, consequentemente, é refletida aos elementos comutadores. Por esse motivo, o ganho estático convencional encontrado na literatura, que negligencia as ondulações de tensão e corrente no capacitor de acoplamento, não é adequado e uma nova abordagem é proposta. Outra consequência da baixa capacitância é o surgimento de dois modos de operação incomuns, devido a descontinuidade da tensão no diodo. A principal contribuição para a literatura é a seguinte: uma análise da característica de carga de todos os modos de operação do conversor contida na mesma corrente média de saída parametrizada. A topologia, ganho estático, característica de carga e limite entre modos de operação não tão comuns, como por exemplo o modo discontínuo quasi-ressonante, são apresentados. Os resultados finais dos experimentos mostram que as formas de onda e cálculos teóricos representam os efeitos físicos na prática e que o dimensionamento foi adequado.

Considerações Finais
Trabalhos futuros e propostos incluem elevar a frequência e, consequentemente, diminuir a ordem de grandeza do acoplamento capacitivo para *picofarads* (pF), aumentando assim o distanciamento das placas para a ordem de centímetros (cm); fazer uso de técnica de grampeamento ativo, realização de comutação suave através de métodos convencionais e, ou, através dos modos de operação diferentes do CCM. Em se tratando de conversores PWM, buscar arquiteturas com alto ganho, uma vez que é comprovada teoricamente a elevação da potência máxima permitida. Além disso, propõe-se o uso de conversores que não seja o uso do transformador Flyback para adequação de ganho, controle de potência no estágio secundário e realizar PFC. No campo teórico, analisar com mais detalhes os outros modos de operação, equacionando valores máximos, mínimos e eficazes, e, inclusive, utilizando o mesmo plano da corrente parametrizadas mostrada nesta dissertação. Aliar estes conceitos à inclusão de resistências série equivalente e entre outras perdas para gerar curvas de eficiência conforme a variação de parâmetros, de modo

que se faça uma metodologia de otimização baseada em eficiência, separação, acoplamento das placas e capacidade de transferência de energia.

Palavras-chave: Carregador de Bateria. Conversor Flyback Modificado. Transferência de Energia sem Fio. Transferência de Energia Capacitiva. Veículo Elétrico.

ABSTRACT

This master's thesis presents the mathematical analysis, sizing, simulation and experimental results of a 200 W Modified Flyback Converter operating in Continuous Current Mode (CCM) applied in Capacitive Power Transfer (CPT) for wireless battery charging implementation, specified for a 58 V Electric Vehicle (EV). The prototype has an overall efficiency of 86%, it is switched at 300 kHz and it is comprised of 2 stages: off-board primary grid-connected (220V); and an on-board secondary battery-connected. These stages are coupled by two pair of copper metal plates (500 mm x 500 mm) separated through a 1.5 mm fiberglass layer, which act as coupling capacitances between the two stages in the order of nanofarads (nF). The found static gain that does not neglect neither voltage or current ripples, along with load characteristic, were important to precisely limit and understand regions of operation not so common in the literature, caused by the low capacitive coupling which results in large voltage excursion and high resonant frequency throughout the circuit. Indeed, such study is valid or may easily be adapted to any classical fourth order PWM converter, and, therefore, further significant fundamental discussions may arise.

Keywords: Battery Charger. Capacitive Power Transfer (CPT). Electric Vehicle. Modified Flyback Converter. Wireless Power Transfer (WPT).

FIGURE LIST

TABLE LIST

ABREVIATION AND INITIAL LIST

BEM	Boundary Element Method
CCM	Continuous Current Mode
CNPq	*Conselho Nacional de Pesquisa*
CPL	Constant Power Load
CPT	Capacitive Power Transfer
DVM	Discontinuous Voltage Mode
DQRM	Discontinuous Quasi-resonant Mode
DWPT	Dynamic Wireless Power Transfer
EMI	Electromagnetic Interference
ESR	Electric Series Resistance
EV	Electric Vehicle
IEA	International Energy Agency
IPT	Inductive Power Transfer
IEEE	Institute of Electrical and Electronics Engineers
KAIST	Korea University Advanced Institute of Science and Technology
MOSFET	Metal-Oxide Semiconductor Field Effect Transistor
OLEV	Online Electric Vehicle
PATH	The Partner for Advanced Transit and Highways
PFC	Power Factor Correction
PWM	Pulse Width Modulation
R&D	Research and Development
RMS	Root mean square
SoC	State of Charge
SiC	Silicon Carbide
THD	Total Harmonic Distortion
UFSC	Universidade Federal de Santa Catarina
WPT	Wireless Power Transfer
ZCS	Zero Current Switching
ZVS	Zero Voltage Switching

SYMBOL LIST

A	Surface area
$\vec{E}$	Electric field
L_1	Primary magnetizing inductance
L_2	Secondary magnetizing inductance
L_{eq}	Equivalent inductance between
C	Equivalent coupling capacitance
C_1	Coupling capacitance "1"
C_2	Coupling capacitance "2"
D	Duty cycle
d	Distance
I_o	Output current
I_o^*	Reflected output current
μ_1	Ratio of switching angular frequency and primary resonance
μ_2	Ratio of switching angular frequency and secondary resonance
ω_1	Primary resonance frequency
ω_2	Secondary resonance frequency
f_s	Switching frequency
n	Turns ratio
P	Output power
P_{max}	Maximum theoretical power
P_{min}	Minimum theoretical power
R_o	Load resistance
R_o^*	Reflected load resistance
t	Time
Δt	Time interval
V_i	Input voltage
V_o	Output voltage
V_o^*	Reflected output voltage
V_{C_M}	Maximum initial condition voltage across the capacitor
V_{C_m}	Minimum initial condition voltage across the capacitor

V_{S_M}	Maximum voltage across the switch
V_{S_m}	Minimum voltage across the switch
$V_{D_M}^*$	Maximum reflected voltage across the diode
$I_{L_{1M}}$	Maximum initial condition current in L_1
$I_{L_{1m}}$	Minimum initial condition current in L_1
$I_{L_{2M}}$	Maximum initial condition current in L_2
$I_{L_{2m}}$	Minimum initial condition current in L_2
$V_{D_{FWD}}$	Diode forward voltage drop
Q_{Bat}	Capacity of the battery
σ	Charge density
ε_o	Electric permittivity in vacuum
ε_r	Electric permittivity in the medium
σ	Charge density
G_{CCM}	Static gain in CCM
G_{DCM}	Static gain in DCM
G_{DVM}	Static gain in DVM
k_E	Capacitive coupling coefficient

SUMMARY

1 INTRODUCTION

This chapter presents a contextualization of electric vehicles and wireless power transfer regarding its importance towards electric mobility and sustainability.

1.1 Contextualization

Globally, transport accounted for **25%** of total **CO_2** emission in 2016, around $8GtCO_2$, 71% larger than in 1990 [IEA, 2018]. As shown in Figure 1.1 (a), in the Americas, transport was the largest emitting sector, accounting for 36% of total emissions. Specifically, it reached **48%** in Brazil, totalizing up to 8% of the total transport emission in the continent, while USA accounts for more than 66%. As it can be seen in Figure 1.1 (b), transport **on roads** corresponds to more than **70%** of the global transport CO_2 emission.

Figure 1.1 – IEA data: (a) CO_2 emissions by sector for selected regions, 2016; (b) Global transport CO_2 emissions by subsectors.
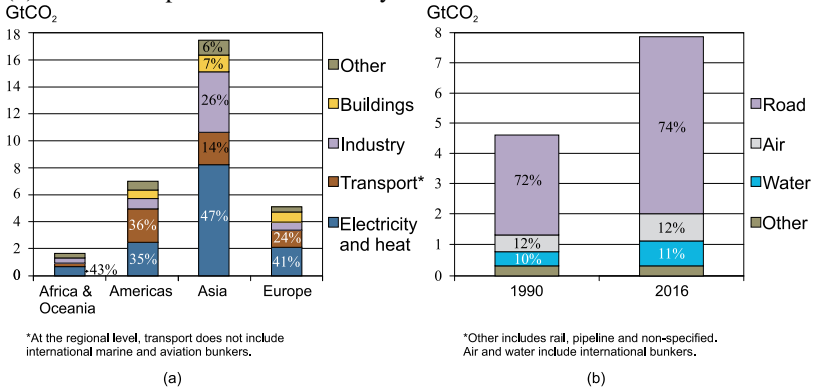
Source: Adapted from [IEA, 2018].

It is well known that conventional vehicles are not only highly **polluting** but also very **inefficient**. Considering the Otto cycle, only 30% of the fuel's chemistry energy is converted into kinetic energy, being worsen for low rotation (5% to 10%) and averaging 15% in an urban scenario. In general, efficiency of the best engines is quite low (<50%), as presented in Figure 1.2, and there is not much that new heat engine technologies can do about it. Obtaining energy from temperature is **tough**, and it is highly associated with the concept of **entropy**.

Figure 1.2 – Thermal energy efficiency.
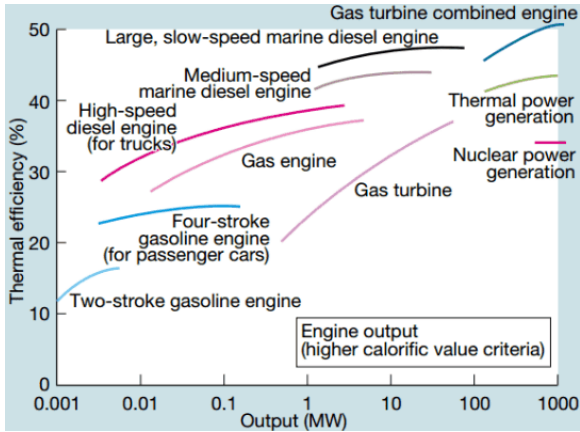
Source: [1].

For example, **electricity** is highly ordered and, therefore, presents very low entropy which enables electric energy to be converted into other forms of energy very **efficiently** (about 90% in electric motors, being relatively constant for any rotation, as presented in Figure 1.3), as opposed to thermal energy. Thus, these features confirm that an electric engine is from **30%** to **40%** more efficient than a combustion engine in the current scenario.

Figure 1.3 – Efficiency of a three-phase induction motor.
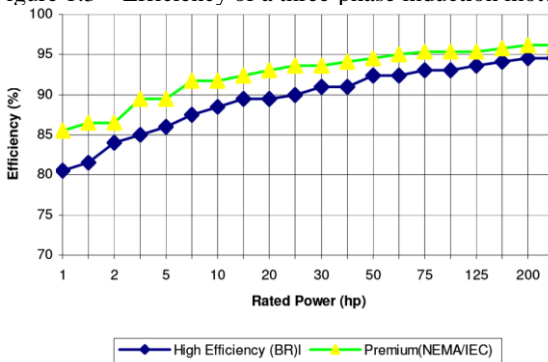
Source: [2].

Another advantage of EVs are their **regenerative breaking**, a straightforward technology able to transform the loss of kinetic energy during a breaking into electric power, making it ideal for urban transport.

According to [3], hypothetically considering a certain scenario in Brazil of mass adoption of pure or hybrid EVs, it would result in a **41%** reduction in gasoline consumption by 2031, accompanied by an increase in electricity consumption of **42.1%** larger than the official projection, bringing energetic efficiency by reducing **27.5%** of Brazilian fleet's energy consumption. It is also affirmed that such scenario is only possible to reach if **public polices**, currently almost **inexistent** in Brazil, of reinforcement of EVs, pure or hybrid were adopted, as with ethanol and flex fuel automotive technologies that were once successfully adopted in Brazil.

Therefore, given a privileged **renewable energy source** as found in Brazil and increasingly growing, the use of EVs would play a key role in mitigating the emission of harmful gases. This would be one of the major factors for strengthening interest in the use of EVs, both from the costumer as well as automotive industry sides.

However, EVs do not have the same practicality as its **energy storage** and **charging time** are limited when compared to traditional fleet, since battery technologies have not evolved enough to follow the required demand.

The **stored energy** in gasoline is about 12 kWh/kg, whereas the energy density found currently in a **lithium-ion** battery pack is about 100-150Wh/kg [4]. Therefore, the energy density found in a fuel car is **one hundred** times larger than in EVs. Considering the energy efficiency, the usable ratio drops to nearly **five**, still a large amount of volume and weight to overcome. Although the technology of energy storage devices and their recharges are evolving at great strides, such as lithium-air (400-500 Wh/Kg [4]), which uses air oxygen for chemical reaction [5], the price embedded in them would continue to be a major bottleneck in expanding the use of EVs.

Therefore, its low energy density and longtime charging causes EV cost and autonomy way less attractive than traditional fleets. Thus, the success of its real popularization will only be achieved thorough parallel technologies that increase its viability, autonomy, practicality and are still efficient. In this context, **wireless power transfer (WPT)** is an important factor to facilitate the expansion and adoption of EVs. The development of a wireless battery charging system can result in an autonomous, safe and human-free charging, reducing the risk of accidents and increasing convenience [6].

Regarding wireless power transfer, the only type found commercially in EVs is the loosely coupled **inductive** type. This is a very mature and leading technology, with overall efficiency (from grid to battery) reaching impressively 94% [WiTricity, 2016]. However, much of its drawback is related to **cost, volume and weight** (requires Ferrite core and Litz wire), **EMI** and is greatly affected by **metal proximity**, due to the presence eddy currents, which decreases its efficiency and puts in danger the vicinity by increasing surrounding temperature.

A relatively new line of research can overcome the challenges faced by inductive types. It consists in the use of **capacitive power transfe**r **(CPT),** as presented in Figure 1.4, that is, by means of electric field, instead of magnetic field. As it will be demonstrated through this master's thesis, a high-performance CPT for EV charging and industrial application is able to yet gain market.

The project in this master's thesis is supported and funded by **ENGIE** company as part of the project R&D021 of the Brazilian Electricity Regulatory Agency (**ANEEL**) and it is also supported by the Brazilian National Council for Scientific and Technological Development (**CNPq**).

Figure 1.4 – Diagram concept of a WPT charging through CPT.
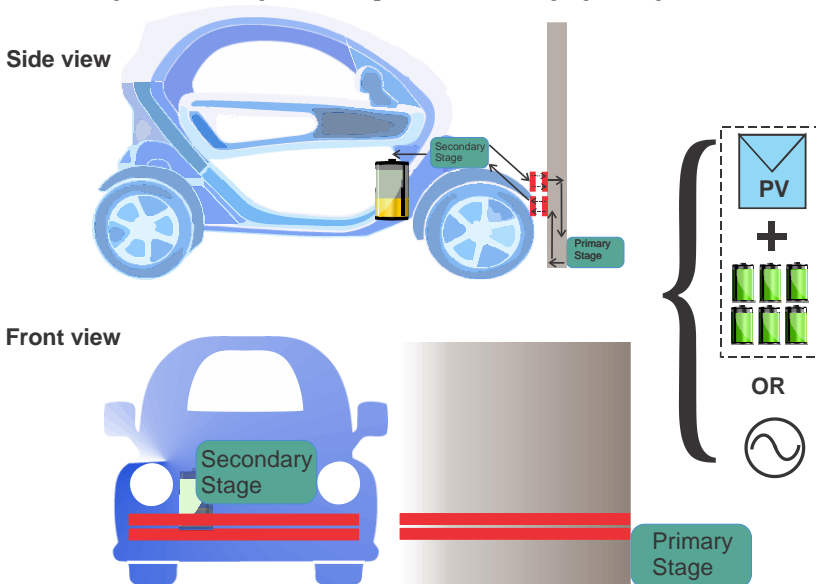
Source: Own elaboration.

1.2 Objectives

This master's thesis aims to present the conception, mathematical analysis, sizing, simulation and experimental results of a 200 W modified Flyback converter applied in capacitive wireless power transfer (CPT) system for battery charging implementation specified for the EV Renault Twizy, available for R&D purposes at the Solar Energy Research Laboratory (Fotovoltaica) at Federal University of Santa Catarina.

1.2.1 General objective

Design-oriented analysis of a modified Flyback converter applied in capacitive power transfer.

1.2.2 Specific objectives

- To review and evaluate CPT systems;
- To disclose and encourage more WPT lines of research and its importance towards society;
- Integration and selection of the CPT topology;
- Sizing and definition of the desired parameters, such as frequency, voltage and air-gap;
- Modeling and simulation of the converter;
- Prototyping the converter.

1.3 Scope of this Thesis

Structure of this dissertation is comprised of 9 chapters at total and 13 Appendixes. In this current Chapter 1, important issues regarding traditional and electrical vehicles have been addressed. The WPT implementation is then proposed as a way of motivating the use and research about EVs.

In Chapter 2, a brief view is made regarding EVs and its battery charging systems so as to introduce the main specification of the Twizy and its battery charger. The Twizy Battery pack is modeled and from this information the proposed converter will be specified accordingly.

In Chapter 3, the main general WPT topics are covered, but mainly CPT system are detailed. A brief historical context is presented and subsequently, the main modern trends and applications are depicted.

In Chapter 4, the electric field and capacitance theories are explained. The final sections of this chapter describe the modelling and understanding of a CPT system.

In Chapter 5, a general review on the literature of converters applied in CPT is covered, presenting their main advantage, disadvantages and features.

In Chapter 6, it is presented the modified DC-DC Flyback converter meant for wireless power transfer (WPT) through capacitive power transfer (CPT). The main contributions to the literatures are found in this chapter: an analysis of the converter contained in the same parametrized output load current. The topology, static gain, load characteristic and boundary between not so common modes of operation are presented and proved through simulation.

In Chapter 7 the sizing and designing criteria is detailly presented. Important equations to size the components are presented. Subsequentially, it is presented an open-loop simulation and compared with calculated values.

In Chapter 8, it is presented the experimental results of the converter, validating in practice the theory presented in previous chapters.

In Chapter 9, the main conclusions are summarized and futures studies are proposed.

2 EV TWIZY AND BATTERY CHARGER

In this Chapter, current and future scenario regarding EVs and its battery charging systems are briefly presented so as to introduce the main features of the Twizy and its battery charger.

2.1 EVs and battery charger systems: a brief overview

Despite the constraints of an EV presented in Chapter 1, the current scenario of the EVs is already viable in some countries and promising great expansion in the world market, even if still far from dominant. According to [7], the battery pack corresponds to nearly 50% of the entire vehicle costs. As presented in [8], the costs of a lithium battery are decreasing rapidly from more than $1000/kWh in 2010, to $200-300/kWh in 2016 and estimated as less than $100/kWh in 2030. The modelling of the total cost of ownership presented in [8] have shown that by 2035, EVs will cost less than conventional vehicles. Besides, it is shown that the EV market also attends costumers worried about acceleration, instant torque and overall power performances, as it already overcomes conventional engines at same costs.

It is important to emphasize that the acquisition of EVs is seen not only as a mere exchange between the conventional and the electric vehicles, but also as a solid investment. Data from the US Department of Energy present some reasons: (i) the price of electricity is 50% cheaper than gasoline, even considering the history of oil volatility. In addition, electricity prices are more stable, helping to keep costs predictable and easier to maintain your budget; (ii) additional discount of the electric energy is foreseen, in order to encourage the use in nocturnal and out-of-point schedules; (iii) in general, purely EVs require less maintenance, as there are fewer fluids (such as oil and transmission fluid) to exchange as well as fewer moving parts, such as the regenerative brake system lasts longer than a conventional brake system; and (iv) the initial tax incentive of US federal and state governments helps lowering the high price of EV acquisition.

The electric vehicles can be characterized as:

- Battery Electric Vehicles (BEV), are usually referred as simply EVs and are fully-electric vehicles with rechargeable batteries;
- Plug-in Hybrid Electric Vehicles (PHEV), have both combustion and electric engines. The batteries are

recharged through plugging in an external electrical power source or regenerative braking;

- Hybrid Electric Vehicles (HEV), have both combustion and electric engines. However, they cannot be recharged electrically through external power source. The recharging process is performed through regenerative braking system.
- Fuel Cell Electric Vehicles (FCEV), use hydrogen, oxygen and electrolyte to convert chemistry energy into electric energy.

According to [4], EVs can also be featured in size and autonomy (A: very small cars; B: small cars; C: medium cars; D: upper-medium cars; E: executive cars; F: luxury cars; S: sport cars; M: multi-purpose vehicles; J: sport utility vehicles (SUVs)). For BEVs, the small (A) and very small types (B) is the most common segment. Therefore, these pure EV types range at maximum 150 km to 200 km.

In order to supply the already large demand in USA, consumers and fleets need access to electric charging stations, also known as EVSE (Electric Vehicle Supply Equipment). According to the American department, the chargers are standardized in 3 types, or levels: AC Level 1 Charging, AC Level 2 Charging and DC Fast Charging:

- The Level 1 charger provides charging from 120 V AC voltage and 15-20 A dedicated circuit. They are commonly used residentially at night or at workplaces and can deliver 3.2 km to 8 km of range per hour of charging.
- Level 2 types can also be used at home with 208/240 V AC. However, because they have the option of operating at up to 19.2 kW, they require dedicated circuit of up to 80 A. They are commonly used as public charging stations and can deliver 16 km to 32 km or range per hour of charging.
- DC Fast types, despite the abbreviation DC in reference to direct current, it requires alternating three-phase voltage of 480 V as power supply. These chargers feature impressive charging times, delivering 96.5 km to 129 km of range in 20 minutes of charging. They are mostly used in public charging stations, nearby of heavy traffic corridors.

The chargers are also specified as on-board or off-board. On-board chargers are simply plugged in to the grid and power is limited due to size and weight. On the other hand, off-board chargers are outside of the vehicle and are intendent for higher power, such as the DC fast charging system.

The US Department website has an interactive map showing 24,847 public power stations in the country [9]. It is possible to simulate routes that display the available stations. As an example, a route was simulated between Los Angeles and New York, totalizing 1264 charging stations along the route.

Figure 2.1 – 1264 EV charging stations across L.A-NY route.

Source: [9].

Popular measures are being taken to promote marketing, such as, the company Nissan, which announced under the motto "no charge to charge" that in certain regions in USA, owners of the purely electric Nissan LEAF car would have for two-year free recharging at their DC Fast charging stations. Moreover, government incentives are also being taken in developed countries, such as USA [10] and Europe [11]. Such facts confirm that electric vehicles are, in fact, becoming increasingly the final choice of the consumer.

In Brazil, some incentive to expand EV's culture are being introduced. Such as, the Smart Electric Mobility Program (Mob-i) launched in 2014, a joint program between Itaipu Binacional, Renault and Ceiia [12] created to develop technologies to support a new generation of electric urban mobility. Thanks to this program, a Renault Twizy was ceded to the Fotovoltaica/UFSC Solar Energy Research Laboratory at Universidade Federal de Santa Catarina.

As it can be seen, the charging of EVs is being performed mostly through conventional and, therefore, contact stations. However, they do

not meet the expectation of demanding users who are concerned with greater practicality and security.

2.2 EV Twizy

The Twizy, shown in Figure 2.2, is a compact (class A) two-seater (one seat in front and one in the back) and reliable urban BEV. It has been manufactured by Renault since 2012. General specification provided by owner manual [13] are presented in Table I and Table II. Due to its size, it is also classified as a heavy quadricycle. In general, the Renault Twizy is commercially available in Europe with costs starting from 6,990 €.

Figure 2.2 – Renault Twizy representation with Mob-i logo.
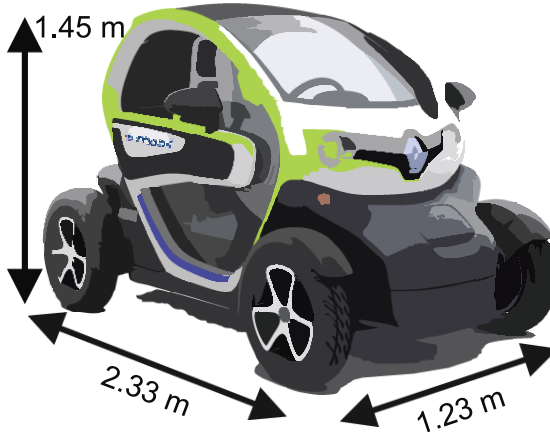
Source: Own elaboration.

Table I – Physical and general specification of the Twizy.

Specification	Value
Height	1.45 m
Length	2.33 m
Width	1.23 m
Total weight	474 kg
Maximum	80 km/h
Range	90 km

Table II – Twizy electric specifications.

Specification	Value/Type
Battery type	Lithium-ion
Battery weight	100 kg
Capacity	6.1 kWh
Charging time	3.5 h
Grid voltage	220 V
Slow charge	10 A
Battery voltage	58 V

The rated power of the converter, considering 220 V rms and 10 A rms from grid, can be estimated as 2200 W. Indeed, Twizy charger is an ELIPS 2000 W Charger converter, as shown in Figure 2.3, whereas Motor is controlled by a SEVCON AC controller, presented in Figure 2.4.

Figure 2.3 – ELIPS 2000 W Charger converter.

Source: [www.ies-synergy.com].

Figure 2.4– SEVCON AC controller.

Source: [http://www.sevcon.com].

2.3 Twizy Battery

This section is divided into two subsections: The first, describes and presents the main advantages and features of the Twizy lithium-ion battery; the second, presents the estimated modeling of the battery pack used in Twizy.

2.3.1 Twizy Lithium-ion battery

The Twizy battery pack is provided by LG Chem company, a leading global automobile battery supplier, such as Ford Focus, Renault Zoe and GM Bolt.

The LG Chem polymer electrode/lamination is the simplest structure, as presented in Figure 2.5. Notice that voltage range of this structure still maintains a well-known lithium-ion voltage characteristic, that is, from approximately 3.0 V to 4.2 V, as shown in Figure 2.6

Figure 2.5 – LG Chem polymer electrode.

Source: [LG Chem, 2019].

Figure 2.6 – Typical charging of a lithium-ion battery using CC-CV methods.
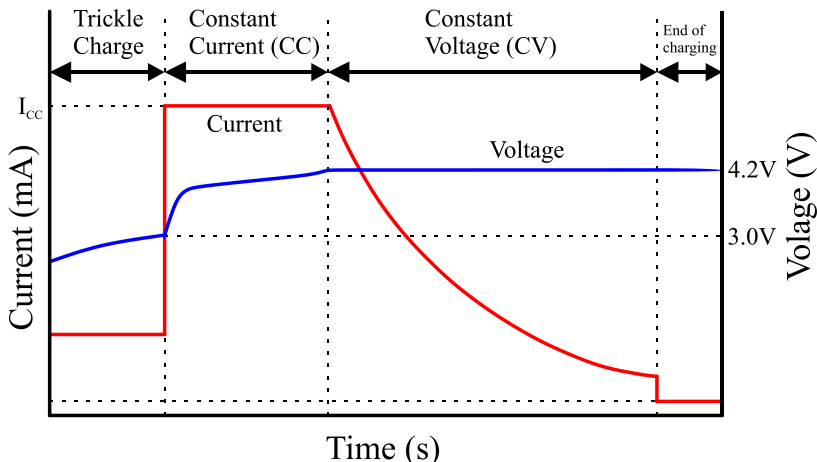
Source: Adapted from [14].

The LG Chem polymer cell is composed of a 'Stack & Folding' structure from the LG Chem polymer electrodes, as presented in Figure 2.7. This is a differentiated solution and increases compactness with respect to conventional winding polymer structures. Theses polymer electrodes are folded and sized until a desired capacity (Ah) is reached.

Figure 2.7– LG Chem's patented 'Stack & Folding' structure.
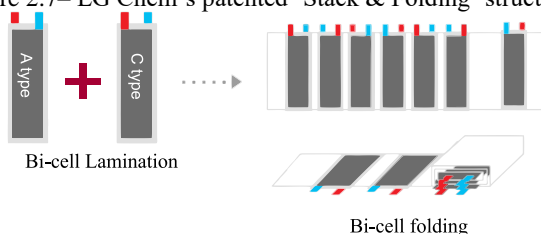
Source: Adapted from [LG Chem, 2019].

From the electrode size, passing through the cell design until the pack structure, the battery design is optimized for different automobile manufacturers, presenting a highly critical design flexibility, as presented in Figure 2.8.

Figure 2.8 – LG Chem Battery design flexibility.
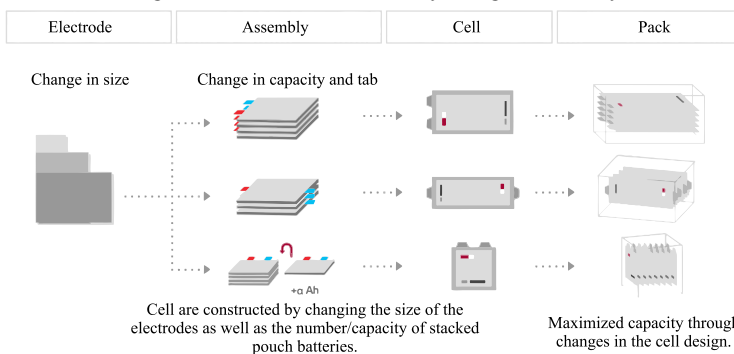
Source: Adapted from [LG Chem, 2019].

Modeling the state of energy in a battery is crucial for the energy management and performance optimization. The high degree of flexibility in the cell level makes its challenging to find exact and official information about the capacity of a single cell and number of modules or packs contained in a given EV supplied by LG Chem. According to [15], the Twizy battery pack consists of 42 cells, arranged in 7 modules each with 6 lithium cells (2 serial blocks each containing 3 cells fitted in parallel – 2S3P), as presented in Figure 2.9 Each cell contains a total capacity of 43 Ah. To validate and confirm this information, this configuration will be modeled and compared to official data.

Figure 2.9 – Estimated Twizy battery pack assembly.
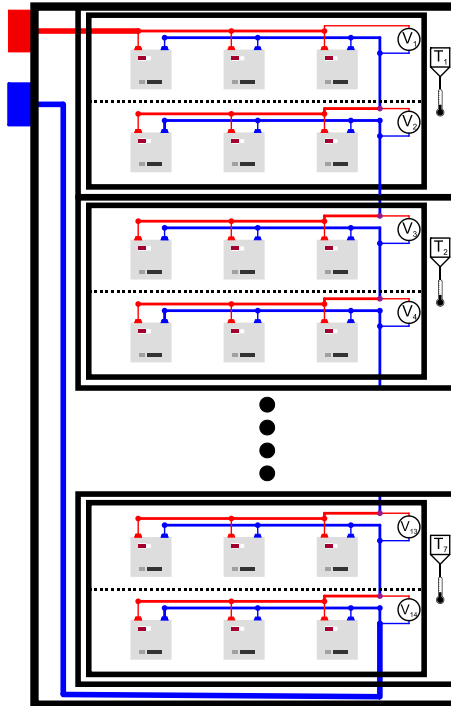
Source: Own elaboration.

In a lithium-ion battery pack, it is of great importance regarding safety and durability to measure and control voltage and temperature levels in the cells. However, there is a compromising between detailed output information and cost. Therefore, the measurements are performed in a group of cells. As shown in Figure 2.9 – Estimated Twizy battery pack assembly., for the Twizy's LG Chem battery pack, 14 voltage measurements are collected (one for each parallel string – 2 for each module) and 7 temperature measurements are collected (1 for each module).

Notice that voltage measurement at the level of each string of cells are enough, since there is a natural self-balancing tendency, whereas serial cells are critical and require either passive or active balancing [16]. Therefore, considering same energy, relatively low battery voltage levels (< 60 V) are not only safer, but also easier and cheaper to manage, when compared to high battery level, such as 384V found in the Nissan Leaf.

It is presented in Table III and Table IV, respectively, the estimated voltage and capacity values at each level of the Twizy battery pack.

Table III – Estimated voltage configuration.

Voltage	V_{min}	$V_{minSafe}$	V_{nom}	$V_{maxSafe}$	V_{max}
Cell	2.75 V	3.28 V	3.75 V	4.13 V	4.3 V
Module	5.5 V	6.56 V	7.50 V	8.26 V	8.6 V
Pack	38.5 V	45.92 V	52.50 V	57.82 V	60.2 V

Table IV– Estimated capacity configuration.

Level	Cell level	Module level	Battery level
Full Capacity	43 Ah	129 Ah	129 Ah
Full Energy	161.25 Wh	967.5 kWh	6.77 kWh
Usable Capacity	38.70 Ah	116.1 Ah	116.1 Ah
Usable Energy	145.12 Wh	870.75 Wh	6.10 kWh

2.3.2 Twizy battery pack modeling

According to [15], the charging process of a Twizy battery consists of two sections, the "CC" (constant current) until SoC reaches 94%, taking about 180 minutes long always followed by the "CV" (constant voltage) which takes about 40 minutes. In the CC mode, the charge speed is mostly linear, whereas in CV mode, it is non-linear and slow. It is worth mentioning that other external factors will interfere in the charging process, e.g., temperature, unbalanced cells and state of health, according to the BMS. The State of Charge (SoC) can be approximately defined by (2.1), as presented in Figure 2.10.

$$SoC(t) = SoC_o + \frac{I_{bat}}{Q_{bat}} t \qquad (2.1)$$

Where:

- SoC_o is the initial state of charge;
- I_{bat} is the constant current (CC) value (A);
- Q_{bat} is capacity of the battery (Ah).

Figure 2.10 – Estimated Twizy Battery SoC for 36 A charging.
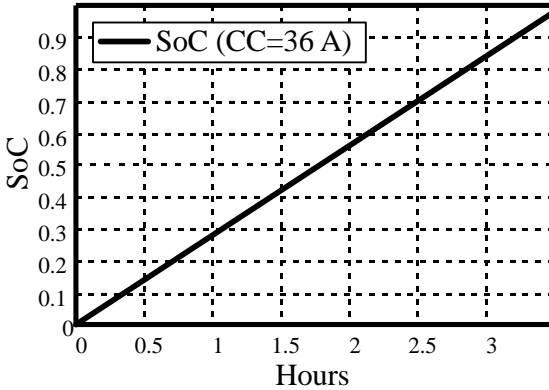
Source: Own elaboration.

There are many electrical equivalent circuits to represent the electrical and chemical interaction in a lithium-ion battery. When dealing with electrical engineering subjects, purely electrical models are intuitive and time-saving. The dual polarization equivalent circuit, presented in [17] is accurate, presenting the best tradeoff between accuracy and complexity and relatively easy way to model a lithium-ion battery. Therefore, this equivalent circuit will be used to model the Twizy battery pack. According to [17], the error is kept within 1 mV for all the curve fittings.

This equivalent circuit, presented in Figure 2.11, adds another RC pair to its simpler version, Thevenin model, in order to consider the dynamic in the final moments of complete charge and discharge.

Figure 2.11 – Dual polarization equivalent circuit
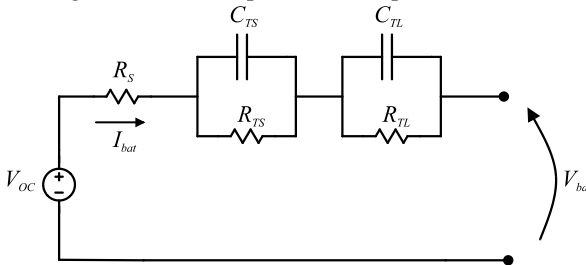
Source: Adapted from [17].

Where:

- V_{OC} is the internal open circuit voltage (V);

- V_{bat} is the terminal voltage (V);
- R_S is the series resistance responsible for instantaneous voltage drop of the step response (Ω);
- $R_{TS}C_{TS}$ is responsible for modeling short-time constant (s);
- $R_{TL}C_{TL}$ is responsible for modeling long-time constant (s).

These parameters are non-linear dependent on the SoC, current, temperature and cycle number, but can mostly be approximated as functions of the SoC. In [17], ten new 850 mAh TCL PL-383562 polymer Li-ion batteries were tested, from which the following averaged functions were extracted:

$$
\begin{aligned}
V_{OC}(SoC) = &-1.031e^{-35SoC} + 3,685 + 0.2156SoC \\
&- 0.1178SoC^2 + 0,3201SoC^3
\end{aligned}
\tag{2.2}
$$

$$
R_S(SoC) = 0.3208e^{-29.14SoC} + 0.07446
\tag{2.3}
$$

$$
R_{TS}(SoC) = 0.3208e^{-29.14SoC} + 0.07446
\tag{2.4}
$$

$$
C_{TS}(SoC) = -752.9e^{-13.51SoC} + 703.6
\tag{2.5}
$$

$$
R_{TL}(SoC) = 6.603e^{-155.2SoC} + 0.04984
\tag{2.6}
$$

$$
C_{TL}(SoC) = -6056e^{-27.12SoC} + 4475
\tag{2.7}
$$

Applying Kirchhoff's voltage law in Figure 2.11, the battery's terminal voltage is given in (2.8).

$$
\begin{aligned}
V_{bat}(t) = &V_{OC}(t) - I_{Bat}R_s(t) + I_{Bat}\left(1 - e^{\frac{-t}{R_{TS}(t)C_{TS}(t)}}\right) \\
&+ I_{Bat}\left(1 - e^{\frac{-t}{R_{TL}(t)C_{TL}(t)}}\right)
\end{aligned}
\tag{2.8}
$$

It is necessary to scale these extracted parameters according to the Twizy battery pack configuration presented in Figure 2.9. Therefore the following factors: $ratio_V$, presented in (2.9), is applied in (2.2); $ratio_R$, presented in (2.10), is applied in (2.3), (2.4) and (2.6); $ratio_C$, presented in (2.11), is applied in (2.5) and (2.7);

$$ratio_V = n_{series} = 14 \qquad (2.9)$$

$$ratio_R = \frac{Cap_{CellTwizy}}{Cap_{CellTCL\ PL-383562}} \frac{n_{series}}{n_{parallel}} = 0.092 \qquad (2.10)$$

$$ratio_C = \frac{1}{ratio_R} = 10.84 \qquad (2.11)$$

Afterwards, it is possible to plot the terminal battery voltage $\left(V_{bat}\right)$ and open circuit voltage $\left(V_{OC}\right)$ with respect to the SoC, as presented in Figure 2.12.

Figure 2.12 – Estimated Twizy Battery voltages for 36 A charging.
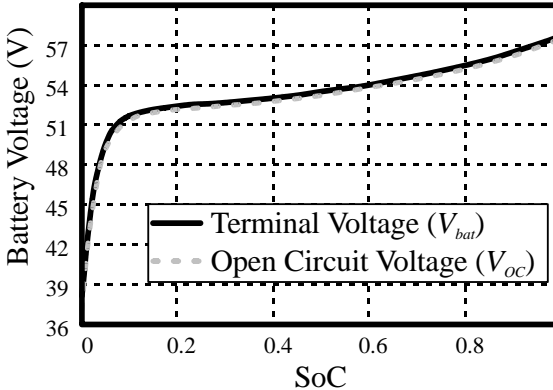
Source: Own elaboration.

2.4 Final considerations

In this Chapter, it was shown that EVs are not only currently playing an important role in the market, but also will overcome in quality and numbers the conventional cars. It was concluded that the success of

EVs highly interacts with lithium-ion battery technologies and charging converters. As the converter presented in this thesis is specified for a Renault Twizy, understanding its recharging process is crucial for product-oriented analysis. The results of the modelling were satisfactory as some results such as voltage range and recharging time were comparable with results found in practice.

3 WIRELESS POWER TRANSFER

In this Chapter, the WPT technology types and features are introduced. Comparisons between IPT and CPT types are presented. At first, it is also presented the main topics and trends on applications of WPT systems.

3.1 WPT applications

3.1.1 Electric Mobility

Besides stationary charging, theme of this thesis, Dynamic Wireless Power Transfer (DWPT) charging applied in vehicles while moving, including trains, planes and drones is achievable. The use of DWPT associated with electric buses as public transportation can fully enhance logistic and mobility, as in the case of KAIST's Online Electric Vehicle (OLEV) system in Korea [18], which 100 kW is transferred over a 20 cm of air-gap and 85% efficiency is achieved. Moreover, the relatively easy adoption of in-motion charging systems would result in a reduced battery bank and, hence, cheaper and lighter for the owner [19]. In Figure 3.1 (a), it is presented a DWPT charging implementation based on arrays of adjacent transmitter coils, therefore using IPT technology. In Figure 3.1 (b), it is presented the same concept for adjacent transmitter plates using a CPT system [20].

Figure 3.1 – Example of a DWPT EV charging: (a) IPT application, (b) CPT application.
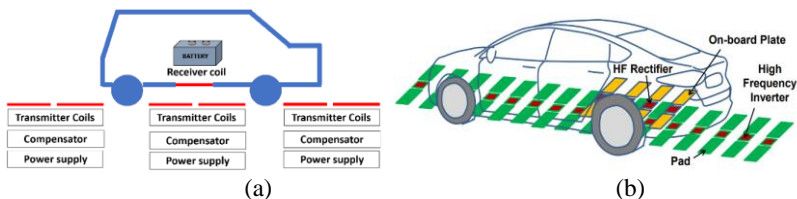
Source: [19], [20].

3.1.2 Electronic devices

Charging a mobile phone is a common scene nowadays. It brings not only convenience, but also safety. A table containing small wireless power networks is able to provide power to laptops and mobiles, as presented in Figure 3.2 (a). It is even possible to wireless charge not

having to place mobile phones on a surface, shown in Figure 3.2 (b), but simply holding or using them, as presented at Disney Research Laboratory and named as Quasistatic Cavity Resonance (QSCR).

Figure 3.2 – (a) A working table charging wirelessly (CPT) multiple devices, presented by Murata, (b) Multiple devices being charging (IPT) using QSCR.

(a)   (b)

Source: [Murata], [21].

3.1.3 Biomedical

Powering an implantable device wirelessly, as shown in Figure 3.4 (b), leads to less discomfort, less risk of infections, ease of communication and real time data acquisition. All of this can be implemented using the concept of Internet of Things, which can send alerts or diagnostics to the user or a doctor nearby. It can also provide electrical stimulation in sensory areas, as presented in Figure 3.4 (a). However, some safety issues must be addressed, as electromagnetic waves highly interact with human tissue and other body parts.

Figure 3.3 – Biomedical examples: (a) Electrical stimulation (IPT), (b) Charging (CPT) an implant device.

(a)   (b)
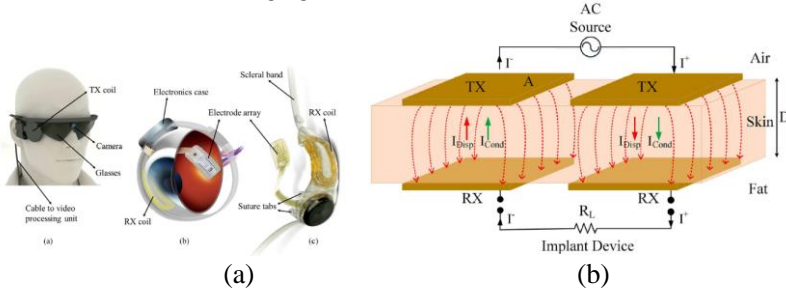
Source: [22].

3.1.4 Industry and Robotic

Wireless power transfer finds application in industry, such as the automotive manufacture industry. The world's first monorail system that utilized a non-contact power supply was created by Daifuku in 1993. The benefits include high reliability and durability, reduced maintenance and cost and increased safeness. In Figure 3.4 (a), it is presented autonomous programable mobile robots from WiBotic. These intelligent robots can be used in logistic application for highly flexible warehouses without the need of constantly monitoring and managing their batteries. In Figure 3.4 (b), it is presented a configuration of robot arms using WPT.

Figure 3.4 – Industry and Robotic examples: (a) Autonomous robots from WiBotic (IPT), (b) Robot arm configuration (IPT).

(a)   (b)

Source: [WiBotic, 2019], [23].

3.1.5 Military, Defense and Surveillance

Easily charging an equipment can enhance military and defense mission. It improves safety, capabilities and reduces battery weight. In Figure 3.5 (a) is presented an image from Solace using CPT systems to recharge defense equipment. In Figure 3.5 (b), it is presented a drone being charged in-flight, without the need of a landing pad to recharge.

Figure 3.5 – (a) Military application (CPT), (b) Surveillance application (IPT).

(a)   (b)

Source: [Solace], [GET].

3.2 WPT systems

Lines of research on WPT topic is dived into two large groups, acoustic field and **electromagnetic field**, as shown in Figure 3.6.

Figure 3.6 – Types of wireless power transfer.
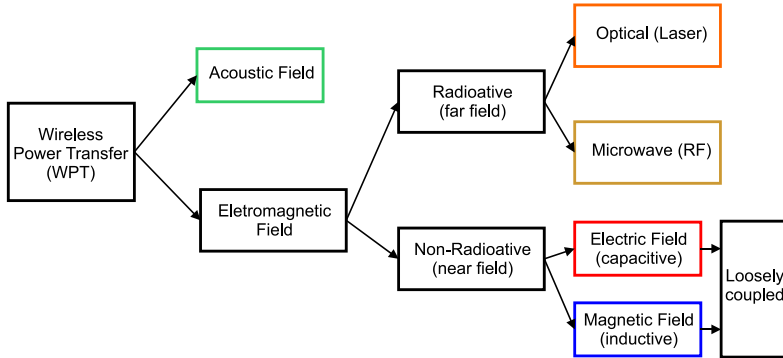
Source: Own elaboration.

3.2.1 Acoustic

For low power application, usually, an acoustic energy system consists of primary and secondary, both containing ultrasonic piezoelectric transducer and separated by a transmission medium, as shown in Figure 3.7.

Figure 3.7 – A typical acoustic energy system.
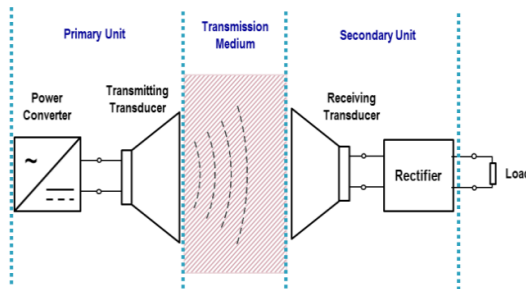
Source: [24].

The main important elements in this system are: power converter, rectifier, transmission medium and transducer. According to [24], the

multiple transceiver design offered 100% efficiency of energy transmission which is 7.24 mW output power.

3.2.2 Far field: laser and microwave

Figure 3.8 – Far field energy transfer example.
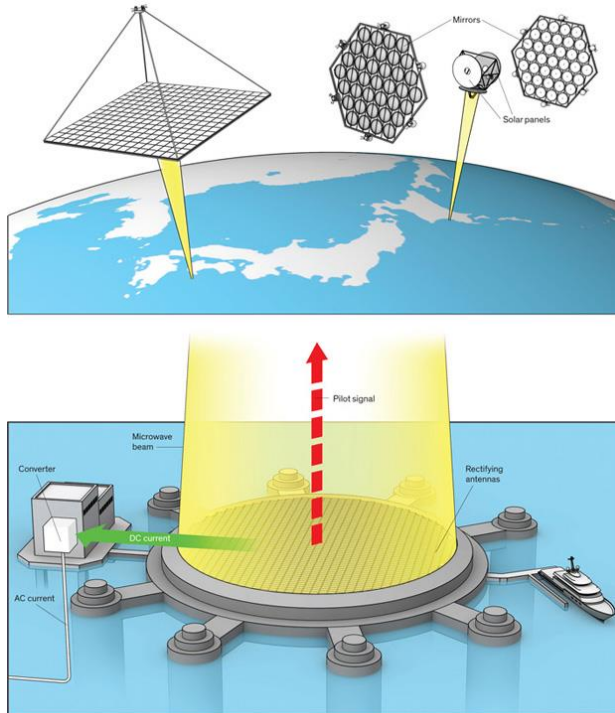
Source: [25].

In the far-field type, power is transferred from very distant places. This type can also be subdivided into two types: optical, which uses light wave length produced by lasers; and quasi-optical length wave microwave. A technology, called Solar Power Satellites (SPS) promises to deliver energy from solar power in satellites to Earth, Earth to space station, satellite to satellite and even Earth to Earth in very remote places. Asian countries, mostly Japan (Japan Aerospace Exploration Agency) is working on an ambitious project [25] to develop by 2030 a 1-gigawatt commercial system, as shown in Figure 3.8.

3.2.3 Inductive Power Transfer

Sometimes considered innovative and futuristic, the loosely coupled inductive power transfer is not a new concept. In fact, these experiments date back to the late 19th century and were first demonstrated by **Nikola Tesla**. In his biography, it is highlighted the tough victory in the war of the currents, more than 200 worldwide patents that includes the alternating induction motor, polyphase generation system and also the invention of the radio.

Moreover, Tesla had left a motivation in the popular imagination: a free transmission of electricity without the use of wires through the entire globe. Myth or truth, it is important to point out that from the concepts of the **Tesla Coil**, one of his most famous inventions, the first step on the WPT had begun. Figure 3.9 (a) presents one of Tesla's most famous picture and the **Wardenclyffe Laboratory** in which Tesla was envisioning the transmission of voice, pictures and power, presented in Figure 3.9 (b).

Figure 3.9 – (a) Nikola Tesla sitting besides its Tesla Coil and (b) The Wardenclyffe Laboratory and the World Wireless System (1901-1906).

(a) (b)
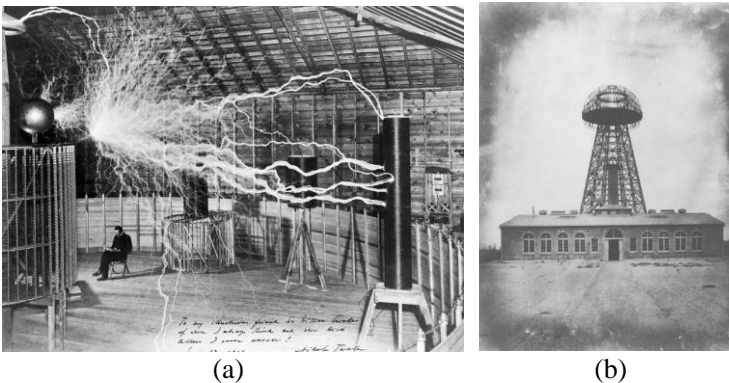
Source: [26].

With an altruistic and controversial view that energy could be transmitted on freely to any inhabitant of the Earth, his Wardenclyffe Laboratory's research was interrupted due to the discontent of financiers. Unfortunately, Tesla, a major contributor to the development of the 21st century, died with the reputation of a mad man due to his great sensitivity and perception about a better future for humanity, much ahead of his time.

Just over a half century later after Tesla's death, inductive WPT research was reappeared when Croatian Prof. **Marin Soljačić** brought a lot of attention after demonstrating in 2007 at the Massachusetts Institute of Technology (MIT) to be able to light a 60 W incandescent light bulb at two meters away with 40% efficiency. Afterwards, they founded the first company, **Witricity**, solely dedicated for WPT purposes. They claim a new system capable of operating at 3.7 kW to 11 kW about 91% to 94% overall efficiency [27].

Figure 3.10 – A stationary EV wireless charging using IPT from Witricity.

Source: [Witricity].

The IPT, since the time of Tesla the most versatile and famous, represent most of the researches and commercial systems available nowadays. In Figure 3.11, it is presented example of companies and consortiums for both CPT and IPT system. Research on IPT focus on three sub-areas: coil designs for better coupling and misalignment tolerance, compensation topology and power converter for processing efficiently high frequency waveforms.

Figure 3.11 – Some companies and consortiums: (a) CPT system, (b) IPT system.
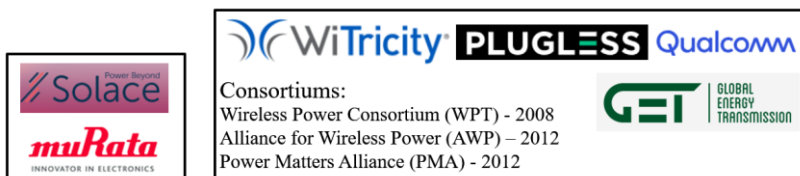
Source: Own elaboration.

3.2.4 Capacitive Wireless Power Transfer (CPT)

Although IPT is more common and popular, the first public presentation about WPT, held by Tesla in 1891 at Columbia College, New York, was actually through electrostatic induction, that is, **capacitive coupling** as shown in Figure 3.12.

Figure 3.12 – Nikola Tesla performing the first presentation about WPT using a CPT system at Columbia College, New York, in 1891.
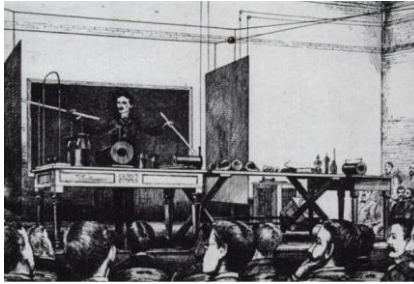
Source: [28].

A very interesting survey is presented in [28] about CPT and IPT, showing their progress and comparison over the last decade until 2015. When compared with IPT, the CPT is suitable for low power and short airgap (< 1 mm) applications, as shown in Figure 3.13

Figure 3.13 – IPT Vs CPT: Efficiency and delivered power versus airgap.
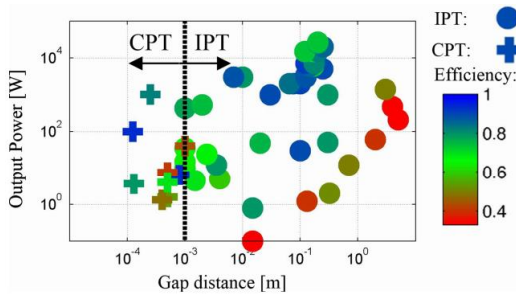
Source: [28].

Another great challenge of CPT system that needs to be addressed is the need for high frequencies (in the order of MHz) to transfer power of the order of kW, shown in Figure 3.14. This occurs because the capacitances formed in these medium airgap systems are very small, of

the order of picofarads [29], which requires either very high voltages or high frequencies to overcome the high impedance. In order to obtain similar results to the IPT systems regarding air-gap and power transfer capability, CPT systems require operating at very high frequencies above 10 MHz. These frequencies enables and prospect a drastic reduced size and weight, high efficiency and large air-gap [30], [31], [32].

Figure 3.14 – IPT Vs CPT: delivered power versus frequency.

Source: [28].
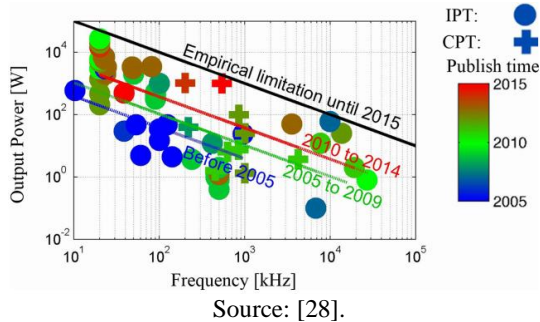
Considering no dielectric, the voltage across the metal plates are limited primarily by the air breakdown voltage; secondly, by the IEEE standard C95.1 [33], which indicates a human exposure of maximum voltage of 614V/m at 1 MHz. Frequency is limited by semiconductor components. The high power and high frequency conditions suggest the use of silicon carbide (SiC) or gallium nitrate (GaN) components.

Therefore, major focus of research on the part of the capacitive wireless transfer is in the application of low power and small air-gaps. Thus, a large topic still has to be covered with lines of research of capacitive transfer to charge EVs in order to achieve results similar to the inductive one, regarding power transfer capability and larger air-gaps.

3.2.4.1 CPT advantages and features

Some advantages stand out in a CPT system when compared to IPT system, regarding the following:

- **Metal interference** – the capacitive coupling has the advantage of not suffering interferences, both of power and signal in metallic proximity [34], as shown in Figure 3.15. This characteristic is responsible, for example, for

the implementation of brushless synchronous machines, which are replaced by a CPT system to feed the rotor [35], [36], power and date transfer with integrated circuits [37] and robotic applications [38] and [39];

Figure 3.15 – Metal interference: (a) in a CPT system; (b) in an IPT system.

(a)   (b)
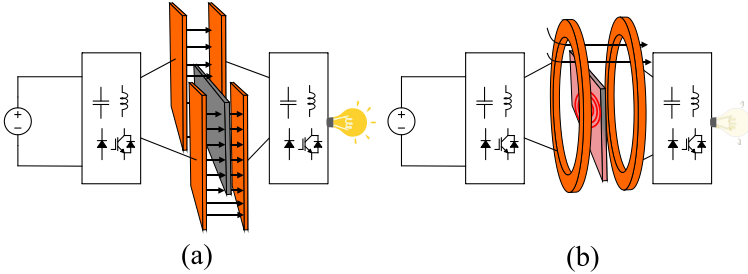
Source: Own elaboration.

- **Constructive aspect** – Another important advantage is the easy implementation with cost-effectiveness of the transmitter and receiver structures, since simple metal plates replace complex designs of planar coils made with Litz and Ferrite, as presented in Figure 3.16. According to [40], besides volume and weight reduction, a CPT can cost 40% less than an IPT charger.

Figure 3.16 – Constructive aspects of transmitters and receivers: (a) in a CPT system; (b) in an IPT system.

(a)   (b)
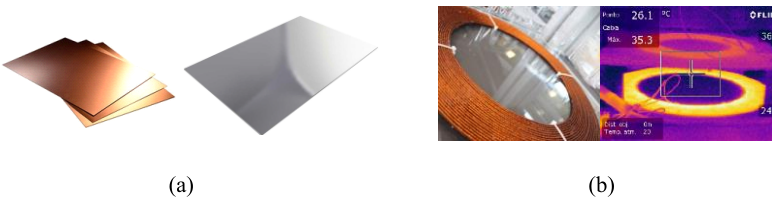
Source: Own elaboration.

- **EMI** – It should be emphasized the minimization of EMI due to the fact that the confinement of the electric field is established between the positive and negative poles of the metal plate pairs, unlike a magnetic field that form a loop from one pole to another pole, as shown in Figure 3.17;

- **Intrinsic properties** – the metal and medium found intrinsically on a given structure can be used to act as coupling capacitance and dielectric, such as, the use of stray capacitances between the vehicles' own chassis and ground [31], the use of wheels as dielectric medium [41].

Figure 3.17 – Electromagnetic lines: (a) in a CPT system; (b) in an IPT system.

(a)   (b)
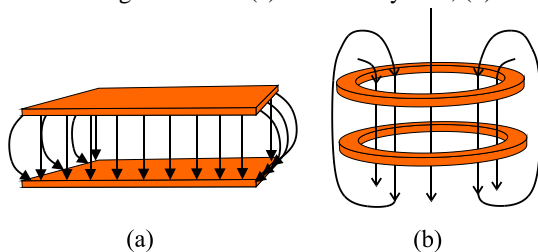
Source: Own elaboration.

Figure 3.18 – Metal and medium can intrinsically be used to charge a vehicle.
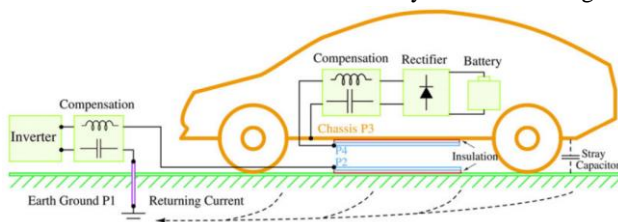
Source: [31].

3.3 Final considerations

In this Chapter, some practical, advanced and current application examples of WPT systems have been presented. Among WPT systems for EV charging, it is highlighted the IPT type due to its efficiency, power transfer capability, large air-gap and maturity in the market. However, when compared to an IPT, there are some specific features found only in a CPT system, such as power transfer through metal barrier. Besides, CPT systems can achieve similar results regarding efficiency, power and air-gap at the cost of very high frequencies (of the order of MHz). It is worth noting that, as the coupling capacitance is weaker, any stray capacitance, due to foreign object, or change in capacitance, due to climate conditions, can interfere in the equivalent capacitance of the system and, therefore, its performance can be compromised. Increasing voltage and frequency is desirable to improve efficiency and power density, however it must be

carefully sized as the high voltage stress across the plates is limited by breakdown voltage and human explosion voltage.

4 ELECTRIC FIELD THEORY OVERVIEW

The aim of this Chapter is to briefly introduce and review some fundamentals concepts necessary to understand a CPT system. The theory is presented from the very first principle to complex structures.

4.1 Basic electrostatic

Michael Faraday introduced in XIX the idea of **electric field lines**. These lines pull away from positive charges into negative charges. In Figure 4.1 (a), it is presented the electric field behavior produced by a negatively charged point. Considering an infinite sheet, which is closer approach to parallel plate capacitors, the electric field behavior is presented Figure 4.1 (b). In both cases, the electric field $\vec{E}$ equation are given in (4.1) and (4.2), respectively. Notice that, when considering an infinite conducting sheet charge, the electric field is constant and do not depend on the distance, but only on the charge density. The reader must be wondering why bothering to discuss such unrealistic situations as the fields produced by a pair of infinite charged plate. One reason is that it is very easy to analyze these situations using **Gaussian law**. A more important reason is that the analysis of "infinite" situations allows good approximations for real problems, such as dealing with points near a plate and fairly far from the edges. Therefore, the infinite case is analogous to the electric field nearby of a very large metal plate.

Figure 4.1 – Electric field: (a) A negatively charged point, (b) a positively charged infinite sheet.

(a)　　　　(b)
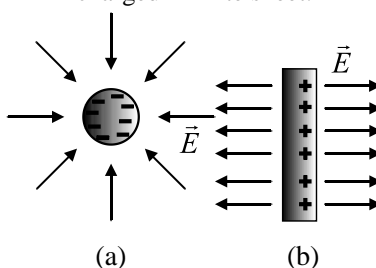
Source: Adapted from [42].

$$\vec{E} = \frac{1}{4\pi\varepsilon_o}\frac{q}{z^2} \tag{4.1}$$

$$\vec{E} = \frac{\sigma}{2\varepsilon_o} \tag{4.2}$$

Where:

- $\frac{1}{4\pi\varepsilon_o}$ is the Coulomb constant equivalent to 8.99 x 10^9 N.m²/C²;
- ε_o is the vacuum permittivity, also called electric constant, has the value 8.85 x 10^{-12}C²/N.m²;
- q is the electric charge given in Coulomb (C);
- z is the distance between a testing point and the charge (m);
- σ is the charge density (C/m²).

When two opposite equally charged points are placed closer, it is said to be a **dipole**. The interactions of the lines for punctual charges and a pair of infinite charged plate are presented in Figure 4.2 (a) and Figure 4.2 (b), respectively. For the case of a punctual electrical dipole, the electric field found in the vicinity is presented in (4.3). When $z \gg d$, the electric field is approximated as in (4.4). According to (4.1) and (4.4) it is possible to realize that the electric field produced by an isolate charge decreases with the proportion $1/z^2$, whereas a dipole is proportional to $1/z^3$. The quicker decrease in a dipole case is due to the opposite electric field cancelation. Notice that, lower values for p, either charge or separation, results also in lower electric field outside the objects. Basically, this is the principle of the electric field behavior of parallel plates charged oppositely with large area and very small separation. As already explained in Chapter 3, it explains a main advantage found in CPT system: the electric field tends to naturally be **contained** from a coupling plate to another plate. This is totally different from a magnetic field, which the lines of a magnetic field are always a loop.

For the case of a pair of infinite plates, the electric field is expressed by (4.5). Notice that electric field is kept constant regardless of the separation and the electric field is contained within the metal plates.

Figure 4.2 – Electric field line behavior: (a) dipole, (b) infinite metal plates.

(a)   (b)
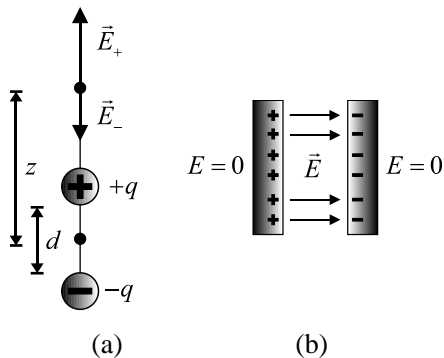
Source: Adapted from [42].

$$\vec{E} = \frac{q}{2\pi\varepsilon_o z^3} \frac{d}{\left(1 - \left(\frac{d}{2z}\right)^2\right)^2} \tag{4.3}$$

$$\vec{E} = \frac{1}{2\pi\varepsilon_o} \frac{p}{z^3} \tag{4.4}$$

$$\vec{E} = \frac{\sigma}{\varepsilon_o} \tag{4.5}$$

Where:
- p is the electric dipole (qd).

4.2 Electrostatic Induction and Power Transfer

One phenomenon that characterizes the transfer of wireless power by capacitive coupling is the **electrostatic induction**, that is, modification in the distribution of electric charge on an object caused by the presence of an electric field nearby. This phenomenon is most effective when the objects are conducting materials, such as metals, as electrons move freely.

An example of electric induction process is shown in Figure 4.3 (a), which depicts a positively charged conductor attracting the negative electrical charges of another conductor without the need of initial electrical contact. The process is concluded by temporally grounding the induced conductor. Such phenomenon occurs in any electrical circuit that contains a **capacitor** through a difference of potential applied to the conductive materials, as shown in Figure 4.3 (b), an electrical equivalent circuit representation. If another capacitor is placed in the return path, there is no need for actual electrical contact, as shown in Figure 4.4.

Figure 4.3 – Electrostatic induction process: (a) induction apparatus diagram, (b) equivalent circuit.

(a)   (b)
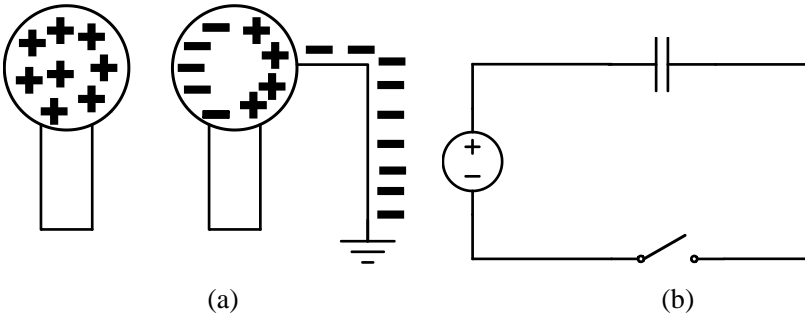
Source: Own elaboration.

Figure 4.4 – Equivalent circuit of a wireless electrostatic principle.
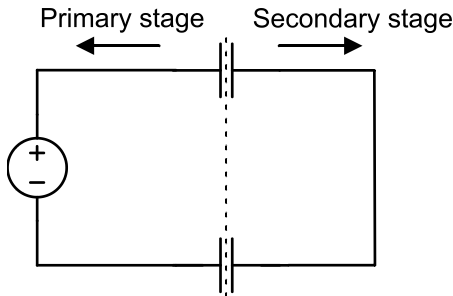
Source: Own elaboration.

It is possible to realize that a CPT system can only be achieved through the use of a pair of organized electric fields, from which one is "sent", and the other one is "returned". In an electrical equivalent circuit, this is translated as at least two capacitances: one is responsible for

"sending" current, and the other one is the return path of this current. This means that a CPT system is composed mostly of two pair of metal plates. It should be noted that these capacitances do not need to be formed necessarily by parallel metal plates, but any kind of capacitance, including stray capacitance that might be undesired in certain cases can actually be used.

Still, regarding CPT systems, the wireless electrostatic induction apparatus presented Figure 4.4 do not explain the **power transfer** concept, but only energy accumulation. Power in an electrical system is defined by the work over time needed to **move** the charge contained in an electric potential, as presented in (4.6). Now, considering only the electrical equivalent circuit representation, a resistance is placed to describe needed power, as presented in Figure 4.5. Notice that, delivered power, shown in (4.7), is realized only in the beginning of the turn ON process, or the turn OFF process. The faster this process is performed; more power is transferred. Straightaway, this is exactly a good definition of a **Wireless Power Transfer through coupling capacitances**, as opposed to definitions that presents the concept of a CPT system by means of AC voltage applied. This means that **commutation** is ultimately required.

Figure 4.5 – Principle of operation of a CPT system.
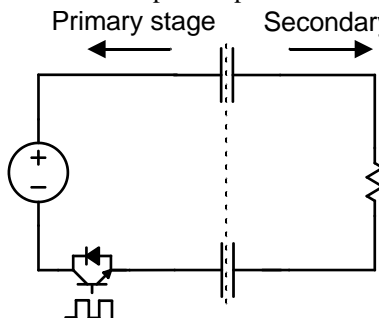
Source: Own elaboration.

$$P = \frac{\partial W}{\partial t} = \frac{\partial (qV)}{\partial t} \tag{4.6}$$

$$P = \left(\frac{\partial q}{\partial t}\right)^2 R = i^2 R \tag{4.7}$$

In order to process this energy in a suitable manner, e.g., charging a battery, more reactive and switching elements are wisely included, as presented in Figure 4.6.

Figure 4.6 – Complete operation of a CPT system.
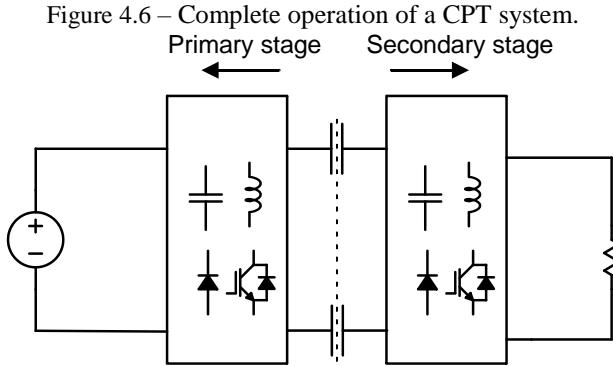
Source: Own elaboration.

4.3 Parallel-plate Capacitance: from simplified equation to Boundary Element Method (BEM).

The electrical charge that accumulates on the capacitor is proportional to the voltage applied as in (4.8), and depends on the **charge distribution, surface area**, **distance** between the plates and the **permittivity** of the material.

$$q = CV \qquad (4.8)$$

For which q is the electrical charge (C) deposited in absolute value on both plates, C is the **capacitance** (F) and V is the applied voltage (V). To relate the electric field between the plates to the total charge, Gauss's law is used in integral form, as presented in (4.9).

$$\oint_S \vec{E} \cdot \vec{da} = \frac{q}{\varepsilon_o \varepsilon_r} \qquad (4.9)$$

Considering that the charge is evenly distributed, parallel plate configuration, that the electric field is oriented symmetrically and disregarding the edge effect, as shown in Figure 4.7 and using (4.9), the capacitance can be expressed by (4.10).

Figure 4.7 – Distribution of the electric charge between two parallel plates.
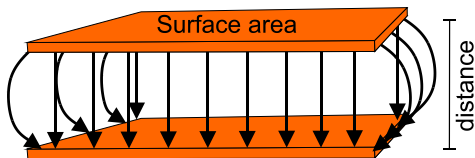
Source: Own elaboration.

$$C_o = \frac{\varepsilon_o \varepsilon_r A}{d} \qquad (4.10)$$

For which ε_o, is the electrical permittivity in vacuum and has a value of 8,85 $pC^2/N.m^2$, ε_r the relative permittivity of the medium (the air is approximately unitary), A the surface area (m^2) and d the separation between the plates (m).

Equation (4.10) is valid when the distance d is much smaller than the area. When the gap between the plates is large enough, it is not accurate as the charge distribution is no longer uniform and the edge effect is not negligible.

To find values closer to the real ones, the authors in [43] use the Boundary Element Method (**BEM**) for parallel plate capacitors of some geometric formats. It was considered equation (4.10) as nominal value to normalize the capacitance calculated using BEM. In the same way, the charge density was normalized with respect to the simplified value.

From this study, it is possible to conclude that:

- For a given length, as the distance between the plates increases, the charge density on the plates increases with respect to the simplified nominal value, this increment being even greater at the edges;
- Therefore, the capacitance is increased in relation to the nominal value. That is, as the distance increases, equation (4.10) results in capacitance values that are increasingly lower than in practice;
- Among the circular, square and rectangular formats, given the same area and space, the capacitance of the rectangular shaped plates is the largest, followed by the square, which is slightly superior to circular. This occurs because the ratio of the perimeter to the area of the rectangular shape is the largest, followed by the square and then circular.

- Also, for the same area, considering a scenario with rectangular plates with a width of 1/3 m and length of 3 m, and another scenario with square plates with width of 1 m and length of 1 m, both with an area of 1 m² and separated by 0.2 m. The rectangular form plates have a capacitance approximately 23% larger than the square plates.

Through the BEM method and empirical approximation, the authors in [43] proposed the expression of the capacitance of parallel plates in the format of square (4.11) and circular (4.12). In this thesis, their found equations were adapted to become a function of area, instead of width or radius.

$$C_s = C_o\left(1 + 2,343\left(\frac{d}{\sqrt{A}}\right)^{0.891}\right), \text{ if } (0,1 \le \frac{d}{\sqrt{A}} < 1,0)$$

$$C_s = C_o\left(1 + 2,343\left(\frac{d}{\sqrt{A}}\right)^{0.992}\right), \text{ if } (1,0 \le \frac{d}{\sqrt{A}} < 10)$$

(4.11)

$$C_D = C_o\left(1 + 2,367\left(\frac{d\sqrt{\pi}}{2\sqrt{A}}\right)^{0.867}\right), \text{ if } (0.005 \le \frac{d\sqrt{\pi}}{2\sqrt{A}} < 0.5)$$

$$C_D = C_o\left(1 + 2,564\left(\frac{d\sqrt{\pi}}{2\sqrt{A}}\right)^{0.982}\right), \text{ if } (0.5 \le \frac{d\sqrt{\pi}}{2\sqrt{A}} < 5.0)$$

(4.12)

4.4 Constructive aspects of a capacitor

When designing a capacitor with very small air-gap, one must pay attention to the fact that the material might not be entirely filled with dielectric (which is usual considering they're moving parts). The capacitance is defined as a function of the dielectric material and the distance containing air, as presented in Figure 4.8.

Considering that charge is evenly distributed through the object, it follows from (4.13) to (4.18), that the equivalent capacitance of such structure is nothing more than the series equivalent capacitance of each substructure, as presented in (4.19). Therefore, a small capacitance in a series capacitance lumped circuit will drastically degrade the equivalent

capacitance to a maximum permittable equivalent capacitance equal to the least capacitance value.

$$Q_{total} = C_{total}V_{total} = C_{total}\left(V_{d1} + V_{d2} + V_{air}\right) \tag{4.13}$$

$$Q_{total} = Q_{d1} = Q_{d2} = Q_{air} \tag{4.14}$$

$$C_{d1}V_{d1} = C_{d2}V_{d2} = C_{air}V_{air} \tag{4.15}$$

$$V_{d1} = \frac{Q_{total}}{C_{d1}}$$
$$V_{d2} = \frac{Q_{total}}{C_{d2}} \tag{4.16}$$
$$V_{air} = \frac{Q_{total}}{C_{air}}$$

$$Q_{total} = C_{total}\left(\frac{Q_{total}}{C_{d1}} + \frac{Q_{total}}{C_{d2}} + \frac{Q_{total}}{C_{air}}\right) \tag{4.17}$$

$$\frac{1}{C_{total}} = \frac{1}{C_{d1}} + \frac{1}{C_{d2}} + \frac{1}{C_{air}} \tag{4.18}$$

$$C_{total} = \frac{\varepsilon_o A}{\frac{d_1 + d_2}{\varepsilon_r} + d_{air}} \tag{4.19}$$

Figure 4.8 – Dielectric material affecting equivalent capacitance.
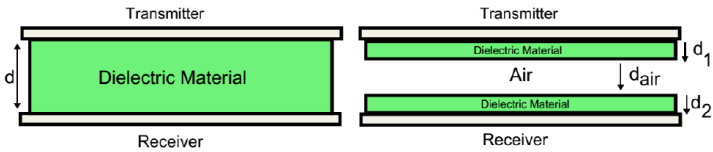
Source: [40].

Interestingly, these equations also explain why CPT systems are not affected by metal barriers. For example, if a metallic plate is placed

between a pair of plates, the equivalent capacitance is kept the same, as it is now formed by two capacitors with doubled values connected in series, which equivalent capacitance results the same before placing the metallic plate.

Another parameter that must be considered is how planar or deformed is a given structure, as shown in Figure 4.9. Again, for very small distances, the capacitance value becomes very sensible to these parameters.

Figure 4.9 – Capacitance of deformed structure.
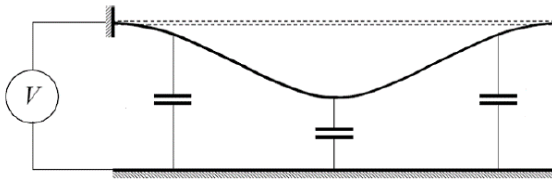
Source: [40].

In fact, for very small gaps, distance becomes challenging to measure or to verify, and the equivalent capacitance is better defined in terms of applied pressure, rather than the distance itself. In [44], a study of the applied pressure on a conformal bumper capacitor presented the results shown in Figure 4.10

Figure 4.10 – Capacitance of couplers versus normalized conformal force. Base force 100 N.
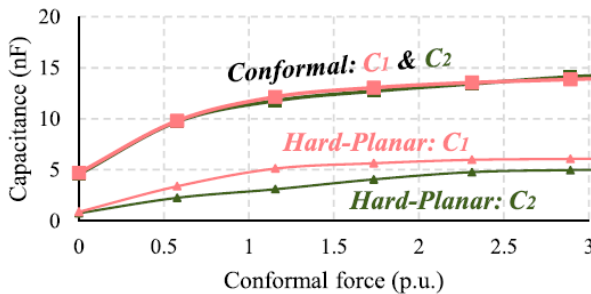
Source: [44].

4.5 Dielectric properties

The increasing frequency also affects the dielectric properties of a material. Although dielectric with high dielectric constant improves the coupling capacitance, factors as loss tangent, dielectric strength and dielectric constant vary significantly with the frequency. A parameter defined as in (4.20) represents the dissipative property of a dielectric material.

$$\tan\delta = \frac{R_{ESR}}{X_C} = R_{ESR}\, 2\pi f_s C \tag{4.20}$$

Where:
- R_{ESR} is the equivalent series resistance at given frequency;
- X_C is the reactive capacitive impedance

The term $\tan\delta$ is practically constant, and therefore, for higher frequencies, R_{ESR} decreases, contributing to elevating efficiency at higher frequency. This is another advantage of a CPT system over an IPT system, where, clearly, the loss of a coil is directly proportional to the frequency. However, it is important to note that the leads or wire connection between plates and circuit will have an impact on the equivalent circuit, as presented in (4.21). This dynamic can be observed in an Impedance Analyzer. Therefore, properly connecting with short adequate wires that eliminates the skin and proximity effects, such as Litz wire or coaxial cables, and constructing magnetic elements likewise is essential for good performance.

$$Z_{cap} = R_{parasitic} + R_{ESR} + \frac{1}{j\omega C} + j\omega L_{parasitic} \tag{4.21}$$

The dielectric strength or voltage breakdown is a parameter that limits the separation of a capacitor. Considering a pure sinusoidal voltage, the maximum strength constant permittable [40] as a function of the area, frequency, current and permittivity is given in (4.22). Such equation explains why in a standard capacitor for higher frequencies, more current is allowed while less voltage across the capacitor is allowed. Conversely, for lower frequencies, less current is allowed while more voltage is allowed. The same principle is applied for any type of capacitor.

$$E_{str} > 2\pi f I \varepsilon_r \varepsilon_o A \tag{4.22}$$

In Table V, it is shown the dielectric property of some material found in [45]. It is also included the results for fiberglass material at 300 kHz, found experimentally in this thesis using Impedance Analyzer.

Table V – Dielectric properties of some materials.

Material	Dielectric Constant	Strength Constant kV/mm
Air	1.005364	3
Soil	10 – 20	–
Teflon	2.1	60
Porcelain	6 – 8	4 – 12
Mica	5.4	160
Polyester	3.6	21.7
Silicon Carbide	10.2	–
Glass	4 – 7	13
Water	73.2 – 99	–
Paper	3.3 – 3.5	14 – 16
Transformer oil	4.5	12
Human skin	33 – 44	–
Fiberglass*	4.8	50

Some capacitance properties are even more challenging to describe, since they are a function of the applied voltage, as in the case of MOSFETs and IGBTs.

4.6 Coupling Interface

Depending on the disposition of the coupling structure, the electric field is naturally rearranged. Therefore, a high interaction between plates AB, Ab, ab and Ba, shown in Figure 4.11, can result in a different equivalent capacitance that requires understanding. Thus, the more the distance between main capacitances increases, the more the impact and interaction are expected, becoming necessary that all capacitive couplings

to be considered in order to obtain an accurate model. This way, the 4 plates form a set of 6 coupled capacitances.

Figure 4.11– Coupling, and cross-coupling and self-capacitances.
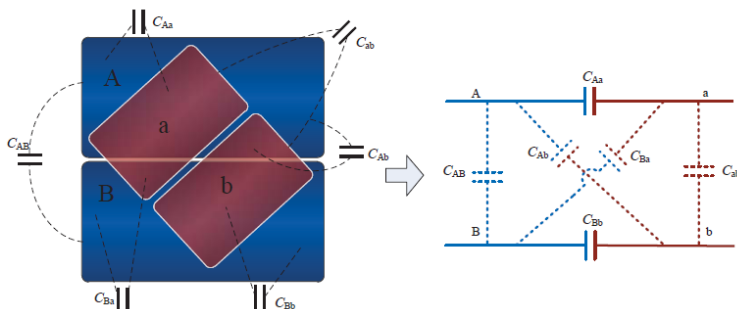
Source: [46].

In Figure 4.11, C_{Aa} and C_{Bb} are defined as main coupling capacitance, C_{Ab} and C_{Ba} are called cross-coupling capacitance and C_{AB} and C_{ab} are defined as leakage capacitance or self-capacitances.

Note that this structure is very complex and, despite the duality in the transfer through the electric field in relation to the magnetic field, does not present a duality in relation to the equivalent model of an IPT system. Therefore, some concepts such as mutual capacitance C_M, dual the mutual inductance, and coefficient of electric coupling K_E, dual to the coefficient of magnetic coupling were abstracted in [47].

Through mathematical manipulation and circuit theory, the authors were able to propose a model equivalent to the physical model and, at the same time, dual to the IPT equivalent model. Figure 4.12 presents this equivalent model called Behavior Source Model.

Figure 4.12 – Behavior Source Model equivalent circuit.
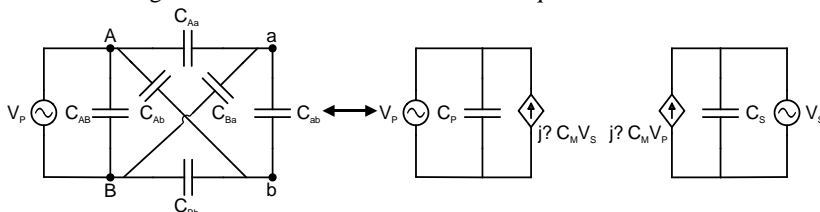
Source: Own elaboration.

The system is modeled by a mutual capacitance (C_M), self-capacitances (C_P and C_S) and a voltage-controlled current source

representing the transfer of energy, as shown in Figure 4.12. The values of C_P, C_S and C_M are expressed, theoretically, as a function of the 6 capacitances or can be measured experimentally [47].

To find the values of C_P, C_S and C_M, this chapter presents a method using Thevenin theorem. The initial step is based in [48], by short circuiting V_S to find C_P, as presented in (4.23) and shown in Figure 4.13.

Figure 4.13 – Finding C_P by short-circuiting the terminals ab.
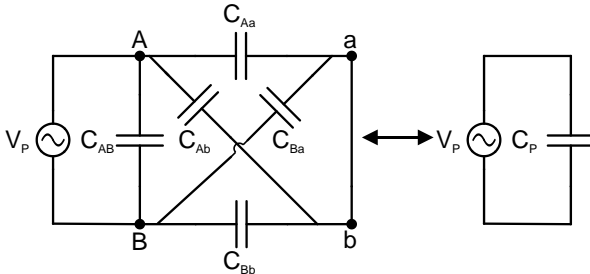
Source: Own elaboration.

$$C_P = C_{AB} + \frac{(C_{Aa} + C_{Ab})(C_{Ba} + C_{Bb})}{C_{Aa} + C_{Ab} + C_{Ba} + C_{Bb}} \qquad (4.23)$$

In the same way, a testing voltage source is applied across the terminal ab, while the terminals AB is short circuited. Therefore C_S is expressed by (4.24).

Figure 4.14 – Finding C_S by short-circuiting the terminals AB and supplying voltage across the terminals ab.
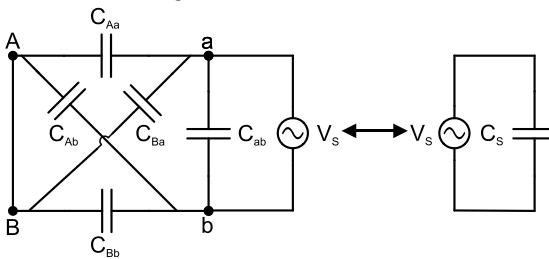
Source: Own elaboration.

$$C_S = C_{ab} + \frac{(C_{Ba} + C_{Aa})(C_{Ab} + C_{Bb})}{C_{Aa} + C_{Ab} + C_{Ba} + C_{Bb}} \qquad (4.24)$$

Afterwards, the secondary is open-circuited, as presented in Figure 4.15 to obtain C_M, shown in (4.25) and (4.26).

Figure 4.15 – Finding C_M by describing the voltage across the open-circuit terminal ab.
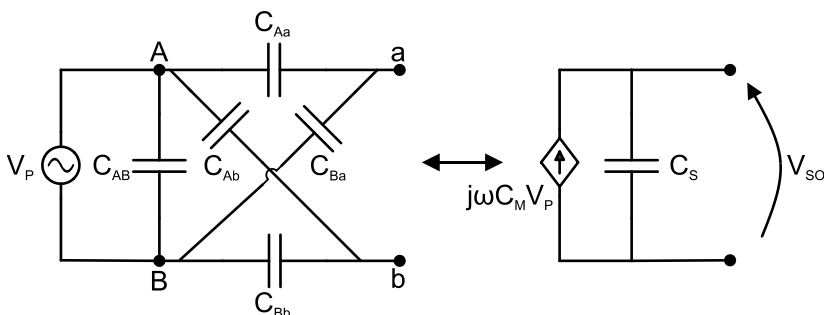
Source: Own elaboration.

$$V_{S_O} = j\omega C_M \frac{1}{j\omega C_S} = \frac{C_M}{C_S} V_P \qquad (4.25)$$

$$C_M = \frac{V_{S_O}}{V_P} C_S = \frac{V_{ab}}{V_{AB}} C_S \qquad (4.26)$$

Therefore, it is necessary to obtain the expression of V_{S_O}, that is V_{ab}. To do so, it is used Thevenin theorem across the terminals ab. Notice that parallel capacitor C_{AB} does not change the Thevenin voltage as it is in parallel with a voltage source. The Thevenin voltage and Thevenin capacitance circuits are presented in Figure 4.17 and Figure 4.16, respectively. The resulting equations are shown in (4.27) and (4.28). The mathematical process to find the Thevenin equivalent equations are laborious, and therefore will be abstained.

Notice that the Thevenin circuit is itself an equivalent circuit that can be used to analyze a CPT system. However, this equivalent circuit can only be applied in linear systems.

$$V_{th} = V_p \frac{C_{Aa}C_{Bb} - C_{Ab}C_{Ba}}{\left(C_{Aa} + C_{Ba}\right)\left(C_{Ab} + C_{Bb}\right)} \qquad (4.27)$$

$$C_{th} = \frac{\left(C_{Aa} + C_{Ba}\right)\left(C_{Ab} + C_{Bb}\right)}{C_{Aa} + C_{Ab} + C_{Ba} + C_{Bb}} \qquad (4.28)$$

Figure 4.16 – Thevenin equivalent capacitance C_{th} across terminal ab.
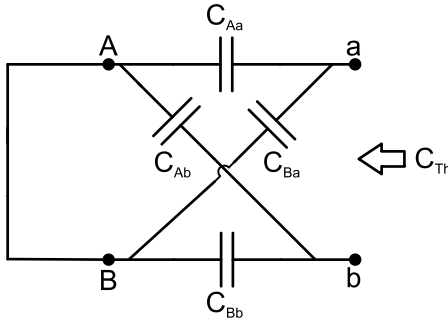
Source: Own elaboration.

Once V_{th} and C_{th} are calculated, it is possible to describe V_{S_o}, as function of them as shown in. A voltage divider, shown in (4.29) results in (4.30).

Figure 4.17 – Thevenin equivalent circuit model.
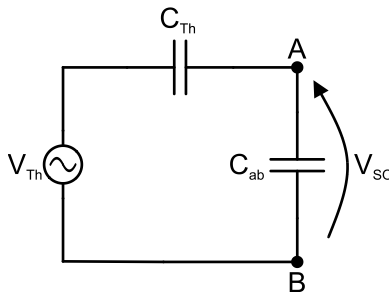
Source: Own elaboration.

$$V_{S_o} = \frac{V_{th}C_{th}}{C_{th} + C_{ab}} \qquad (4.29)$$

$$V_{S_O} = V_P \frac{C_{Aa}C_{Bb} - C_{Ab}C_{Ba}}{C_{ab}\left(C_{Aa} + C_{Ba} + C_{Ab} + C_{Bb}\right) + \left(C_{Aa} + C_{Ba}\right)\left(C_{Ab} + C_{Bb}\right)} \quad (4.30)$$

Substituting (4.30) and (4.24) in (4.26), finally results in the expression that describes C_M in terms of main and cross-coupling capacitances. Notice that, it does not depend on leakage capacitances.

$$C_M = \frac{C_{Aa}C_{Bb} - C_{Ab}C_{Ba}}{C_{Aa} + C_{Ba} + C_{Ab} + C_{Bb}} \quad (4.31)$$

Similar to magnetic coupling coefficient, it is defined the capacitive coupling coefficient as presented in (4.32) and (4.33).

$$k_E = \frac{C_M}{\sqrt{C_P C_S}} \quad (4.32)$$

$$k_E = \frac{C_{Aa}C_{Bb} - C_{Ab}C_{Ba}}{\sqrt{\left(C_{Aa} + C_{Ab}\right)\left(C_{Aa} + C_{Ba}\right)\left(C_{Ab} + C_{Bb}\right)\left(C_{Ba} + C_{Bb}\right)}} \quad (4.33)$$

A straightforward analysis can be done by considering symmetry in the coupling interfaces: $C_{Aa} = C_{Bb} = C$ and $C_{Ab} = C_{Ba} = C_{cross}$. This way, the coupling coefficient is simply defined as in (4.34)

$$k_E = \frac{C - C_{cross}}{C + C_{cross}} \quad (4.34)$$

Simple and interesting conclusions are presented:
- If $C_{cross} = 0$ (no cross-coupling capacitance), $k_E = 1$, meaning maximum energy transfer;
- If $C_{cross} = C$, $k_E = 0$, meaning power is nulled;
- If $C_{cross} > C$, $k_E < 0$, meaning that cross-coupling capacitance transfer power;
- If $C = 0$ (no main capacitance), $k_E = -1$, meaning maximum energy transfer, but through cross-coupling capacitances;

- For any general case presented in (4.33), $-1 < k_E < 1$ [48].

When using Behavior Source Model equivalent circuit, measuring each coupling capacitance is not necessary. A practical measurement test, as in open-circuit and short-circuit of a transformer, can be performed:

- To measure C_P, short-circuit secondary stage and measure the capacitance across terminal AB;
- To measure C_S, short-circuit primary stage and measure the capacitance across terminal ab;
- To measure C_M, apply a sinusoidal voltage at operating frequency across primary stage and measure the open-circuit voltage across terminal ab and apply (4.26).

4.7 Experimental results

Figure 4.18 – Double-sided copper printed circuit board used in the experiments: (a) Primary side view, (b) secondary side view.

(a)

(b)
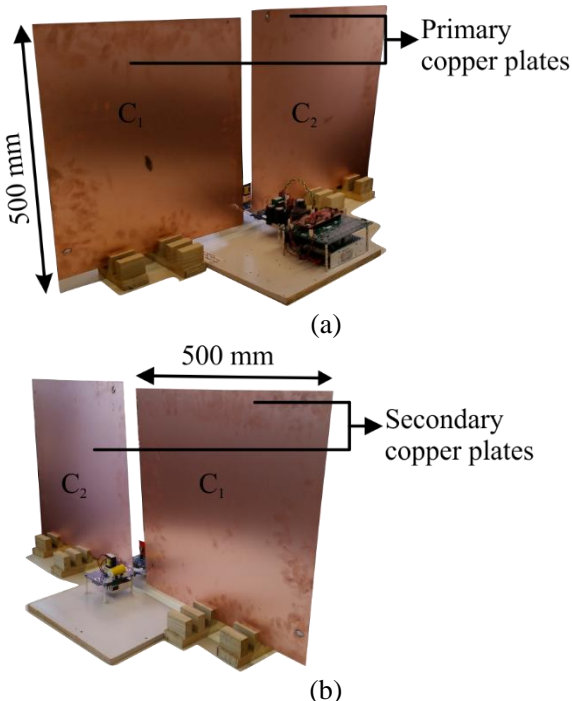
Source: Own elaboration.

In this thesis, for simplicity, the capacitors are made of a double-sided copper printed circuit board (500 mm x 500 mm) with 1.5 mm fiberglass acting as dielectric, as presented in Figure 4.18. The capacitance of the two double-sided plate was measured using E4990A Impedance Analyzer, which results are shown in Figure 4.19 and Figure 4.20, respectively.

The capacitances measured at 300 kHz were 7.1 nF for both metal plate pairs. Notice that a resonance frequency is found at approximately 3 MHz. Therefore, the fiber glass dielectric constant at 300 kHz can be determined by simply rearranging (4.10), as presented in (4.35), which resulted in approximately 4.8.

Figure 4.19 – Impedance characteristic of double-sided plate "C_1".
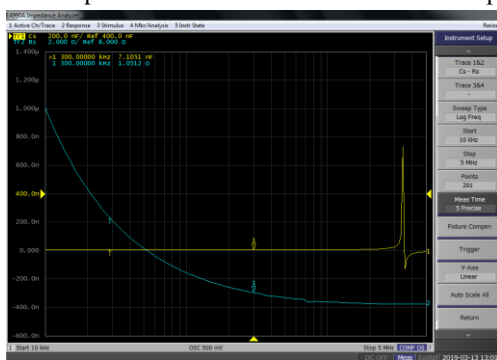
Source: Own elaboration.

Figure 4.20 – Impedance characteristic of double-sided plate "C_2".
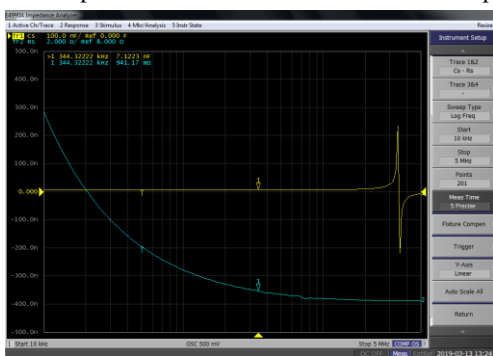
Source: Own elaboration.

$$\varepsilon_{r_{f.glass}} = C_{measured} \frac{d}{\varepsilon_o A} = 4.8 \qquad (4.35)$$

4.8 Final considerations

A complete definition of a CPT system and main features were presented from the most initial basic structure (a punctual electric charge) to more complex ones (4 planar plate configuration) in a simple way.

Regarding designing parallel-plate capacitors, it is concluded that for very small gaps (<mm), which distance and format are challenging to measure or control, applied pressure suits better for describing the capacitance. As the distance between parallel plates increases, the edge effect becomes more significant and more charge is capable to be deposited on the plates. It is concluded that the equivalent capacitance in a given structure is a function of the distribution charge, dielectric properties, frequency and cross-interaction between surfaces. Their interaction can even null power transfer.

The study of parallel plates as capacitors presented in this chapter can be used in any printed circuit, not only for wireless power transfer purposes. It is suggested the investigation of the effectiveness to conclude if a relatively needed low capacitor composed of inner layers in a printed circuit board (PCB) can improve volume, lifetime and efficiency of a circuit.

5 CONVERTERS APPLIED IN CPT

In this Chapter, the commonly converters applied in a CPT system are briefly introduced, presenting their advantages, disadvantages and main features.

5.1 Resonant full bridge inverters

These topologies are mostly common in WPT systems and, combined with a resonant circuit, are able to provide excitation to the primary side effectively. As for the resonant circuits, a large number is already present in the literature, such as L, LC [49], LCL, LCLC [50], CLLC and others. The simplest of all, L series inductor series connection in both primary and secondary is shown in Figure 5.1.

Figure 5.1 – Resonant series converter applied in CPT.
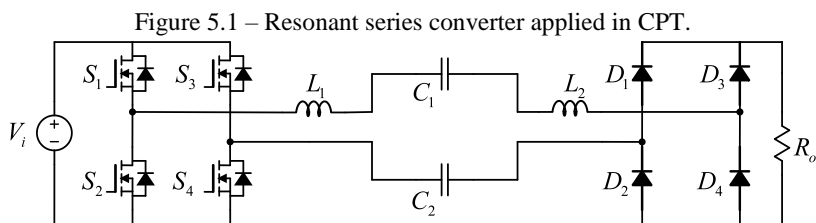
Source: Adapted from [51].

Each compensation topology has different characteristics with advantages and disadvantages. For example, despite the simplicity of the L-series topology, it has the drawback of requiring high inductances in order to establish resonance with the low coupling capacitors.

One solution would be the use of external capacitors in parallel, thus, forming the LC topology, as shown in Figure 5.2 [49]. The addition of parallel capacitors would result in a combination of reduced inductances for resonance establishment. However, considering the addition of external capacitances much larger than the coupling capacitance, the resonance condition becomes dependent mostly on external capacitors, and therefore causes this converter to behave similar to a SS topology [52] in an IPT system: independent resonance establishment and highly unstable regarding misalignment.

Figure 5.2 – Double side LC Resonant converter applied in CPT.
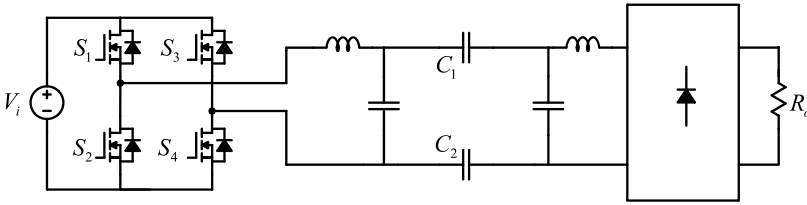
Source: Adapted from [49].

To make the system directly proportional to the capacitive coupling coefficient, the LCLC compensation on both sides is proposed in [50], as shown in Figure 5.3.

Figure 5.3 – Double-sided LCLC Resonant converter applied in CPT.
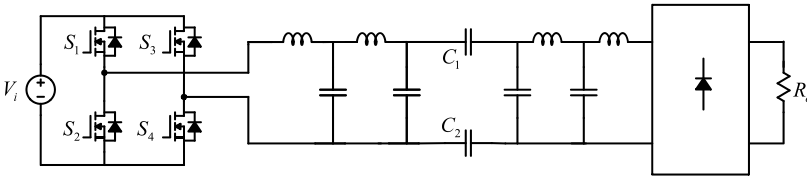
Source: Adapted from [50].

5.2 Power amplifier converters

Systems based on high frequency amplifiers, such as class D, class E and others [53], [54], [44] can be modified to implement CPT. In fact, they can also be classified as resonant converters.

Intrinsically, amplifiers operate at very high frequencies, resulting in the reduction of storage elements, increased efficiency, and large transfer distance. In contrast, these topologies are highly sensitive to parameter variation. In practice, variations such as capacitance between the plates are inevitable and can affect resonance, which causes drastic reduction of transmitted power.

In [54], a very low power Class-E (0.97 W) with 96% efficiency is presented. In [44], this topology is used for charging electric vehicles with a conformal bumper installed in front of a vehicle, as shown in Figure 5.4 The results showed efficiency of 92% for 1 kW at 530 kHz.

Figure 5.4 – Class E amplifier applied in CPT.
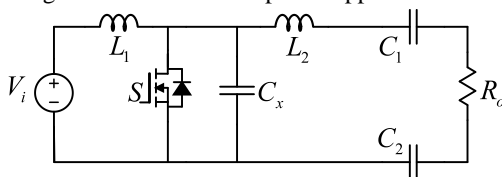
Source: Adapted from [44].

5.3 PWM Converters

5.3.1 Modified SEPIC, ZETA and ĆUK converters

All the classical converters with a link capacitor can be modified to be applied in CPT [34]. The advantages of the PWM converters include the use of few switch elements and simplified signal conditioning. Due to its asymmetry, applications are limited by the voltage allowed in the switching elements and, therefore, reaching lower power levels when compared to topologies based on the full bridge converters. The classical PWM converters that have a series capacitor: Ćuk, SEPIC and Zeta can then be used for WPT purposes by adding a capacitor to the current return path as shown in Figure 5.5, Figure 5.6 and Figure 5.7, respectively.

Figure 5.5 – Ćuk converter: (a) Conventional, (b) Modified.

(a)   (b)
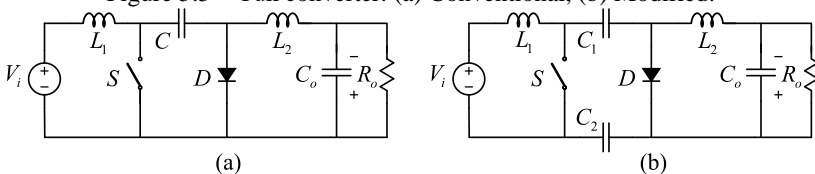
Source: Adapted from [34].

Figure 5.6 – SEPIC converter: (a) Conventional, (b) Modified.

(a)   (b)
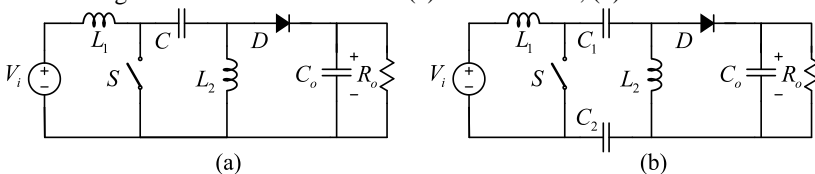
Source: Adapted from [34].

Figure 5.7 – Zeta converter: a) Conventional, b) Modified.

(a) (b)
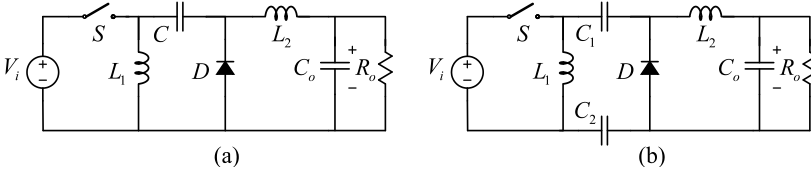
Source: Adapted from [34].

It is verified that the equivalent circuit of the modified converters is the standard circuit of each converter, considering an equivalent series capacitance (5.1) between C_1 and C_2. The voltage across each coupling capacitor are presented in (5.2) and (5.3), while current flow keeps the same across both capacitors.

$$C = \frac{C_1 C_2}{C_1 + C_2} \tag{5.1}$$

$$v_{C_1} = \frac{C_2}{C_1 + C_2} v_C \tag{5.2}$$

$$v_{C_2} = \frac{C_1}{C_1 + C_2} v_C \tag{5.3}$$

If $C_1 = C_2$, then the voltage across the coupling capacitors are simply defined by (5.4).

$$v_{C_1} = v_{C_2} = \frac{1}{2} v_C \tag{5.4}$$

Thus, under certain conditions, most of the characteristics ruling the modified converters are the same as those classical converters:

- Simple conditioning and driving circuitry;
- Operates as step up or step down with a static gain similar in continuous conduction mode (CCM) to (5.5);
- Capacitive accumulation (indirect converter);
- They are fourth order systems that hinder the control of the structure [55].

$$G(D) = \frac{D}{1-D} \qquad (5.5)$$

5.3.1.1 Mean voltage value across the coupling capacitor

      The mean voltage value across the coupling capacitor of these 3 converters is non-zero, an apparent disadvantage for capacitive coupling wireless energy transfer applications [34]. This average value affects the performance of the coupling capacitors, since the voltage applied to the plates is limited by the rupture stress of the medium in which they are located. In addition, the efficiency seems to be affected by this average component.

      Knowing that in steady state the stability of the converter is guaranteed by the null average voltage value across the inductors, considering classical static gain and observing the mesh containing the inductors in Figure 5.5, Figure 5.6 and Figure 5.7, the average voltage value of the coupling capacitors are:

$$\frac{\left\langle V_{C_{\acute{C}uk}} \right\rangle_{T_s}}{V_i} = \frac{1}{1-D} \qquad (5.6)$$

$$\frac{\left\langle V_{C_{SEPIC}} \right\rangle_{T_s}}{V_i} = 1 \qquad (5.7)$$

$$\frac{\left\langle V_{C_{Zeta}} \right\rangle_{T_s}}{V_i} = \frac{D}{1-D} \qquad (5.8)$$

      To find the mean voltage value across each coupling capacitor C_1 and C_2, apply the expressions (5.6), (5.7) and (5.8) in (5.2) and (5.3)

5.3.2 Modified Buck-Boost

      To solve the problem of non-null average voltage value across coupling capacitances inherent to the converters shown in section 5.3.1.1 5.3.1.1, [34] proposes a topology based on the buck-boost converter, as shown in Figure 5.8.

Figure 5.8 – Modified Buck-Boost converter: a) Equivalent, b) Complete.

(a) (b)
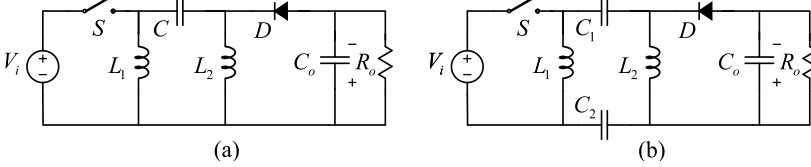
Source: Adapted from [34].

5.3.2.1 Mean value of the voltage at the coupling capacitor

It can be seen, therefore, that for any mode of operation, the average voltage values across the capacitors are zero.

$$\frac{\langle V_C \rangle_{T_s}}{V_i} = 0 \qquad (5.9)$$

5.4 Final considerations

Any power converter that contains a series capacitor on its structure can be modified to be applied in CPT systems. It is important to note that, besides adding a capacitor on the return path, the converter must maintain or improve its characteristic for low capacitance values.

As expected, among the presented types, the Full H-Bridge Resonant converters present the best results regarding power density, efficiency, air-gap and misalignment. However, they require more complex structures and a large number of reactive elements and, therefore, might be unfeasible for relatively low power applications.

Following efficiency results, there are the Power Amplifier converters, which hold their advantage on the simplicity. On the other hand, they are highly dependent on the frequency resonance, and, therefore cannot allow practical misalignments. Power is also limited by the single active switch.

The PWM converters are commonly suitable for low power application and present simpler structures. Different from the Power Amplifier converters, they are able to maintain their static gain constant for relatively small variations on the coupling capacitances. Regarding the PWM converters, the average voltage value across the coupling

capacitances are harmful, but can be overcome with the use of a modified Buck-Boost.

As it is presented in the following Chapter 6, in the same way that a conventional Buck-boost can be modified to its isolated version, Flyback, the modified Buck-boost can also be modified to its isolated version. However, as the coupling capacitors already provide galvanic isolation, the main purposes of the use of a coupled inductor is to adjust voltage gains.

6 MODIFIED FLYBACK APPLIED IN CPT

6.1 Introduction

Based on the modified Buck-Boost, the simplified and idealized proposed system, presented in Figure 6.1, consists on a modified Flyback converter designed to transfer power through coupling capacitances. The step-down coupled inductor located in the secondary stage has the purpose of adjusting voltage gain, as some battery of some EVs are up to 60 V as in Renault Twizy [13]. As it will be presented in section 6.6, it also increases power transfer capability.

Figure 6.1 – Modified Ideal Flyback converter.
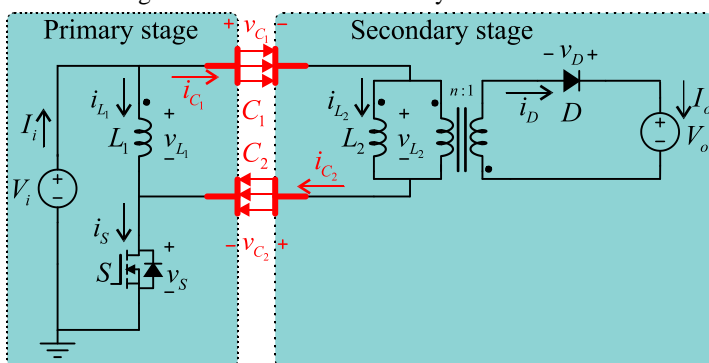
Source: Own elaboration.

An equivalent capacitance, as in (5.1) together with the reflected circuit as in (6.1) and (6.2) form an equivalent circuit as presented in Figure 6.2. For convenience, throughout this thesis it will be used this reflected equivalent circuit.

$$V_o^* = n\left(V_o + V_{D_{FWD}}\right) \tag{6.1}$$

$$I_o^* = \frac{I_o}{n} \tag{6.2}$$

Figure 6.2 – Equivalent circuit of the modified Flyback converter.
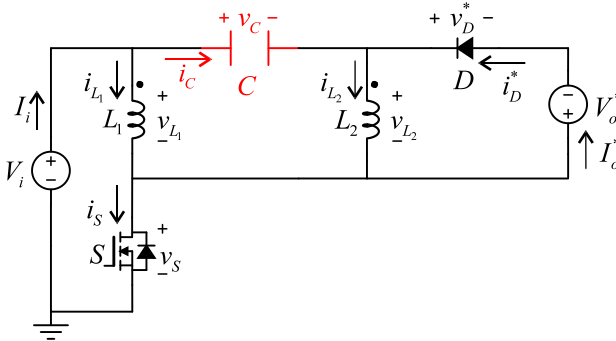
Source: Own elaboration.

As summarily presented in Figure 6.3, besides the common continuous conduction mode (CCM) and discontinuous current mode (DCM) well described in the literature, two different modes are identified [56] as the voltage across the diode might become forward-biased before the subinterval DT_s. The 4 observed modes are:

- 1) *Continuous conduction mode* (CCM): the switch conducts during the subinterval DT_s, while diode conducts current during the entire subinterval $(1-D)T_s$. This mode is the conventional CCM.

- 2) *Discontinuous current mode* (DCM): the switch conducts during the subinterval DT_s, while diode discharge completely before subinterval $(1-D)T_s$ ends. This mode operates as a CPL and is the conventional DCM.

- 3) *Discontinuous voltage mode* (DVM): the switch conducts during the subinterval DT_s, while diode starts to conduct before subinterval DT_s ends, and keeps conducting during the entire subinterval $(1-D)T_s$. Voltage across the switch becomes discontinuous. This mode operates as a constant power load (CPL) and is dual to DCM.

- 4) *Discontinuous quasi-resonant mode* (DQRM): the switch conducts during the subinterval DT_s, while diode starts to conduct before subinterval $(1-D)T_s$ ends, and discharge completely before the end of subinterval. This mode is an overlapping between DVM and DCM.

Figure 6.3 – Four possible operating modes.
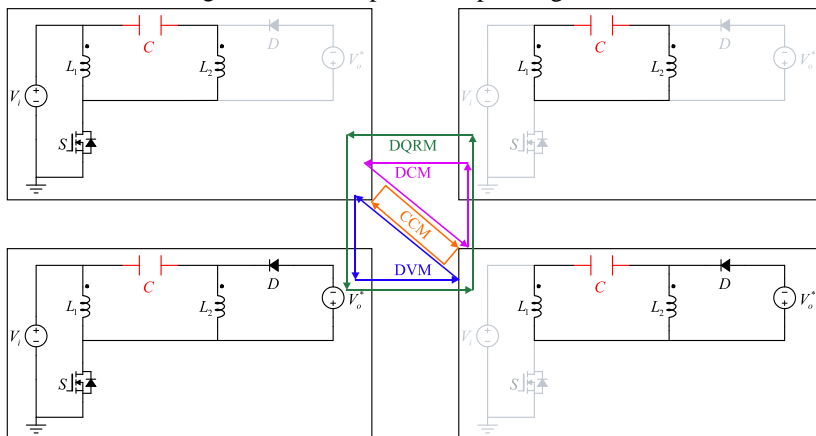
6.2 Continuous conduction mode (CCM)

The continuous conduction mode is defined by which the current in the diode is never zeroed, and at the same time, the diode never conducts together with the switch. Thus, this mode has two operating subintervals: in the first one, the switch S is conducting and the diode D is reverse biased, and the second one when the switch S is turned OFF and the diode D is conducting.

6.2.1 First subinterval

In this subinterval, the switch command in S is triggered, while diode D is naturally reverse biased as presented in Figure 6.4.

Figure 6.4 – First subinterval equivalent circuit in CCM.
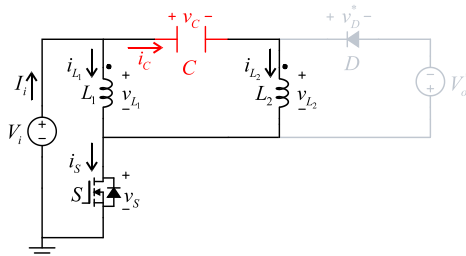
The inductor L_1 stores energy from the input source V_i. Thus, the current grows linearly, starting from a minimum initial value $I_{L_{1m}}$, as presented in (6.3).

$$i_{L_1}(t) = \frac{V_i}{L_1} t + I_{L_{1m}} \tag{6.3}$$

In the mesh containing the resonant circuit $L_2 C$, developing second order differential equation, the voltage across the capacitor behave as presented in [57]. Therefore, the voltage increases sinusoidally as shown in (6.4).

$$v_C(t) = V_i + \left(V_{C_m} - V_i\right)\cos(\omega_2 t) + I_{L_{2m}} \sqrt{\frac{L_2}{C}} \sin(\omega_2 t) \tag{6.4}$$

Where:
- V_i is the input voltage source (V);
- V_{C_m} is the minimum initial condition value $v_C(0)$ (V);
- $I_{L_{2m}}$ is the minimum initial condition value $i_C(0)$ (A);
- ω_2 is the natural angular frequency $\sqrt{\dfrac{1}{L_2 C}}$ (rad/s).

To find the expression of the current in the capacitor, simply derive (6.4), resulting in (6.5).

$$\sqrt{\frac{L_2}{C}} i_C(t) = \left(V_i - V_{C_m}\right)\sin(\omega_2 t) + I_{L_{2m}} \cos(\omega_2 t) \tag{6.5}$$

The current in the inductor L_2 is the same as that of the coupling capacitor as shown in (6.6).

$$i_{L_2}(t) = i_C(t) \tag{6.6}$$

Finally, the current in the switch and the voltage across the diode are defined, respectively by (6.7) and (6.8).

$$i_s(t) = i_{L_1}(t) + i_{L_2}(t) \tag{6.7}$$

$$v_D^*(t) = V_i + V_o^* - v_C(t) \tag{6.8}$$

6.2.2 Second subinterval

When the switch is commanded to block, the diode starts to conduct. Such equivalent circuit is presented in Figure 6.5.

Figure 6.5 – Second subinterval equivalent circuit in CCM.
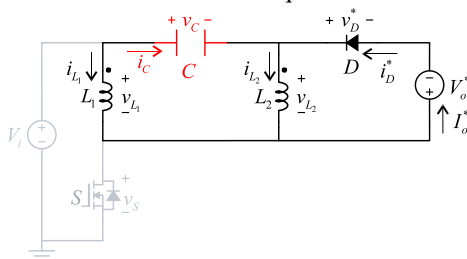
Source: Own elaboration.

Similar to the first subinterval, equations (6.9) and (6.10) express the behavior of the voltage and current across the coupling capacitor. In this subinterval, the energy stored in the reactive elements during the first subinterval is transferred to V_o^*. Therefore, the voltage V_o^*, which has opposite polarity of V_i, is imposed across the resonant circuit $L_1 C$ and across magnetizing inductance L_2, deenergizing them with second and first order behavior, respectively, according to (6.11) and (6.12).

$$v_C(t) = V_o^* + \left(V_{C_M} - V_o^*\right)\cos(\omega_1 t) - I_{L_{1M}}\sqrt{\frac{L_1}{C}}\sin(\omega_1 t) \tag{6.9}$$

$$\sqrt{\frac{L_1}{C}}i_C(t) = \left(V_o^* - V_{C_M}\right)\sin(\omega_1 t) - I_{L_{1M}}\cos(\omega_1 t) \tag{6.10}$$

Where:
- V_o^* is the reflected output voltage load (V);

- V_{C_M} is the maximum initial condition value $v_C(DT_s)$ (V);

- $I_{L_{1M}}$ is the maximum initial condition value $i_C(DT_s)$ (A);

- ω_1 is the natural angular frequency $\sqrt{\dfrac{1}{L_1 C}}$ (rad/s).

The current in the inductor L_1 is the same as that of the capacitor with opposite direction, according to (6.11).

$$i_{L_1}(t) = -i_C(t) \tag{6.11}$$

On the other hand, L_2 is demagnetized linearly, starting from a maximum value $I_{L_{2M}}$, as shown in (6.12)

$$i_{L_2}(t) = I_{L_{2M}} - \frac{V_o^*}{L_2} t \tag{6.12}$$

Finally, the current in the diode and the voltage across the switch are defined, respectively by (6.13) and (6.14).

$$i_D^*(t) = i_{L_1}(t) + i_{L_2}(t) \tag{6.13}$$

$$v_S(t) = V_i + V_o^* - v_C(t) \tag{6.14}$$

6.2.3 Waveforms

The main general waveforms of the currents and voltages in the switching and reactive elements and their maximum and minimum values for two switching periods are shown in Figure 6.6.

Figure 6.6 – Main general waveforms in CCM.
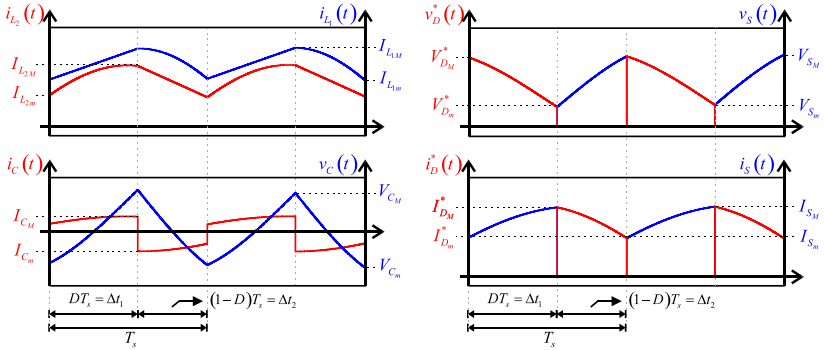
Source: Own elaboration.

6.2.4 Initial condition of the system equation

Once the behavior of the voltage and current on the storage elements in CCM presented in section 6.2 is known, it is necessary to express the initial conditions of the system as function of fixed variables such as input and output voltages, switching frequency, natural angular frequency and duty cycle.

As shown in Figure 6.6, the voltage V_{C_M} occurs at the instant Δt_1 for (6.4), as shown in (6.15). Meanwhile, the voltage V_{C_m} occurs at the instant Δt_2 for (6.9), according to (6.16).

$$V_{C_M} = V_i + \left(V_{C_m} - V_i\right)\cos\left(\omega_2 \Delta t_1\right) + I_{L_{2m}}\sqrt{\frac{L_2}{C}}\sin\left(\omega_2 \Delta t_1\right) \quad (6.15)$$

$$V_{C_m} = V_o^* + \left(V_{C_M} - V_o^*\right)\cos\left(\omega_1 \Delta t_2\right) - I_{L_{1M}}\sqrt{\frac{L_1}{C}}\sin\left(\omega_1 \Delta t_2\right) \quad (6.16)$$

The current $I_{L_{1m}}$ occurs at the instant Δt_2 for (6.11), as shown in (6.17). Meanwhile, the current $I_{L_{1M}}$ occurs at the instant Δt_1 for (6.3), according to (6.18).

$$\sqrt{\frac{L_1}{C}}I_{L_{1m}} = I_{L_{1M}}\cos\left(\omega_1 \Delta t_2\right) - \left(V_o^* - V_{C_M}\right)\sin\left(\omega_1 \Delta t_2\right) \quad (6.17)$$

$$I_{L_{1M}} = I_{L_{1m}} + \frac{V_i \Delta t_1}{L_1} \tag{6.18}$$

Substituting (6.18) in (6.17) and manipulating the equation results in (6.19). And, substituting (6.19) in (6.18), results in (6.20).

$$I_{L_{1m}} = \frac{\left(V_{C_M} - V_o^*\right)\sqrt{\dfrac{C}{L_1}}\sin\left(\omega_1 \Delta t_2\right) + \dfrac{V_i \Delta t_1}{L_1}\cos\left(\omega_1 \Delta t_2\right)}{1 - \cos\left(\omega_1 \Delta t_2\right)} \tag{6.19}$$

$$I_{L_{1M}} = \frac{\left(V_{C_M} - V_o^*\right)\sqrt{\dfrac{C}{L_1}}\sin\left(\omega_1 \Delta t_2\right) + \dfrac{V_i \Delta t_1}{L_1}}{1 - \cos\left(\omega_1 \Delta t_2\right)} \tag{6.20}$$

The current $I_{L_{2M}}$ occurs at the instant Δt_1 for (6.6), as shown in (6.21). Meanwhile, the current $I_{L_{2m}}$ occurs at the instant Δt_2 for (6.12), according to (6.22).

$$\sqrt{\frac{L_2}{C}}I_{L_{2M}} = \left(V_i - V_{C_m}\right)\sin\left(\omega_2 \Delta t_1\right) + I_{L_{2m}}\cos\left(\omega_2 \Delta t_1\right) \tag{6.21}$$

$$I_{L_{2m}} = I_{L_{2M}} - \frac{V_o^* \Delta t_2}{L_2} \tag{6.22}$$

Substituting (6.22) in (6.21) and manipulating the equation, results in (6.23). And substituting (6.23) in (6.22), it results in (6.24).

$$I_{L_{2M}} = \frac{\left(V_i - V_{C_m}\right)\sqrt{\dfrac{C}{L_2}}\sin\left(\omega_2 \Delta t_1\right) - \dfrac{V_o^* \Delta t_2}{L_2}\cos\left(\omega_2 \Delta t_1\right)}{1 - \cos\left(\omega_2 \Delta t_1\right)} \tag{6.23}$$

$$I_{L_{2m}} = \frac{\left(V_i - V_{C_m}\right)\sqrt{\dfrac{C}{L_2}}\sin\left(\omega_2\Delta t_1\right) - \dfrac{V_o^*\Delta t_2}{L_2}}{1 - \cos\left(\omega_2\Delta t_1\right)} \tag{6.24}$$

Then, substituting (6.20) in (6.16), and substituting this result together with the substitution result of (6.24) in (6.15), results in an expression V_{C_M} as a function of V_i, V_o^* and V_{C_m} as in (6.25).

$$\begin{aligned}
V_{C_M} &= \left(1 - \cos\left(\omega_2\Delta t_1\right) + \frac{\sin^2\left(\omega_2\Delta t_1\right)}{1 - \cos\left(\omega_2\Delta t_1\right)}\right)V_i \\
&\quad - \left(\sqrt{\frac{L_2}{C}}\frac{\Delta t_2}{L_2} + \frac{\sin\left(\omega_2\Delta t_1\right)}{1 - \cos\left(\omega_2\Delta t_1\right)}\right)V_o^* \\
&\quad + \left(\cos\left(\omega_2\Delta t_1\right) - \frac{\sin^2\left(\omega_2\Delta t_1\right)}{1 - \cos\left(\omega_2\Delta t_1\right)}\right)V_{C_m}
\end{aligned} \tag{6.25}$$

Using trigonometric identity, (6.25) is rewritten as (6.26).

$$V_{C_M} = 2V_i - \left(\sqrt{\frac{L_2}{C}}\frac{\Delta t_2}{L_2} + \frac{\sin\left(\omega_2\Delta t_1\right)}{1 - \cos\left(\omega_2\Delta t_1\right)}\right)V_o^* - V_{C_m} \tag{6.26}$$

In an analogous way, the expression of V_{C_m} as a function of V_i, V_o^* and V_{C_M} is presented in (6.27).

$$V_{C_m} = -\left(\sqrt{\frac{L_1}{C}}\frac{\Delta t_1}{L_1} + \frac{\sin\left(\omega_1\Delta t_2\right)}{1 - \cos\left(\omega_1\Delta t_2\right)}\right)V_i + 2V_o^* - V_{C_M} \tag{6.27}$$

Substituting (6.27) in (6.26), it is found the static gain of the output voltage V_o^* by the input voltage V_i of the converter in CCM, according to (6.28).

$$G_{CCM} = \frac{V_o^*}{V_i} = \frac{2 + \sqrt{\dfrac{L_1}{C}}\,\dfrac{\Delta t_1}{L_1}\,\dfrac{\sin(\omega_1 \Delta t_2)}{1 - \cos(\omega_1 \Delta t_2)}}{2 + \sqrt{\dfrac{L_2}{C}}\,\dfrac{\Delta t_2}{L_2}\,\dfrac{\sin(\omega_2 \Delta t_1)}{1 - \cos(\omega_2 \Delta t_1)}} \tag{6.28}$$

Knowing that the instants Δt_1 and Δt_2 are defined by (6.29) and (6.30), respectively:

$$\Delta t_1 = DT_s = \frac{D}{f_s} \tag{6.29}$$

$$\Delta t_2 = (1 - D)T_s = \frac{1 - D}{f_s} \tag{6.30}$$

And that, by trigonometric identity:

$$\frac{\sin(x)}{1 - \cos(x)} = \cot\left(\frac{x}{2}\right) \tag{6.31}$$

Let the following relationships be:

$$\mu_1 = \frac{2\pi f_s}{\omega_1} \tag{6.32}$$

$$\mu_2 = \frac{2\pi f_s}{\omega_2} \tag{6.33}$$

The static gain can then be rewritten as a function of D, μ_1 and μ_2, according to (6.34).

$$G_{CCM}(D, \mu_1, \mu_2) = \frac{V_o^*}{V_i} = \frac{1 + \dfrac{\pi D}{\mu_1}\cot\left(\dfrac{\pi(1 - D)}{\mu_1}\right)}{1 + \dfrac{\pi(1 - D)}{\mu_2}\cot\left(\dfrac{\pi D}{\mu_2}\right)} \tag{6.34}$$

Static gain analysis will be better comprehended in the section 6.2.6. For the time being, the objective remains to find the initial conditions as a function of fixed variables.

The average value of the current in the inductor L_2 is the integral of the sum between (6.6) and (6.12) over the corresponding switching period as shown in (6.35), resulting in (6.36).

$$I_{L_{2avg}} = \frac{1}{T_s} \int_0^{T_s} i_{L_2}(t) = \frac{1}{T_s} \left(\int_0^{\Delta t_1} i_{L_2}(t)dt + \int_0^{\Delta t_2} i_{L_2}(t)dt \right) \quad (6.35)$$

$$I_{L_{2avg}} = \frac{I_{L_{2m}} + I_{L_{2M}}}{2} D + \frac{C}{T_s} \left[\begin{array}{l} I_{L_{2m}} \sqrt{\frac{L_2}{C}} \sin(\omega_2 \Delta t_1) + \\ (V_{C_m} - V_i)(\cos(\omega_2 \Delta t_1) - 1) \end{array} \right] \quad (6.36)$$

The current $I_{L_{2avg}}$ is equivalent to the output load current I_o^*, that conveniently is defined in terms of the output voltage V_o^* and a reflected output load resistance R_o^*, as presented in (6.37).

$$I_{L_{2avg}} = I_o^* = \frac{V_o^*}{R_o^*} \quad (6.37)$$

Knowing that $I_{L_{2m}}$ and $I_{L_{2M}}$ are defined in terms of V_i, V_o^* and V_{C_m} as in (6.24) and (6.23), receptively, it is now possible to express V_{C_m} as a function of V_i, V_o^* and R_o^* by substituting (6.24), (6.23) and (6.37) in (6.36), resulting in (6.38).

$$\frac{V_o^*}{R_o^*} = AV_i - AV_{C_m} - BV_o^* \quad (6.38)$$

In which the values A and B are, respectively, expressed in (6.39) and (6.40).

$$A = \sqrt{\frac{C}{L_2}}(1-D)\cot\left(\frac{\pi D}{\mu_2}\right) + 2Cf_s \tag{6.39}$$

$$B = \frac{(1-D)^2}{2f_sL_2}\frac{1+\cos(\omega_2 DT_s)}{1-\cos(\omega_2 DT_s)} + \sqrt{\frac{C}{L_2}}(1-D)\cot\left(\frac{\pi D}{\mu_2}\right) \tag{6.40}$$

Considering the static gain in (6.34) and rearranging (6.38), V_{C_m} is expressed in (6.41).

$$V_{C_m} = \varepsilon_m V_i \tag{6.41}$$

$$\varepsilon_m = 1 - \frac{G_{CCM}}{A}\left(B + \frac{1}{R_o^*}\right) \tag{6.42}$$

The term A, shown in (6.39), can be better presented as (6.43). The division of the term B by the term A, results in simplification presented in (6.44).

$$A = 2Cf_s\left(1 + \frac{\pi(1-D)}{\mu_2}\cot\left(\frac{\pi D}{\mu_2}\right)\right) \tag{6.43}$$

$$\frac{B}{A} = \frac{\pi(1-D)}{\mu_2}\cot\left(\frac{\pi D}{\mu_2}\right) \tag{6.44}$$

Finally, ε_m in a more simplified form is presented in (6.45).

$$\varepsilon_m = 1 - G_{CCM}\left(\frac{\dfrac{\pi(1-D)}{\mu_2}\cot\left(\dfrac{\pi D}{\mu_2}\right) +}{} + \frac{1}{2f_sCR_o^*\left(1 + \dfrac{\pi(1-D)}{\mu_2}\cot\left(\dfrac{\pi D}{\mu_2}\right)\right)}\right) \tag{6.45}$$

Substituting (6.41) in (6.26) and following the same simplification process used to find V_{C_m}, V_{C_M} is expressed as in (6.46).

$$V_{C_M} = \varepsilon_M V_i \tag{6.46}$$

$$\varepsilon_M = 1 - G_{CCM} \left(\dfrac{\dfrac{\pi(1-D)}{\mu_2} \cot\left(\dfrac{\pi D}{\mu_2}\right) +}{- \dfrac{1}{2 f_s C R_o^* \left(1 + \dfrac{\pi(1-D)}{\mu_2} \cot\left(\dfrac{\pi D}{\mu_2}\right)\right)}} \right) \tag{6.47}$$

Once the expressions for V_{C_m} and V_{C_M} are found as a function of fixed variables, it is now possible to find the expressions for $I_{L_{1m}}$, $I_{L_{1M}}$, $I_{L_{2m}}$ and $I_{L_{2M}}$ as functions of the same variables. Substituting (6.41) and (6.46) in (6.19), (6.20), (6.23) and (6.24); performing the necessary mathematical manipulations, the values $I_{L_{1m}}$, $I_{L_{1M}}$, $I_{L_{2m}}$ and $I_{L_{2M}}$ are redefined as presented in (6.48), (6.49), (6.50), and (6.51), respectively:

$$I_{L_{1m}} = 2\pi f_s C V_i \cot\left(\dfrac{\pi(1-D)}{\mu_1}\right) \left(\dfrac{\varepsilon_M - G_{CCM}}{\mu_1} + \dfrac{2\pi D}{\mu_1^2} \cot\left(\dfrac{2\pi(1-D)}{\mu_1}\right) \right) \tag{6.48}$$

$$I_{L_{1M}} = 2\pi f_s C V_i \cot\left(\dfrac{\pi(1-D)}{\mu_1}\right) \left(\dfrac{\varepsilon_M - G_{CCM}}{\mu_1} + \dfrac{2\pi D}{\mu_1^2} \dfrac{1}{\sin\left(\dfrac{2\pi(1-D)}{\mu_1}\right)} \right) \tag{6.49}$$

$$I_{L_{2m}} = 2\pi f_s C V_i \cot\left(\frac{\pi D}{\mu_2}\right)\left(\frac{1-\varepsilon_m}{\mu_2} - \frac{2\pi(1-D)G_{CCM}}{\mu_2{}^2}\frac{1}{\sin\left(\frac{2\pi D}{\mu_2}\right)}\right) \quad (6.50)$$

$$I_{L_{2M}} = 2\pi f_s C V_i \cot\left(\frac{\pi D}{\mu_2}\right)\left(\frac{1-\varepsilon_m}{\mu_2} - \frac{2\pi(1-D)G_{CCM}}{\mu_2{}^2}\cot\left(\frac{2\pi D}{\mu_2}\right)\right) \quad (6.51)$$

It is concluded in this section that the values of the initial conditions of the system could be expressed as function of known parameters in a project. Note, however, that such values are a function of a resistive load R_o^*, which is not very favorable to interpret the load characteristic in a generic manner.

6.2.5 Parametrization

Before starting the load characteristic section of the converter, it is necessary to have a parametrization of the output current so that the functions are dimensionless and independent of the load resistance, making it possible to characterize the converter in a generic and dimensionless way. Thus, equation (6.45) can be rewritten as shown in (6.52). Defining the parametrized output current γ according to (6.53), ε_m is defined as a function of γ as shown in (6.54). Following the same steps, ε_M can be defined as in (6.55).

$$\varepsilon_m = 1 - G_{CCM}\frac{\pi(1-D)}{\mu_2}\cot\left(\frac{\pi D}{\mu_2}\right) - $$
$$\frac{V_o^* I_o^*}{V_o^* 2 f_s C V_i\left(1+\frac{\pi(1-D)}{\mu_2}\cot\left(\frac{\pi D}{\mu_2}\right)\right)} \quad (6.52)$$

$$\gamma = \frac{I_o^*}{2 f_s C V_i} \quad (6.53)$$

$$\varepsilon_{m}\left(\gamma\right)=1-G_{CCM}\,\frac{\pi\left(1-D\right)}{\mu_{2}}\cot\left(\frac{\pi D}{\mu_{2}}\right)-$$

$$\frac{1}{\left(1+\dfrac{\pi\left(1-D\right)}{\mu_{2}}\cot\left(\dfrac{\pi D}{\mu_{2}}\right)\right)^{\gamma}}\gamma \qquad (6.54)$$

$$\varepsilon_{M}\left(\gamma\right)=1-G_{CCM}\,\frac{\pi\left(1-D\right)}{\mu_{2}}\cot\left(\frac{\pi D}{\mu_{2}}\right)+$$

$$\frac{1}{\left(1+\dfrac{\pi\left(1-D\right)}{\mu_{2}}\cot\left(\dfrac{\pi D}{\mu_{2}}\right)\right)^{\gamma}}\gamma \qquad (6.55)$$

Dividing the equations expressing the maximum and minimum values of the currents in the inductors, presented in (6.48), (6.49), (6.50) and (6.51) by the output current I_{o}^{*} and using (6.53), (6.54) and (6.55), it is defined the parametrized relations (6.56), (6.58) (6.60) and (6.62).

$$\delta_{L_{1m}}\left(\gamma\right)=\frac{\pi}{\gamma}\cot\left(\frac{\pi\left(1-D\right)}{\mu_{1}}\right)\left(\begin{array}{c}\dfrac{\varepsilon_{M}\left(\gamma\right)-G_{CCM}}{\mu_{1}}+\\[2ex]+\dfrac{2\pi D}{\mu_{1}^{2}}\cot\left(\dfrac{2\pi\left(1-D\right)}{\mu_{1}}\right)\end{array}\right) \qquad (6.56)$$

$$\delta_{L_{1m}}=\frac{I_{L_{1m}}}{I_{o}^{*}} \qquad (6.57)$$

$$\delta_{L_{1M}}\left(\gamma\right)=\frac{\pi}{\gamma}\cot\left(\frac{\pi\left(1-D\right)}{\mu_{1}}\right)\left(\begin{array}{c}\dfrac{\varepsilon_{M}\left(\gamma\right)-G_{CCM}}{\mu_{1}}+\\[2ex]+\dfrac{2\pi D}{\mu_{1}^{2}}\dfrac{1}{\sin\left(\dfrac{2\pi\left(1-D\right)}{\mu_{1}}\right)}\end{array}\right) \qquad (6.58)$$

$$\delta_{L_{1M}} = \frac{I_{L_{1M}}}{I_o^*} \tag{6.59}$$

$$\delta_{L_{2m}}(\gamma) = \frac{\pi}{\gamma}\cot\left(\frac{\pi D}{\mu_2}\right)\left(\frac{1-\varepsilon_m(\gamma)}{\mu_2} - \frac{2\pi(1-D)G_{CCM}}{\mu_2^2}\frac{1}{\sin\left(\frac{2\pi D}{\mu_2}\right)}\right) \tag{6.60}$$

$$\delta_{L_{2m}} = \frac{I_{L_{2m}}}{I_o^*} \tag{6.61}$$

$$\delta_{L_{2M}}(\gamma) = \frac{\pi}{\gamma}\cot\left(\frac{\pi D}{\mu_2}\right)\left(\frac{1-\varepsilon_m(\gamma)}{\mu_2} - \frac{2\pi(1-D)G_{CCM}}{\mu_2^2}\cot\left(\frac{2\pi D}{\mu_2}\right)\right) \tag{6.62}$$

$$\delta_{L_{2M}} = \frac{I_{L_{2M}}}{I_o^*} \tag{6.63}$$

6.2.6 Static gain

The static gain G_{CCM} presented in (6.34) represents the relation between the output and input voltages of the converter considering no loss and does not neglect the voltage ripple across the coupling capacitor. Due to the high voltage and current ripples across the coupling capacitors and inductors, the CCM static gain found in classical converters presented in (5.5) might not be applicable. In Figure 6.7, it is presented the static gain for different parameters and the conventional static.

Figure 6.7– Static gain for different parameter combinations.
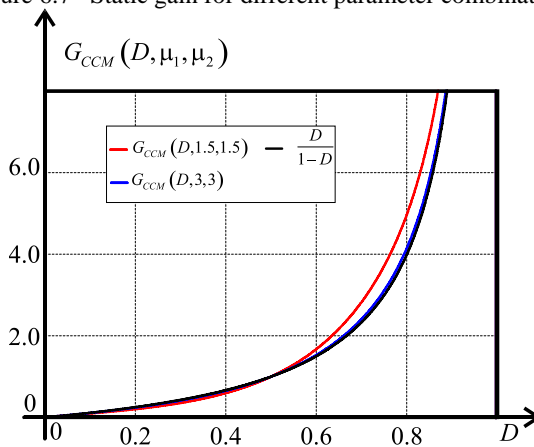
Source: Own elaboration.

Figure 6.8 presents the static gain behavior (6.34) normalized with respect to conventional static gain for different parameter combinations. Notice that, depending on the reactive elements, duty cycle and switching frequency, an error of up to 30%, for example, can be expected if conventional static gain is used. In fact, for higher ratio values (≥ 3), the error compared to conventional static gain is kept within 6%, whereas special care must be taken for lower ratio values (≤ 3). Therefore, depending on the reactive elements and the switching frequency, small ripple approximation cannot be used to find the precise static gain. Another conclusion is that, as shown in Figure 6.8 (b), if $\mu_1 > \mu_2$, the static gain tends to present higher values. Conversely, if $\mu_1 < \mu_2$, the static gain tends to present lower values. Such characteristic can also be used to adjust static gain, without the need of adjusting duty cycle or turns ratio.

Figure 6.8 – Normalized static gain for different parameter combinations: (a) for $\mu_1 = \mu_2$, (b) for $\mu_1 \neq \mu_2$.

(a)   (b)
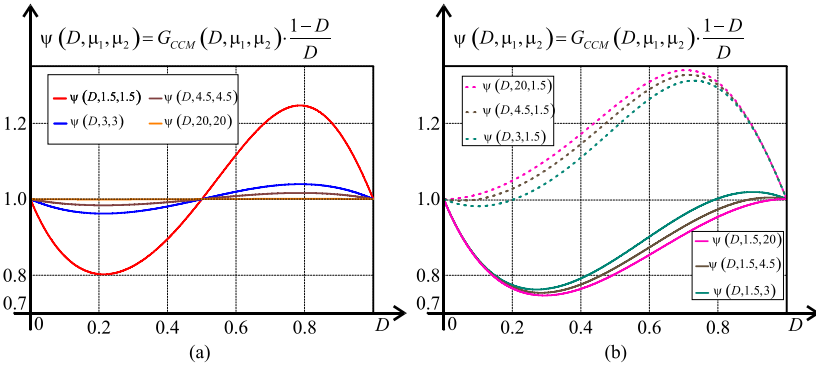
Source: Own elaboration.

Naturally, the static gain of the converter must present a monotonic, continuous, positive and increasing characteristic with the increment of D in the CCM region. Therefore, if there are values of μ_1, μ_2 or D that do not satisfy these conditions, it may indicate that the converter conducts in another region or is not realizable with these parameters.

Equation (6.34) presents cotangent terms, which requires careful analysis. The cotangent function in the trigonometric circle is shown in Figure 6.9. Note that it is continuous for arguments between 0 and π.

Figure 6.9 – Cotangent function in the trigonometric function.
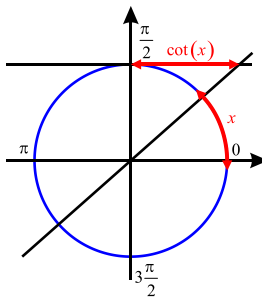
Source: Own elaboration.

In this context, the arguments in the terms with cotangent presented in (6.34) are comprehended in the domain as shown in (6.64) and (6.65).

$$0 < \frac{\pi(1-D)}{\mu_1} < \pi \qquad (6.64)$$

$$0 < \frac{\pi D}{\mu_2} < \pi \qquad (6.65)$$

Knowing that D varies from 0 to 1, a necessary condition for the converter to operate in CCM is given in (6.66).

$$\mu_{1,2} > 1 \qquad (6.66)$$

Notice that the higher the ratios μ_1 and μ_2, the more the converter's static gain is assimilated to that of a conventional gain. Such analysis is proven by analyzing the limits of these ratios in (6.34) tending to infinity. Applying the concept of the limit of a cotangent function presented in (6.67), the limits of the numerator and denominator behave, respectively, according to (6.68) and (6.69). Thus, the static gain with both ratios tending to infinity is the same as that of the conventional converter, as proved in (6.70).

$$\lim_{x \to \infty} \frac{\pi}{x} \cot\left(\frac{\pi}{x}\alpha\right) = \frac{1}{\alpha} \qquad (6.67)$$

$$\lim_{\mu_1 \to \infty} 1 + \frac{\pi D}{\mu_1} \cot\left(\frac{\pi(1-D)}{\mu_1}\right) = 1 + \frac{D}{1-D} = \frac{1}{1-D} \qquad (6.68)$$

$$\lim_{\mu_1 \to \infty} 1 + \frac{\pi(1-D)}{\mu_2} \cot\left(\frac{\pi D}{\mu_2}\right) = 1 + \frac{1-D}{D} = \frac{1}{D} \qquad (6.69)$$

$$\lim_{\mu_{1,2} \to \infty} G_{CCM}\left(D, \mu_1, \mu_2\right) = \frac{D}{1-D} \qquad (6.70)$$

Also, in relation to the gain G_{CCM}, the limits can also be used to analyze the behavior of the converter for D tending to 0 or 1. When D tends to 0, the numerator tends to the constant number 1, while the

denominator tends to infinity, resulting in (6.71). When D tends to 1, the numerator tends to infinity, while the denominator tends to the constant number 1, resulting in (6.72).

$$\lim_{D \to 0} G_{CCM}\left(D, \mu_1, \mu_2\right) = 0 \tag{6.71}$$

$$\lim_{D \to 1} G_{CCM}\left(D, \mu_1, \mu_2\right) = \infty \tag{6.72}$$

When the input and output voltage sources are imposed, the static gain is also imposed. From the expression presented in (6.34), it is developed the condition for operating in CCM, as presented in (6.73). It is not possible to fully isolate D, however, numerically, it is possible to evaluate if the converter operates in CCM. If the limits to infinity presented in (6.68) and (6.69) are applied, then the condition can be simplified as in conventional converter according to (6.74).

$$D = \frac{G_{CCM} + \dfrac{G_{CCM}\,\pi}{\mu_2}\cot\left(\dfrac{\pi D}{\mu_2}\right) - 1}{\dfrac{G_{CCM}\,\pi}{\mu_2}\cot\left(\dfrac{\pi D}{\mu_2}\right) + \dfrac{\pi}{\mu_1}\cot\left(\dfrac{\pi(1-D)}{\mu_1}\right)} \tag{6.73}$$

$$\lim_{\mu_{1,2} \to \infty} D = \frac{G_{CCM}}{1 + G_{CCM}} = \frac{V_o^*}{V_o^* + V_i} \tag{6.74}$$

6.2.6.1 Voltage ripple across the coupling capacitor

Shown in Figure 6.6, the ripple of the voltage across the capacitor C in steady state is obtained by subtracting V_{C_M} expressed in (6.55) from V_{C_m} presented in (6.54), as presented in (6.76). Using the approximation deduced in (6.70), the voltage variation across the coupling capacitor can be approximated as presented in (6.77). The voltage ripple in C_1 and C_2 are found by dividing by two, if (5.4) is assumed, as shown in (6.78). Note the importance of high switching frequencies and capacitances values to minimize the voltage ripple value ΔV_C. It is also concluded that in light load conditions or low gains, the voltage excursion is smaller, whereas in

heavy load conditions or large gains, the voltage excursion is larger, approaching this way DVM.

$$\Delta V_C = \Delta\varepsilon V_i \tag{6.75}$$

$$\Delta\varepsilon = \frac{2}{\left(1 + \frac{\pi(1-D)}{\mu_2}\cot\left(\frac{\pi D}{\mu_2}\right)\right)}\gamma \tag{6.76}$$

$$\Delta\varepsilon \simeq 2\gamma D = \frac{1}{f_s C R_o^*}\frac{D^2}{1-D} \tag{6.77}$$

$$\Delta V_{C_{1,2}} = \frac{\Delta\varepsilon V_i}{2} \tag{6.78}$$

6.2.6.2 Voltage ripple across the output capacitor

When switch is turned ON, the output capacitor C_o supplies energy to the load. The average value of the discharge current during the subinterval Δt_1 is the output average load current I_o , but no longer reflected, as presented in (6.79).

$$\Delta V_{C_o} = \frac{1}{C_o}\int_0^{\Delta t_1} I_o dt = \frac{I_o \Delta t_1}{C_o} = \frac{I_o D}{f_s C_o} \tag{6.79}$$

6.2.6.3 Maximum voltage across switching elements

The maximum peak voltage across the active switch is presented in (6.80), whereas the maximum peak voltage across the diode is presented in (6.81).

$$V_{S_{\max}} = \left(1 + G_{CCM} - \varepsilon_{\mathrm{m}}\right)V_i \tag{6.80}$$

$$V_{D_{\max}} = \frac{V_{S_{\max}}}{n} \tag{6.81}$$

6.2.6.4 Current ripple in the inductors

The ripples of the currents in the inductors shown in Figure 6.6 are obtained by subtracting their respective maximum and minimum values. From (6.18) and (6.22), the ripple is obtained for I_{L_1} in (6.82) and for I_{L_2} in (6.84). If the static gain approaches the static gain of a conventional Flyback converter, the expression (6.84) can be approximated, thus resembling the expression for classical converters. The parametrized current ripple of the inductors L_1 and L_2 are presented in (6.83) and (6.85), respectively. Note that, dual to the voltage ripple across the coupling capacitor, the current ripples in the inductors becomes smaller for heavy loads and larger for light loads, approaching the DCM.

$$\Delta I_{L_1} = \frac{V_i \Delta t_1}{L_1} = \frac{V_i D}{L_1 f_s} \tag{6.82}$$

$$\frac{\Delta I_{L_1}}{I_o^*} = \Delta \delta_{L_1} = \frac{2\pi^2 D}{\mu_1^2} \frac{1}{\gamma} \tag{6.83}$$

$$\Delta I_{L_2} = \frac{V_o^*(1-D)}{L_2 f_s} = \frac{G_{CCM} V_i (1-D)}{L_2 f_s} \cong \frac{V_i D}{L_2 f_s} \tag{6.84}$$

$$\frac{\Delta I_{L_2}}{I_o^*} = \Delta \delta_{L_2} = \frac{2\pi^2 (1-D) G_{CCM}}{\mu_2^2} \frac{1}{\gamma} \tag{6.85}$$

6.2.6.5 RMS current value expression

The RMS values are deduced using the initial conditions found in section 6.2.4. The RMS value of the current in the inductor L_1 is expressed in (6.86).

$$I_{L_{1RMS}} = \sqrt{I_{L_{1a}}^2 + I_{L_{1b}}^2} \tag{6.86}$$

$$I_{L_{1a}} = \sqrt{\frac{1}{T_s} \int_0^{DT_s} \left[\left(\frac{V_i}{L_1} t + I_{L_{1m}} \right)^2 dt \right]} \tag{6.87}$$

$$I_{L_{1_b}} = \sqrt{\frac{1}{T_s} \int_0^{(1-D)T_s} \left[\left(I_{L_{1M}} \cos(\omega_1 t) + \sqrt{\frac{C}{L_1}} \left(V_{C_M} - V_o^* \right) \sin(\omega_1 t) \right)^2 dt \right]} \quad (6.88)$$

The RMS value of the current in the primary winding of inductor L_2 is expressed in (6.89).

$$I_{L_{2P_{RMS}}} = \sqrt{I_{L_{1_b}}^2 + I_{L_{2_a}}^2} \quad (6.89)$$

$$I_{L_{2_a}} = \sqrt{\frac{1}{T_s} \int_0^{DT_s} \left[\left(\sqrt{\frac{C}{L_2}} \left(V_i - V_{C_m} \right) \sin(\omega_2 t) + I_{L_{2m}} \cos(\omega_2 t) \right)^2 dt \right]} \quad (6.90)$$

The RMS value of the current in the secondary winding of inductor L_2 is expressed in (6.91).

$$I_{L_{2S_{RMS}}} = \sqrt{\frac{1}{T_s} \int_0^{(1-D)T_s} \left[\left(n \left(\begin{array}{c} \sqrt{\frac{C}{L_1}} \left(V_{C_M} - V_o^* \right) \sin(\omega_1 t) + \\ + I_{L_{1M}} \cos(\omega_1 t) - \frac{V_o^*}{L_2} t + I_{L_{2M}} \end{array} \right) \right)^2 \right] dt} \quad (6.91)$$

The RMS value of the current in the coupling capacitor C is expressed in (6.92).

$$I_{C_{RMS}} = I_{L_{2P_{RMS}}} \quad (6.92)$$

The RMS value of the current in the active switch S is expressed in (6.93).

$$I_{S_{RMS}} = \sqrt{\frac{1}{T_s} \int_0^{DT_s} \left[\left(\begin{array}{c} \sqrt{\frac{C}{L_2}} \left(V_i - V_{C_m} \right) \sin(\omega_2 t) + I_{L_{2m}} \cos(\omega_2 t) \\ + \frac{V_i}{L_1} t + I_{L_{1m}} \end{array} \right)^2 \right] dt} \quad (6.93)$$

The RMS value of the current in the diode D is expressed in (6.94).

$$I_{D_{RMS}} = I_{L_{2S_{RMS}}} \qquad (6.94)$$

The RMS value of the current in the output filter capacitor C_o is expressed in (6.95).

$$I_{C_{o_{RMS}}} = \sqrt{I_{D_{RMS}}^2 - I_o^2} \qquad (6.95)$$

6.3 Discontinuous Conduction Mode (DCM)

The DCM is defined by the current discontinuity in the diode D during subinterval Δt_2. Thus, in addition to the two subintervals in CCM mode presented in section 6.2, there is a third subinterval in which the current in the diode is zeroed. Due to its zero-current switching (ZCS) and inherent power factor correction (PFC) features, this region is largely used for switched-mode power supplies (SMPS) purposes.

6.3.1 Third subinterval for DCM

The equivalent circuit of this subinterval is shown in Figure 6.10

Figure 6.10 – Equivalent circuit of the third subinterval in DCM.
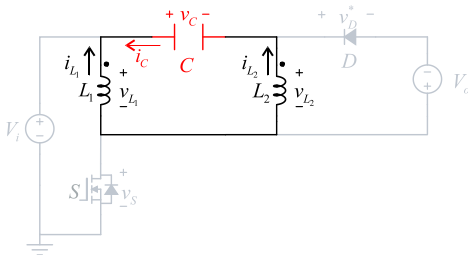
Source: Own elaboration.

All the equations of the reactive elements during the first two subintervals as a function of time presented in section 6.2: (6.3), (6.4), (6.5), (6.6), (6.9), (6.10), (6.11) and (6.12) remain valid. Note, however, that Δt_2 will no longer be expressed by (6.30), but rather by the instant in

which diode current is completely discharged. Note also that the initial conditions presented in section 6.3 is not satisfied in DCM, since the system of equations are different.

The system of equations in DCM presents three more fundamental equations for its resolution. The first one is the determination of the instant when the diode is discharged. The current in the diode is the sum of the currents in the inductor L_1, shown in (6.11) and in L_2, shown in (6.12). The subinterval for which the current is zeroed is presented in in (6.96). This equation is nonlinear, so that a numerical method is needed.

$$
\begin{aligned}
\Delta t_2 &= root\left(i_D\left(t\right)\right) \\
&= root\left(\begin{aligned} &\sqrt{\frac{C}{L_1}}\left(I_{L_{1M}}\cos\left(\omega_1 t\right)-\left(V_o^*-V_{C_M}\right)\sin\left(\omega_1 t\right)\right)+ \\ &+I_{L_{2M}}-\frac{V_o^*}{L_2}t \end{aligned} \right)
\end{aligned} \tag{6.96}
$$

The other equations are obtained from the equivalent circuit's homogenous second order differential equation as shown in (6.97), which its solution is presented in (6.98).

$$
v_C\left(t\right)+L_1 C\frac{d^2 v_C\left(t\right)}{dt^2}+L_2 C\frac{d^2 v_C\left(t\right)}{dt^2}=0 \tag{6.97}
$$

$$
v_C\left(t\right)=V_{C_o}\cos(\omega_e t)+I_{C_o}\sqrt{\frac{L_1+L_2}{C}}\sin\left(\omega_e t\right) \tag{6.98}
$$

Where:

- V_{C_o} is the voltage initial condition value $v_C\left(\Delta t_2\right)$ (V);

- I_{C_o} is the current initial condition value $i_C\left(\Delta t_2\right)$ (A);

- ω_e is the natural angular frequency $\sqrt{\dfrac{1}{L_1+L_2\ C}}$ (rad/s).

From the derivation of (6.98), it is obtained the expression of the current in the capacitor C, which is the same for both inductors, according to (6.100) and (6.101).

$$\sqrt{\frac{L_1 + L_2}{C}} i_C(t) = -V_{C_o} \cos(\omega_e t) + I_{C_o} \cos(\omega_e t) \qquad (6.99)$$

$$i_{L_1}(t) = -i_C(t) \qquad (6.100)$$

$$i_{L_2}(t) = i_C(t) \qquad (6.101)$$

As it can be seen, solving the system of equations to find the initial conditions and static gain in DCM is complicated and time consuming. However, as in an ordinary Flyback, the modified converter still maintains its constant power load (CPL) characteristic in DCM. This information is important and useful for determining the load characteristic and static gain in DCM, as it will be demonstrated in section 6.3.2.1.

6.3.2 Waveforms

The main general waveforms of the currents and voltages in the switching and reactive elements are shown in Figure 6.11. Notice that, there is a small voltage excursion across switching elements, whereas a large current ripple is observed as expected in DCM.

Figure 6.11 – General main waveforms in DCM.
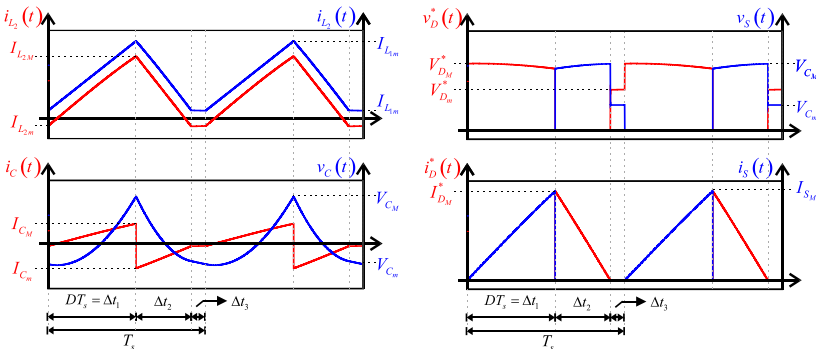
Source: Own elaboration.

6.3.2.1 Load characteristic and boundary condition in DCM

The boundary condition for the converter to reach DCM mode is presented in (6.102).

$$I_{L_{1m}} + I_{L_{2m}} = 0 \tag{6.102}$$

Substituting (6.56) and (6.58) in (6.102), the condition is defined in dimensionless terms as (6.103)

$$\delta_{L_{1m}} + \delta_{L_{2m}} = 0 \tag{6.103}$$

Knowing that in the DCM region, the converter behaves as a CPL, then, there is a critical minimum power P_{DCM} for which the converter is able to supply:

$$P_{\min} = P_{DCM} = V_o^* I_{oDCM}^* = G_{CCM} V_i I_{oDCM}^* \tag{6.104}$$

$$I_{oDCM}^* = 2 f_s C V_i \gamma_{DCM} \tag{6.105}$$

The value γ_{DCM} is found computationally from the expression (6.106). Therefore, P_{DCM} can be expressed by (6.107).

$$\gamma_{DCM} = root\left(\delta_{L_{1m}}(\gamma) + \delta_{L_{2m}}(\gamma)\right) \tag{6.106}$$

$$P_{DCM} = G_{CCM} V_i^2 \, 2 f_s C \gamma_{DCM} \tag{6.107}$$

For each γ_{DCM}, the static gain in DCM is defined by (6.108). Using the definition of the output parameterize current in (6.53), the static gain in DCM as a function of γ is presented in (6.109).

$$\frac{V_o^*}{V_i} = \frac{P_{DCM}}{I_o^* V_i} = \frac{G_{CCM} V_i^2 \, 2 f_s C \gamma_{DCM}}{I_o^* V_i} \tag{6.108}$$

$$G_{DCM}(\gamma) = \frac{V_o^*}{V_i} = \frac{G_{CCM} \gamma_{DCM}}{\gamma} \tag{6.109}$$

Finally, using (6.110), the load characteristic in DCM is presented in Figure 6.12 for $\mu_1 = \mu_2 = 3$. The dots in the figure correspond to

simulation results using PSIM software, thus validating the theory through simulation.

$$G_{DCM}\left(D,\mu_1,\mu_2,\gamma\right) = G_{CCM}\frac{\gamma_{DCM}}{\gamma}, \text{ if } \gamma < \gamma_{DCM} \qquad (6.110)$$

Figure 6.12 – Load characteristic and boundary between DCM and CCM for $\mu_1 = \mu_2 = 3$
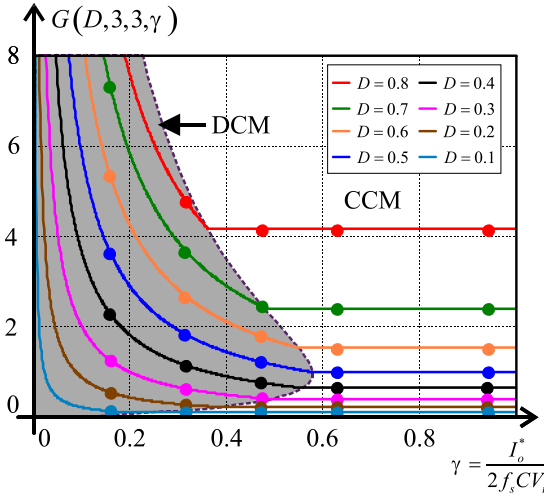
Source: Own elaboration.

Considering imposing input and output voltage sources, it is sufficient for the converter to operate in DCM when the condition (6.111) is satisfied.

$$D < \frac{G_{CCM} + \dfrac{G_{CCM}\pi}{\mu_2}\cot\left(\dfrac{\pi D}{\mu_2}\right) - 1}{\dfrac{G_{CCM}\pi}{\mu_2}\cot\left(\dfrac{\pi D}{\mu_2}\right) + \dfrac{\pi}{\mu_1}\cot\left(\dfrac{\pi(1-D)}{\mu_1}\right)} \qquad (6.111)$$

Considering resistive output load resistance, if it is assumed infinite coupling capacitance, the condition for meeting DCM is the same as those conventional PWM converters, presented in (6.112). For the proposed converter, it observed that this condition is necessary, but not sufficient, as the converter becomes in DCM with smaller D. However, this equation is a quick indication and approximation as for the mode of operation of the converter.

$$D < 1 - \sqrt{\frac{2L_{eq}f_s}{R_o^*}} \qquad (6.112)$$

Where:

- L_{eq} is the parallel equivalent inductance between the inductors.

6.4 Discontinuous Voltage Mode (DVM)

In 1997, Ćuk states in [58]: "*Duality relationship in switching converters can be extended to even include their discontinuous conduction mode*". The author used the duality principle applied for Discontinuous Inductor Current Mode (DICM) to explain the Discontinuous Capacitance Voltage Mode (DVCM) for 4th order converters. Symmetry properties are also included, as shown in [59], which proves that the DVM for Ćuk converter presents fairly good Power Factor Correction (PFC) characteristic, with the advantage of low current stress for heavy loads.

Differently, it is worth mentioning that in this thesis, no duality principle was implemented, and still the same fundamental equations and duality properties are found. The DVM operation can then be defined as the voltage discontinuity across the diode after subinterval Δt_1. And, as in DCM, in addition to the subintervals in CCM mode presented in section 6.2, there is another subinterval, but instead of "open" equivalent circuit, there is a "short" equivalent circuit. However, this interval occurs sequentially during subinterval Δt_2, while third subinterval is common to the second subinterval in CCM. Therefore, Δt_1 is no longer expressed as in (6.29), but rather by the interval for which the voltage across the diode is zeroed.

As in section 6.4.3, the objective remains finding the load characteristic and boundary condition between CCM and DVM. Therefore, the system of equations and its resolution is not necessary.

6.4.1 Second subinterval for DVM

The equivalent circuit of the second subinterval in DVM is shown in Figure 6.13. Due to the large voltage drop across the coupling capacitance, the diode becomes forward biased while the switch is still conducting.

Figure 6.13– Equivalent circuit of the second subinterval in DVM mode.
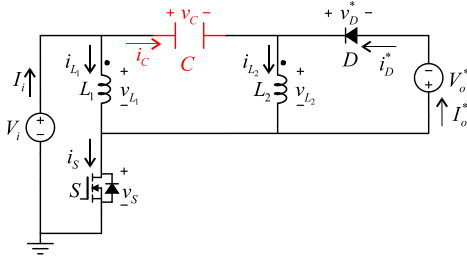
Source: Own elaboration.

6.4.2 Waveforms

The main general waveforms of the currents and voltages in the switching and reactive elements are shown in Figure 6.14 . Notice the dual behavior between DVM and DCM presented in section 6.3.2: there is a large voltage excursion across the switching elements, whereas less current ripple is observed. It worth mentioning that, in the same way that in DCM it is performed ZCS, in DVM it is performed ZVS.

Figure 6.14 – General main waveforms in DVM.
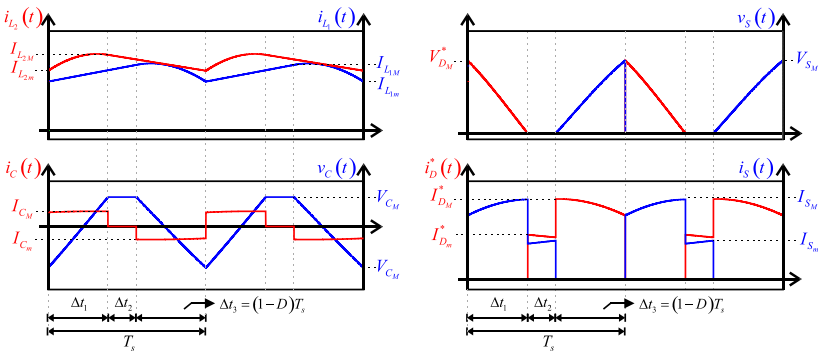
Source: Own elaboration.

6.4.3 Load characteristic and boundary condition in DVM

The boundary condition for the converter to reach DVM mode is presented in (6.113)

$$V_i + V_o^* - V_{C_M} = 0 \tag{6.113}$$

Substituting (6.34) and (6.55) in (6.113), the condition is then defined in dimensionless terms as (6.114).

$$1 + G_{CCM}(D, \mu_1, \mu_2) - \varepsilon_M(\gamma) = 0 \tag{6.114}$$

Knowing that, in this mode, the converter operates as CPL and is able to deliver a given maximum power and adopting the same procedure as in section 6.3.2.1, let the following equations:

$$P_{\max} = P_{DVM} = G_{CCM}V_i^2 2f_s C\gamma_{DVM} \tag{6.115}$$

$$\gamma_{DVM} = root\left(1 + G_{CCM}(D, \mu_1, \mu_2) - \varepsilon_M(\gamma)\right) \tag{6.116}$$

$$G_{DVM}(\gamma) = \frac{V_o^*}{V_i} = \frac{G_{CCM}\gamma_{DVM}}{\gamma} \tag{6.117}$$

Using (6.118), the load characteristic for $\mu_1 = \mu_2 = 3$ and DVM region is presented in Figure 6.15, in which the dots are values found in simulation results using PSIM software. Notice that the voltage gains decreas tending to zero as the parametrized output current increases.

$$G_{DVM}(D, \mu_1, \mu_2, \gamma) = G_{CCM}\frac{\gamma_{DVM}}{\gamma}, \text{ if } \gamma > \gamma_{DVM} \tag{6.118}$$

Figure 6.15 – Load characteristic and boundary between DVM and CCM for $\mu_1 = \mu_2 = 3$.
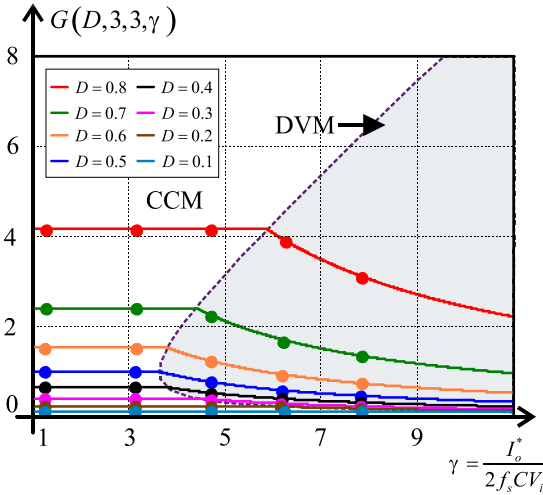
Source: Own elaboration.

Considering imposing input and output voltage sources, it is sufficient for the converter to operate in DVM when the condition (6.119) is satisfied.

$$D > \frac{G_{CCM} + \dfrac{G_{CCM}\pi}{\mu_2}\cot\left(\dfrac{\pi D}{\mu_2}\right) - 1}{\dfrac{G_{CCM}\pi}{\mu_2}\cot\left(\dfrac{\pi D}{\mu_2}\right) + \dfrac{\pi}{\mu_1}\cot\left(\dfrac{\pi(1-D)}{\mu_1}\right)} \tag{6.119}$$

Let, the condition for DVM:

$$1 + G_{CCM} - \varepsilon_M < 0 \tag{6.120}$$

Substituting (6.47) in (6.120) results in:

$$G_{CCM}\left(1 + \frac{\pi(1-D)}{\mu_2}\cot\left(\frac{\pi D}{\mu_2}\right) - \frac{1}{2f_s C R_o^*\left(1 + \dfrac{\pi(1-D)}{\mu_2}\cot\left(\dfrac{\pi D}{\mu_2}\right)\right)}\right) < 0 \tag{6.121}$$

As G_{CCM} is positive, and considering the assumption that $\mu_1 = \mu_2 \to \infty$, which means applying the limit definition presented in (6.67) in (6.121), results in (6.122). Finally, developing it, the condition for operating in DVM is presented in (6.123), which is also confirmed in [56] found through duality principle. Again, such condition is necessary, but not sufficient for finite values of μ_1 or μ_2 , but is a quick indication as for the mode the converter is operating.

$$\frac{2f_s CR_o^*(1-D) - D^2 + 2f_s CR_o^* D}{2f_s CR_o^*} < 0 \qquad (6.122)$$

$$D > \sqrt{2f_s CR_o^*} \qquad (6.123)$$

6.5 Discontinuous Quasi-Resonant Mode (DQRM)

In addition to CCM, DCM and DVM, another operating mode is identified. It can be considered as a combination between DCM and DVM regions, therefore a restricted portion of the parametrized output current plane [56]. In DQRM, the transistor is turned ON at zero current (ZCS) and OFF at zero voltage (ZVS). Therefore, the switching loss in the semiconductors are reduced in the same way as in other quasi-resonant converters.

Indeed, according to [60], this operating region can also be considered as members of quasi-resonant classes. In contrast with other quasi-resonant converters, which require frequency control, the DQRM region can be controlled through the duty cycle and there is no need for bidirectionality for the switch.

This section aims to briefly describe the DQRM using the same technique as in previous sections to evaluate the parameters that bring the converter in this mode. Therefore, equations and further details are not presented.

6.5.1 Waveforms

The general waveforms of the currents and voltages in the switching and reactive elements and their maximum and minimum initial conditions for two switching periods are shown in Figure 6.16.

Figure 6.16 – General main waveforms in DQRM.
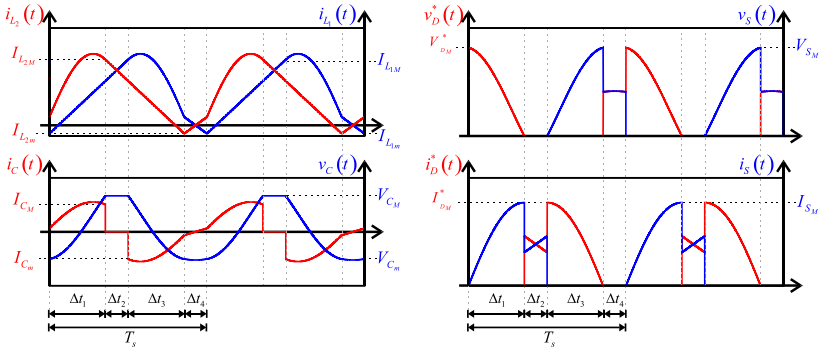
Source: Own elaboration.

6.5.2 Boundary condition between CCM and DQRM

Using the same analysis to plot the boundaries as in previous sections, it is possible to note that the DQRM is an overlapping between DCM and DVM. In the region corresponding to this overlapping, the converter can no longer be characterized as in (6.110) or (6.118), as the existence of CCM region is not satisfied. However, it is possible to identify all regions of operation in the same parametrized output current plane, as shown in Figure 6.17. Notice that, at low values of μ_1 and μ_2, the DCM and DVM curves have the tendency of overlapping, that is, under such conditions the converter is entering the DQRM region.

A singular and interesting operating point, however, can be characterized for $\mu_1 = \mu_2 = 1.548$. It is a critical mode between DQRM, DVM, DCM and CCM regions, as shown in Figure 6.17 (curve in orange). It is worth presenting the general main waveform in the critical DQRM-CCM condition for $D = 0.5$, $\mu_1 = \mu_2 = 1.548$ and $\gamma = 2.659$, as shown in Figure 6.18.

Figure 6.17 – Identified all operating regions in the same parametrized output current.
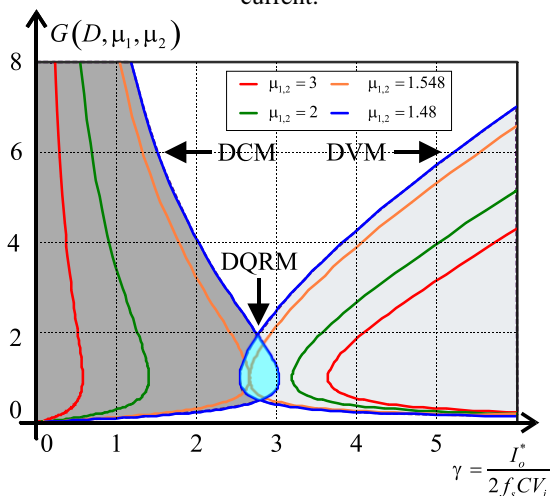
Source: Own elaboration.

Figure 6.18 – General main waveforms in critical DCM-DVM-CCM-DQRM ($\mu_1 = \mu_2 = 1.548$ and $D = 0.5$).
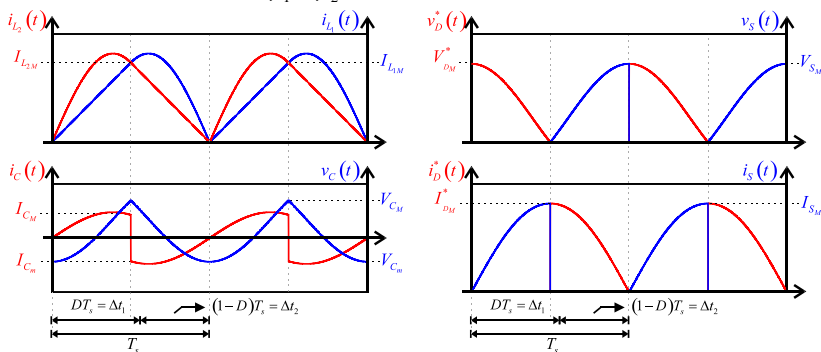
Source: Own elaboration.

6.6 Power transfer capability

In this section, $P_{\max}$ (W) and $P_{\min}$ (W) equations are expressed as a function of input and output voltages, reactive elements and switching

frequency. These expressions are derived, supposing $\mu_1 = \mu_2 \to \infty$ for simplification purposes.

6.6.1 Maximum power

Expressing the output load resistance R_o^* in terms of output power and output voltage V_o^*, substituting (6.74) in (6.123) results in an expression for determining maximum delivered power. This equation shows the importance of operating at high frequencies and coupling capacitances, and mainly high voltages, as maximum power is in proportion to the squared input and output voltages.

$$P_{max} \leq 2Cf_s \left(V_o^* + V_i\right)^2 = 2Cf_s \left(nV_o + V_i\right)^2 \qquad (6.124)$$

It also validates the choice for using a step-down coupled inductor in L_2 instead of a step-down coupled inductor in L_1, as it would decrease the reflected capacitance, which is in squared proportion. Therefore, placing a step-down coupled inductor in L_1, would result in maximum theorical power defined by (6.125).

$$P_{max}^{new} = \frac{P_{max}}{n^2} \qquad (6.125)$$

Therefore, the step-down coupled inductor in the secondary increases power transfer capability and a step-up coupled inductor in the primary circuit is suggested for the same sake, which resembles [61].

6.6.2 Minimum power

As in a conventional Flyback converter, the converter is able to deliver a minimum power. Following the same steps as in section 6.6.1 for Equation (6.112), results in:

$$P_{min} \geq \left(\frac{V_i V_o^*}{V_i + V_o^*}\right)^2 \frac{1}{2L_{eq}f_s} \qquad (6.126)$$

6.7 Final considerations

An accurate study of the modified Flyback converter applied in CPT was presented. The found static gain that do not neglect neither voltage or current ripple along with load characteristic was important to precisely limit not so common regions of operation and significant fundamental discussions may arise.

Equating the initial conditions of the system as a function of external and controllable variables was important to express and understand the converter without the need of iteration process or simulation results. Moreover, parametrizing the system with respect to the parametrized output current presented in this Chapter, decreased the number of variables by grouping them, turned the analysis dimensionless and independent of a load resistance.

The strategy of using CPL theory for DCM and DVM and their boundary conditions was responsible for easily expressing their load characteristic, numerically, without the need of equating their topological states. The understanding of DCM, DVM and DQRM is fundamentally important, mainly in a CPT system, where low coupling capacitance causes high voltage excursion as well as high resonance frequency comparable with switching frequencies. Plus, heavy or light load, that is, maximum or minimum delivered power phenomenon can be observed through the proposed analysis, and also applied in classical converters.

Although no duality theory was implemented, many dual occasions were observed between DCM and DVM. Indeed, such study is valid or may easily be adapted to any 4th order PWM converter. As demonstrated, the DCM region is to ZCS, as DVM region is to ZVS. Plus, the CCM is region is to hard switching, as DQRM is to ZCS and ZVS. Future studies are still required to understand the consequences of operating in DVM and DQRM regions applied in CPT and comparison with studies in [56] are still required.

Besides, placing a step-up coupled inductor in the secondary stage was beneficial in terms of adjusting voltage gain levels for practical implementation and power transfer capability. As it will be seen following Chapter 7, the values of the inductances also require criteria other than maximum ripple, commonly presented in the literature, in order to increase efficiency of the converter.

7 PROJECT AND SIZING

This chapter presents the sizing and design criteria of the proposed converter. The development of the project has the purpose of verifying the equations provided in Chapter 6 through simulation and further experimental results. The complete schematic is presented in Figure 7.1.

The designed PCBs in 3D, shown in Figure 7.2, accurately presents the primary and secondary stages prototype's dimension including gate driver, bridge rectifier and clamping circuitry.

Figure 7.1 – Complete and idealized proposed CPT system.
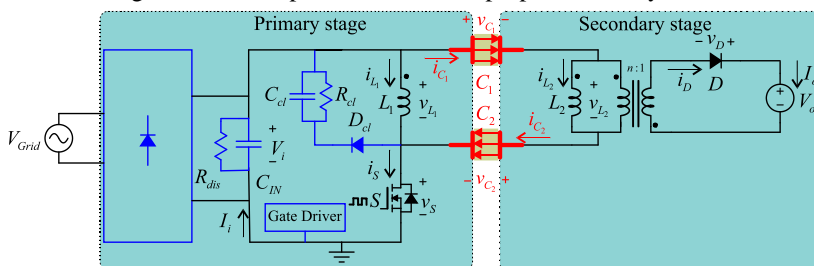
Source: Own elaboration.

Figure 7.2 – The designed PCBs in 3D.
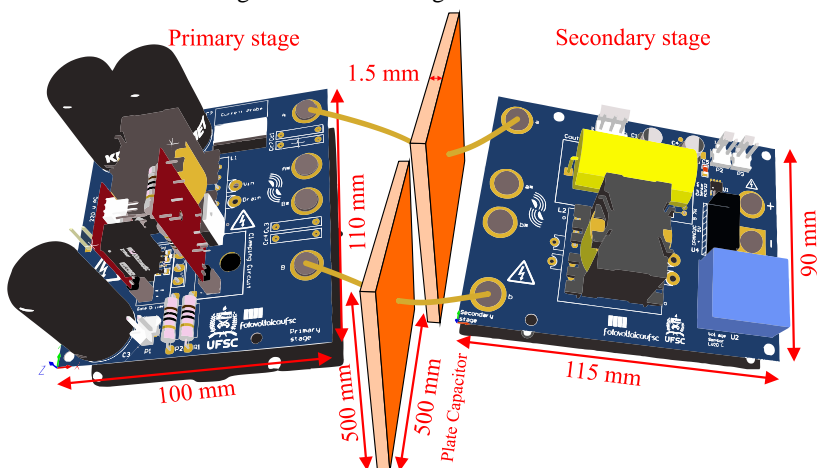
Source: Own elaboration.

7.1 Design specification

Although the commercial Twizy charger is a 2000 W, the proposed converter was constrained to deliver 200 W. The reason for limiting power is that a conventional Flyback is more cost-effective for relatively low power applications (in DCM, it is commercially available for up to 150 W [62], [63]). Nevertheless, interleaving solution for the modified Flyback can be further applied to reach higher power.

Input battery voltage goes along with Twizy's battery specification, whereas maximum and minimum input DC voltage of the converter are specified according to a regular bridge rectifier connected to the grid. The bridge rectifier, clamping circuit and gate driver were designed and implemented as part of the prototype and are presented, respectively in Appendixes F, D and H.

The switching frequency (300 kHz) and coupling capacitance (about 10 nF) were selected based on approximated values found in [34]. As the converter is hard switched, frequency is also limited by excessive switching loss. It is important notice that the selected frequency is lower than the resonance frequency found experimentally in the reactive elements (capacitors and inductors). The turns ratio n of the coupled inductor was chosen so that the converter operates close to $D = 0.5$ for the sake of efficiency and good performance.

Table VI – Design specification.

Specification	Value
Rated power	200 W
Nominal battery voltage	54 V
Maximum battery voltage	59.8 V
Minimum battery voltage	49.25 V
Maximum output current	3.34 A
Nominal input voltage	295.57 V
Maximum input voltage	311.13 V
Minimum input voltage	280 V
Grid voltage	220 V RMS
Grid frequency	60 Hz

7.2 Load characteristic specification

The first step is to choose adequately the parameters μ_1 and μ_2. The choice is based on the following criteria:

- 1) They are large enough to keep output parameterized current γ in the CCM region as small gain variations are expected. From Table VI and applying (6.53), it is possible to define maximum, nominal and minimum values for γ. These values are shown in Figure 7.3 and are contained in CCM region.
- 2) Consider the power loss associated with leakage inductance of the coupled inductor. Therefore, μ_2 should be kept relatively low, as leakage inductance is in proportion to magnetizing inductance.
- 3) The parameter μ_1 should be larger than μ_2 to compensate and increase equivalent inductance. It also decreases current ripple through the circuit, which increases efficiency.

Following it, the parameters $\mu_1 = 8$ and $\mu_2 = 3$ were chosen. Table VII presents the load characteristic specification, whereas Figure 7.3 present the load characteristic plotting for the adopted parameters. Note that the converter is expected to operate in the hatched area, far from DCM region and even farther from DVM region. Using equations (6.107) and (6.115) it is also possible to check the theorical power range limits of the converter.

Table VII – Load characteristic specification.

Specification	Value
μ_1	8
μ_2	3
D_{min}	0.477
D_o	0.512
D_{max}	0.550
γ_{min}	0.597
γ_o	0.628

γ_{max}	0.663
f_s	300 kHz
$C_1 = C_2$	10 nF
n	6
P_{min}	97.788 W
P_{max}	1.149 kW

Figure 7.3 – Load characteristic for the designed parameters.
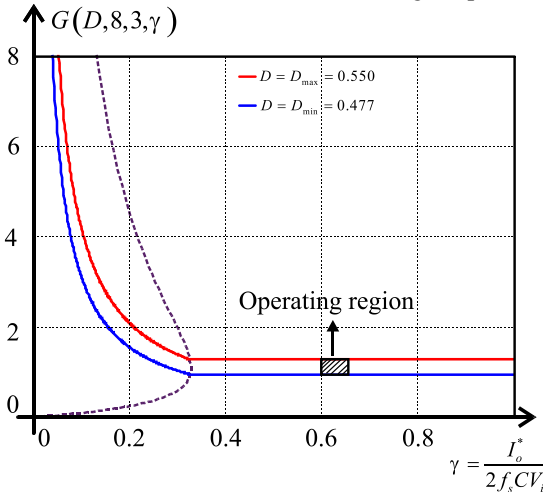
Source: Own elaboration.

7.3 Component sizing

In this section, the equations presented in Chapter 6 are applied to size the components. Afterwards, the components are either handmade manufactured or commercially acquired.

7.3.1 Coupled inductor L_2

Instead of the commonly ripple current technique, the coupled inductor L_2 is calculated as a function of the load characteristic specification shown in section 7.2 according to (7.1).

$$L_2 = \frac{\mu_2^{\,2}}{\omega_2^{\,2}C} = 506.6\ \mu\mathrm{H} \tag{7.1}$$

The coupled inductor design needs an initial estimate of the core size to meet the requirements efficiently and cost-effective. The used method is based on the Core Area Product, obtained by multiplying the core magnetic cross-section area A_e by the window area (bobbin area) A_w available for the winding, as presented in Figure 7.4.

Figure 7.4 – EE Core representation.
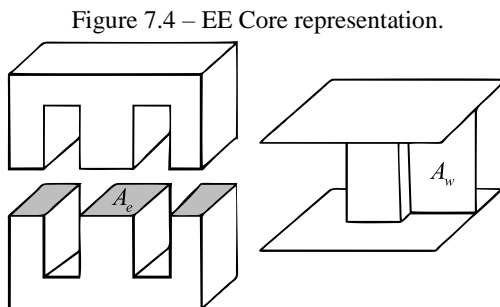
Source: Adapted from [62].

7.3.1.1 Magnetic cross-section area A_e

It follows from Faraday's Law:

$$E = N\frac{d\phi}{dt} = \frac{NA_e \Delta B_{max}}{dt} \tag{7.2}$$

Where:
- E is the voltage applied in the coupled inductor (V);
- N is the number of turns;
- A_e is the magnetic cross-section area (cm^2);
- ΔB_{max} is the peak flux density swing (T);

Equation (7.2) is applied and developed for the secondary of the coupled inductor, since a known and constant voltage is applied during the second subinterval. The largest cross-section area occurs for maximum gain scenario, as presented in (7.3).

$$A_e = \frac{V_{o\max}\left(1-D_{\max}\right)}{f_s N_s \Delta B_{\max}} \tag{7.3}$$

7.3.1.2 Window area A_w

Let the definition of current density:

$$NI_{RMS} = A_s J_{\max} = K_w K_{u2} A_w J_{\max} \tag{7.4}$$

Where:

- I_{RMS} is the RMS current applied in the winding (A);
- A_s is the effective winding copper area;
- $J_{\max}$ is the maximum allowed current density;

Two factors must be applied in the window area to relate it to the effective winding cupper area. One factor that accounts for non-idealities, such as creepage, insulation and voids between round wires. A safe factor is $K_w = 0.4$. The other factor will be defined as a calculated secondary use factor K_{u2}, presented in (7.5).

$$K_{u2} = \frac{1}{1+\dfrac{1}{n}\dfrac{I_{L_{2p_{RMS}}}}{I_{L_{2s_{RMS}}}}} \tag{7.5}$$

Rearranging (7.4), results in the window area equation, presented in (7.6), which also is the largest for $D_{\max}$.

$$A_w = \frac{N_s I_{L_{2s_{RMS}}}}{K_w K_{u2} J_{\max}} \tag{7.6}$$

7.3.1.3 Ferrite core

The area product equation and its result are shown in (7.7). The ferrite core available in the laboratory is a NEE-30/15/14 [64]. The parameters used to calculate the area product are shown in Table VIII. Their values and meanings are explained in the following sections.

$$A_e A_w = \frac{V_o(1-D)I_{L_{2S_{RMS}}}}{K_w K_{u2} J_{max} f_s \Delta B_{max}} = 0.459 \text{ cm}^4 \tag{7.7}$$

Table VIII – Ferrite core specification for coupled inductor L_2 .

IP12E Ferrite from Thornton and chose parameters	
Specification	Value
Volume	8.174 cm^3
Weight	21 g
A_e	3.235 cm^2
A_w	0.507 cm^2
$A_e A_w$	1.037 cm^4
K_w	0.4
K_{u2}	0.555
J_{max}	465 A/ cm^2
ΔB_{max}	0.1 T

7.3.1.4 Peak flux density swing

Core hysteresis losses are a function of flux swing and frequency. The flux swing can be limited by loss or saturation. For operating frequencies above 250 kHz [65], core loss is the determining factor. Based on the curve provided by the datasheet of the material shown in Figure 7.5, the initial peak flux density was set to 0.05 T, corresponding to a core loss of approximately 30 mW/g (in green). The peak flux density in the curve must be doubled to obtain ΔB_{max} , as usually in datasheets such curve is obtained from sinusoidal waveforms.

Figure 7.5 – IP12 EE Core loss curve indicating powe loss for 0.05T at 300kHz.
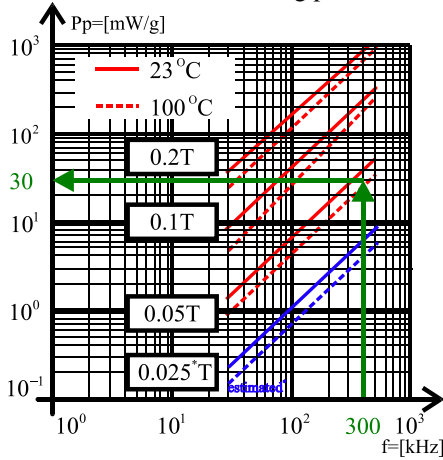
Source: Adapted from [64].

7.3.1.5 Current density

The conductors are calculated according to maximum current density and skin effect. To meet current density requirement, the copper area should be larger than the value presented in (7.8). The value of J_{max} was iteratively set to 465 A/cm^2.

$$S_P = \frac{I_{L_{2PRMS}}^2}{J_{max}} = 0.00149 \text{ cm}^2$$

$$S_S = \frac{I_{L_{2SRMS}}^2}{J_{max}} = 0.01114 \text{ cm}^2$$

(7.8)

To avoid skin effect, the diameter must be less than the value presented in (7.9). The selected AWG 30 diameter value is 0.025 cm, the cupper area S_{cu} is 0.000509 cm^2 and the insulated area S_{AWG} is 0.000704 cm^2.

$$\frac{15}{\sqrt{f_s}} = 0.027 \text{ cm}$$

(7.9)

Number of conductors in parallel are simply defined by (7.8) divided by AWG cupper area, as presented in (7.10).

$$N_{C_P} = \frac{S_P}{0.000509} = 3$$
$$N_{C_S} = \frac{S_S}{0.000509} = 22$$

(7.10)

7.3.1.6 Number and of turns and winding configuration

A technique to reduce leakage inductance known as interleaving was used. It divides the windings into smaller sections to decrease inner magnetic field. In

Figure 7.6, it is presented the used interleaving structure with $K_i = 2$. According to [66], the leakage inductance increases in direct squared proportion to the number of turns over the factor K_i, as presented in (7.11). Therefore, the number of turns should be kept as low as possible, while interleaving with $K_i = 2$ reduces leakage inductance by 4 times, compared to no interleaving structures.

$$l_k \propto \frac{N^2}{K_i^2}$$

(7.11)

Figure 7.6 – Coupled inductor with interleaving technique with $K_i = 2$.
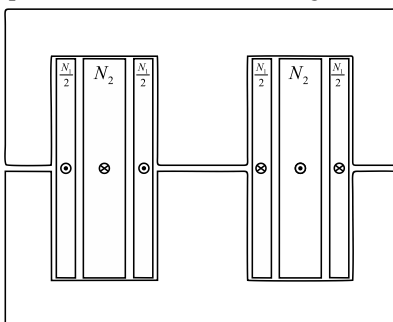
Source: Own elaboration.

The number of turns of the secondary is defined straight from (7.3), as presented in (7.12). Instead of rounding up, the number of turns is rounded down in order to decrease leakage inductance as well as to

facilitate manufacturing. Afterwards, the number of turns in the primary is shown in (7.13). It is important to notice that the magnetic field ΔB_{max} increases with less given turns, and therefore compromises core losses, although it improves winding efficiency.

$$N_s = \frac{V_{o\max}\left(1-D_{\max}\right)}{A_e f_s \Delta B_{\max}} = 7 \tag{7.12}$$

$$N_p = nN_s = 42 \tag{7.13}$$

After determining the number of turns, the new magnetic flux is recalculated as presented in (7.14) and core loss should be observed again.

$$\Delta B_{\max_{New}} == \frac{V_{o\max}\left(1-D_{\max}\right)}{A_e f_s N_s} = 0.111 \text{ T} \tag{7.14}$$

7.3.1.7 Airgap

The addition of air gap introduces a much greater reluctance than the core reluctance, making the value of the magnetizing inductance virtually insensitive to variations of the core permeability. Therefore, saturation occurs at higher values of current, more energy can be stored and the inductor becomes less susceptible to variations in the magnetic properties of the core. The total air gap, neglecting the large core permeability compared to air permeability, is given in (7.15), whereas the gap of each leg of the core is given in (7.16). In practice, these values were finely adjusted to return desirable inductances.

$$l_t = \frac{\mu_o A_e N_p^2}{L_2} = 0.534 \text{ mm} \tag{7.15}$$

$$l_g = \frac{\mu_o A_e N_p^2}{4L_2} = 0.133 \text{ mm} \tag{7.16}$$

7.3.1.8 Fulfillment performance

To check whether the coupled inductor is performable or not, a factor k is calculated as presented in (7.17). This factor must necessarily

be less than 1 and it is advisable to be larger than 0.3. If it is not possible to construct the winding in the available window area, one must adjust the parameters $\Delta B_{\max}$, $J_{\max}$ or change the ferrite core in an iterative process.

$$0.3 < k = \frac{S_{AWG}N_{C_P}N_P + S_{AWG}N_{C_s}N_S}{A_w K_w} = 0.58 < 1 \qquad (7.17)$$

7.3.1.9 Coupled inductor's main parameters

To find the main parameters of the coupled inductor, it was performed open and short circuit tests. The inductance and equivalent series resistance found in the short circuit test corresponds to the leakage inductance and ESR, whereas the inductance found in the open circuit test corresponds to the sum values between leakage and magnetizing inductances. The tests were performed using E4990A-020 impedance analyzer. The result is shown in Table IX. The turns ratio found was 6.13.

Table IX – Coupled inductor's pratical main paramaters.

Magnetizing (μH)		Leakage (μH)		ESR (Ω)		Resonance (Mhz)	
Pri.	Sec.	Pri.	Sec.	Pri.	Sec.	Pri.	Sec.
579.16	14.88	7.43	0.192	1.66	0.04	1.75	1.58

7.3.2 Inductor L_1

As in section 7.3.1, the inductor L_1 is calculated as a function of the load characteristic specification shown in section 7.2 according to (7.18). The largest current ripple is found when maximum input and output voltages are applied. Equation (6.82) is then applied for this scenario, as presented in (7.19).

$$L_1 = \frac{\mu_1^2}{\omega_1^2 C} = 3.6 \text{ mH} \qquad (7.18)$$

$$\Delta I_{L_1} = \frac{V_i D}{L_1 f_s} = 151.03 \text{ mA} \qquad (7.19)$$

7.3.2.1 Ferrite core

Following the same procedure as in section 7.3.1.3, but considering the input voltage during first subinterval, the largest product area equation and its result are shown in (7.20). The largest value is found when minimum input voltage and maximum input voltage is applied. The ferrite core was the same of the coupled inductor due to availability.

$$A_e A_w = \frac{V_{i\min} D_{\max} I_{L_{1RMS}}}{K_w J_{\max} f_s \Delta B_{\max}} = 0.223 \text{ cm}^4 \tag{7.20}$$

Table X– Ferrite core specification for coupled inductor L_2.

IP12E Ferrite from Thornton and chosen parameters	
Specification	Value
Volume	8.174 cm^3
Weight	21 g
A_e	3.235 cm^2
A_w	0.507 cm^2
$A_e A_w$	1.037 cm^4
K_w	0.7
$J_{\max}$	470 A/ cm^2
$\Delta B_{\max}$	0.05 T

7.3.2.2 Peak flux density swing

Based on the curve provided by the data sheet of the material, shown in Figure 7.7, the initial peak-to-peak flux density was set to 0.025 T, corresponding to a core loss of approximately 5 mW/g. Indeed, very low magnetic loss is expected, whereas large cupper loss is foreseen. Again, the peak flux density in the curve must double to obtain $\Delta B_{\max}$.

Figure 7.7 – IP12 EE Core loss curve indicating powe loss for 0.025T at 300kHz.
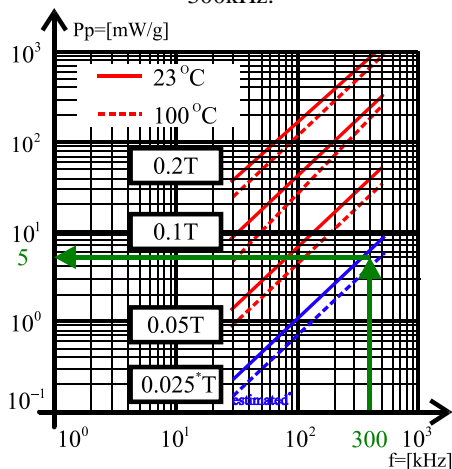
Source: Adapted from [64].

7.3.2.3 Current density

To meet current density requirement, the copper area should be larger than the value presented in (7.8). The value of J_{max} was set to 470 A/cm^2. In order to avoid skin effect, the same AWG 30 type was selected, and therefore, number of conductors in parallel is presented as in (7.22).

$$S_1 = \frac{I_{L_{1RMS}}^2}{J_{max}} = 0.00152 \text{ cm}^2 \tag{7.21}$$

$$N_{C_1} = \frac{S_1}{0.000509} = 3 \tag{7.22}$$

7.3.2.4 Number of turns and their configuration

The number of turns is presented in (7.23). This value is rounded down. The 3 conductors were handmade twisted as in a Litz wire.

$$N_1 = \frac{V_{i\min} D_{max}}{A_e f_s \Delta B_{max}} = 85 \tag{7.23}$$

7.3.2.5 Airgap

The total air gap, neglecting the large core permeability compared to air permeability, is given in (7.24), whereas the gap of each leg of the core is given in (7.25).

$$l_t = \frac{\mu_o A_e N_1^2}{L_1} = 0.0307 \text{ mm} \tag{7.24}$$

$$l_g = \frac{\mu_o A_e N_p^2}{4L_2} = 0.077 \text{ mm} \tag{7.25}$$

7.3.2.6 Fulfillment performance

As in section 7.3.1.8 , the inductor fulfillment performance is checked as presented in (7.26).

$$0.3 < k = \frac{S_{AWG} N_{C_1} N_1}{A_w K_w} = 0.302 < 1 \tag{7.26}$$

7.3.2.7 Inductor's main parameters

The values of the inductor's parameters are shown in Table XI.

Table XI – Inductor's practical main paramaters.

Self-inductance (mH)	ESR (Ω)	Resonance (kHz)
3.35	41.95	803.9

7.3.3 Diode

The diode is specified according to maximum average and RMS values of the current and reverse voltage. The average and RMS values and equations, considering $D = D_{max}$, are presented in (7.27) and (7.28), respectively. Maximum reverse voltage condition occurs when maximum input and output voltages are applied, as presented in (7.29). Therefore, a Schottky diode IDH20G65C6XKSA1 from Infineon Technologies was used. Its mains specification is shown in Table XII.

$$I_{D_{avg}} = I_o = 3.344 \text{ A} \tag{7.27}$$

$$I_{D_{RMS}} = I_{L_{2S_{RMS}}} = 5.179 \text{ A} \tag{7.28}$$

$$V_{D_{\max}} = \frac{V_{i_{\max}} - V_{C_m}}{n} + V_{o_{\max}} = 121.11 \text{ V} \tag{7.29}$$

Table XII – Diodes's main paramaters.

IDH20G65C6XKSA1	
Specification	Value
Reverse voltage (V_{RRM})	650 V
Forward current (I_F)	20 A
Forward voltage (V_F)	1.25 V

7.3.4 Active switch

The active switch is specified according to the maximum average and RMS values of the current and maximum reverse voltage. The average and RMS values, considering $D = D_{\max}$, are presented in (7.30) and (7.31), respectively. Maximum reverse voltage condition is given in (7.32).

$$I_{S_{avg}} = I_o^* G_{CCM} = 119 \text{ mA} \tag{7.30}$$

$$I_{S_{RMS}} = 0.998 \text{ A} \tag{7.31}$$

$$V_{S_{\max}} = n V_{D_{\max}} = 726.65 \text{ V} \tag{7.32}$$

An active switch with fast commutation is mandatory to reach good efficiency. Therefore, a Sic MOSFET C2M0280120D from Cree/Wolfspeed was chosen. Its main parameters are shown in Table XIII.

Table XIII – MOSFET's main paramaters.

C2M0280120D	
Specification	Value
Drain-to-source Voltage (V_{DSmax})	1200 V
Gate-to-source Voltage (V_{GSmax})	-10/25 V
Drain current (I_D) @ 100 ºC	6 A
Drain-to-source resistance R_{DSon}	280 m Ω
Input capacitance C_{iss}	259 pF
Output capacitance C_{oss}	23 pF
Reverse transfer capacitance C_{rss}	3 pF
t_r rise time	7.6 ns
t_f fall time	9.9 ns
Internal gate resistance $R_{G(int)}$	11.4 Ω
Gate charge total Q_g	20.4 nC

7.3.5 Coupling capacitor

7.3.5.1 Film capacitor

Before testing the converter with real metal plates, it was performed a test using film capacitors meant for high-frequency AC and pulse circuits. The coupling capacitors must meet the maximum allowed AC voltage and RMS current. The RMS value voltage across the coupling capacitors were calculated and their result is shown in (7.33). For quicker check, it is also sufficing to check if maximum peak voltage value calculated across the coupling capacitors are lesser than the RMS specified by the datasheet of the capacitor. The RMS current value in the coupling capacitors is presented again in (7.34). Table XIV presents the main specification of the used film capacitor B32672L8103J000.

$$V_{C_{1RMS}} = V_{C_{2RMS}} = 32.69 \text{ V} < \frac{V_{C_M}}{2} \tag{7.33}$$

$$I_{C_{RMS}} = 0.998 \text{ A} \tag{7.34}$$

Table XIV – Coupling film capacitor's specifiations.

B32672L8103J000	
Specification	Value
Capacitance	10 nF
Tolerance	5 %
tan δ @ 100 kHz	2×10^{-3}
V_{RMS}@ 300 kHz	~150 V
I_{RMS}@ 300 kHz	~3 A

7.3.5.2 Metal plate capacitor

Metal plates are selected as already presented in Section 4.7, and it is presented in Table XV. The material, fiberglass, is named FR-4 (glass reinforced epoxy laminate material. The dielectric strength d_{st} of the fiberglass is about 50 kV/mm, therefore, a minimum distance must be respected to avoid voltage breakdown, as shown in (7.35). In the same way, keeping the distance = 1.5 mm, a maximum voltage is allowed in the plate capacitors is shown in (7.36). Notice that, using practical values of the inductances and the values of the metal plate capacitors the relative frequency parameters resulted in $(\mu_1, \mu_2) = (6.5, 2.7)$.

Table XV – Coupling metal plate capacitor's main specifications.

Metal Plates	
Specification	Value
Capacitance	7.1 nF
Length	500 mm
Width	500 mm
Distance d	1.5 mm
Dielectric material	Fiberglass
Dielectric constant ε_r	4.8

Dielectric Strength d_{st}	50 kV/mm
ESR @ 300 kHz	1 Ω

$$d_{\min} = \frac{V_{C_{\max}}}{d_{st}} = 0.0012 \text{ mm}$$ (7.35)

$$V_{C_{\max}} = d \times d_{st} = 75 \text{ kV}$$ (7.36)

7.3.6 Output capacitor

Maximum voltage ripple of the output capacitor was designed for 1% of the output voltage. From equation (6.79), it is possible to size the output capacitor as presented in (7.37). It was observed that maximum ripple voltage occurs for minimum output and input voltages, corresponding to $D = 0.503$. The output capacitor must also follow the ESR criteria. Following the procedure in [62], the least ESR allowed is presented in (7.38). Finally, the last criteria is the RMS current value already mentioned in (6.95), which is expressed again together with its result for highest value condition $(D_{\max})$, presented in (7.39). Therefore, it was used the film capacitor C4GADUD5150AA1J from KEMET, with main specifications presented in Table XVI.

$$C_o = \frac{I_o D}{f_s \Delta V_{C_o (\%)} V_{o\min}} = 12.6 \; \mu\text{F}$$ (7.37)

$$ESR < \frac{\Delta V_{C_o (\%)} V_{o\min}}{I_{D_{pk-pk}}} = \frac{\Delta V_{C_o (\%)} V_{o\min}}{n\left(\dfrac{V_{o\min}^* \left(1 - D_{\min}\right)}{L_2 f_s} + \dfrac{V_{i\max}^* D_{\min}}{L_1 f_s}\right)}$$

$$\simeq \frac{\Delta V_{C_o (\%)} f_s L_{eq}}{n^2 \left(1 - D_{\min}\right)} = 70.83 \text{ m}\Omega$$ (7.38)

$$I_{C_{o\,RMS}} = \sqrt{I_{D_{RMS}}^2 - I_o^2} = 4.645 \text{ A}$$ (7.39)

Table XVI – Output capacitor's main specifications.

C4GADUD5150AA1J	
Specification	Value
Capacitance	15 µF
Tolerance	5%
AC Voltage	160 V
DC Voltage	250 V
Ripple Current @ 100 kHz	12 A
Dielectric Material	PP, Metallized
ESR @ 100 kHz	3.9 mΩ

7.3.7 Full bridge rectifier

The full bridge rectifier is specified for grid connection of 220 RMS and 60 Hz. The components are presented in Table XVII. The complete design is presented in Appendix H – .

Table XVII – Prototyped full bridge rectifier's components.

Component	Type	Main Parameters
Diode bridge	Standard	600 V / 1.1 V / 15 A
Input Capacitor C_{IN}	Electrolytic	3-p x 330 µH /350 V/1.97 A
Discharge resistor	Through hole	330 k Ω

7.3.8 Gate driver

The gate driver, presented in Figure 7.8, is an attachable device designed to switch at least 300 kHz for SiC MOSFETs, with components shown in Table XVIII. The complete design is presented in Appendix H.

Figure 7.8 – Gate driver PCB in 3D.
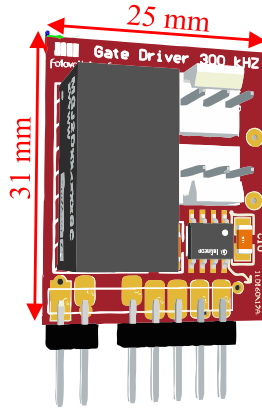
Source: Own elaboration.

Table XVIII – Prototyped gate driver's components.

Component	Type	Main Parameters
DC-DC Converter	Isolated	20 V / -15 V / 2 W
IC Gate Driver	Magnetic	1200 V /±6 A / 4 MHz
Bypass Cap.	SMD Ceramic	1 μF
R_{Gtotal}	Intrinsic	13 Ω

7.3.9 Passive clamping circuit

The passive clamping circuit, presented in Figure 7.9, with components shown in Table XIX, is also an attachable device designed to clamp voltage up to 1000 V. The leakage inductance L_{leak} of L_2 is submitted by the sum of the voltages V_i and V_o^*, but, differently from an ordinary passive clamping circuit applied in a conventional Flyback, the total voltage is also subtracted by the value V_{C_M}, as shown in (7.40). If the converter comes closer to DVM or DQRM, the total applied voltage across the magnetizing inductance during commutation tends to zero, which makes the energy associated with leakage inductance to decrease, and becomes independent of input, output or clamping voltage, but only dependent and limited by (7.41). Consequently, these features under such circumstances indicates that the modified Flyback has a large advantage

over the conventional Flyback with respect to efficiency. The complete design is presented in Appendix D.

Figure 7.9– Prototyped passive clamping circuit.
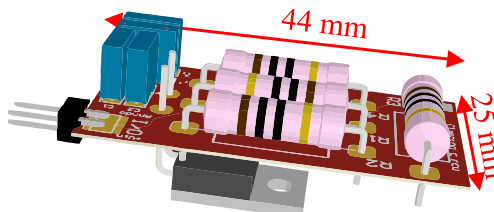
Source: Own elaboration.

$$P_{cl} = P_{g\infty} \frac{1}{1 - \left(\dfrac{V_i + V_o^* - V_{C_M}}{V_{cl}} \right)} = 7.67 \text{ W} \tag{7.40}$$

$$P_{g\infty} = 0.5 L_{leak} \left(I_{L_{1M}} + I_{L_{2M}} \right)^2 f_s = 3.75 \text{ W} \tag{7.41}$$

Where:

- L_{leak} is the leakage inductance of L_2 (H);
- P_{cl} is the power loss associated with the passive clamping circuit (W);
- V_{cl} voltage for which the circuit protects the switch (V).

Table XIX – Prototyped clamping circuit's components.

Component	Type	Main Parameters
Clamping diode	SiC Schottky	1200 V / 1.8 V / 1 A
Clamping capacitor	Film PET	2s x 1 nF / 630 V
Clamping resistor	Through Hole	(3s x 18 + 1x 12) k Ω → 11W

7.4 Open loop simulation results

The converter designed in this Chapter 7 is simulated using PSIM software in order to validate the theory proposed in Chapter 6. The simulated conditions are presented in Table XX and were chosen according to the output practical experimental testing setup. It is important to notice that, practical relative frequency parameters μ_1 and μ_2 changed from 8 and 3, to 7.72 and 3.21 respectively when using the film capacitors of 10 nF and to 6.5 and 2.1 using the metal plates.

To obtain an idea of the open-loop dynamics presented in the main waveforms of the converter, it is presented the output voltage, coupling capacitance voltage and current in Figure 7.11 Figure 7.12, respectively. The complete results are shown in Table XXI.

Table XX – Open-loop simulation's specifications.

Specification	Value
Rated power (P)	200 W
Output voltage (V_o)	57.75 V
Input voltage (V_i)	305.5 V
Resistive load (R_o)	16.675 Ω
Coupling capacitance (C_1)	10 nF
Coupling capacitance (C_2)	10 nF
Switching frequency (f_s)	300 kHz
Primary inductor (L_1)	3.35 mF
Secondary inductor (L_2)	579.16 µF
Output capacitor (C_o)	15 µF
Diode forward voltage ($V_{D_{FWD}}$)	818.09 mV
Duty cycle (D)	0.5275

Figure 7.10– Simulated output voltage waveform.
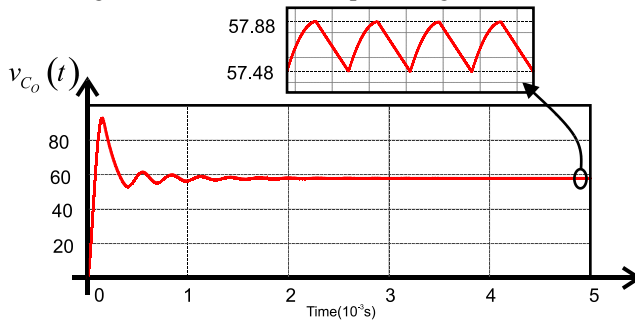
Source: Own elaboration.

Figure 7.11 – Simulated coupling capacitor voltage waveform.
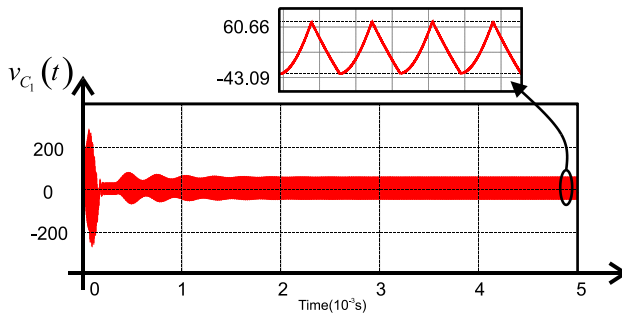
Source: Own elaboration.

Figure 7.12 – Simulated coupling capacitor current waveform.
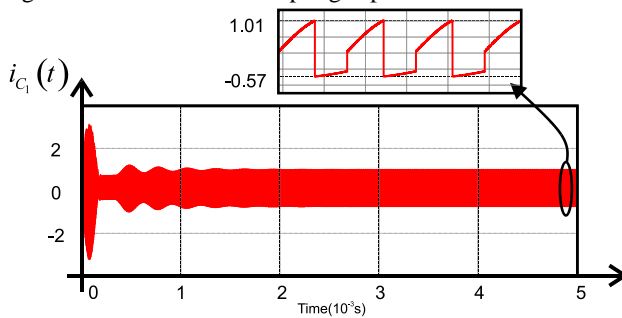
Source: Own elaboration.

Table XXI – Open loop simulation's specifications.

Parameter	Calculated	Simulated	Error (%)
$V_{C_{1M}} = V_{C_{2M}}$	60.961 V	60.659V	0.377
$V_{C_{1m}} = V_{C_{2m}}$	-43.526 V	-43.090 V	0.538
$I_{L_{1M}}$	730.881 mA	728.449 mA	0.333
$I_{L_{1m}}$	570.756 mA	569.057 mA	0.298
$I_{L_{2M}}$	1.018 A	1.021 A	0.294
$I_{L_{2m}}$	55.412 mA	55.870 mA	0.819
$V_{S_M} = V_{D_M}^*$	746.146 V	744.986 V	0.155
$V_{S_m} = V_{D_m}^*$	538.579 V	537.471 V	0.206
ΔV_{C_o}	408.617 mV	402.415 mV	1.032
$I_{C_{RMS}}$	657.653 mA	657.081 mA	0.087
$I_{L_{1RMS}}$	656.316 mA	655.889 mA	0.065
$I_{S_{RMS}}$	932.709 mA	932.432 mA	0.029
$I_{D_{RMS}}$	5.220 A	5.216 A	0.076
$I_{C_{oRMS}}$	3.906 A	3.905 A	0.025

7.5 Final considerations

In this Chapter, the components are sized, according to power, switching frequency, applied voltages and current stress, always observing the load characteristic. Different from a conventional Flyback, the inductance values were sized with respect to their relative resonance frequency parameters $\mu_{1,2}$ in order to provide desired load characteristic and increased efficiency. Some steps have been provided to minimize losses associated with leakage inductance. A comparison between simulated and calculated results have shown a maximum error of 1.032%, validating the equations so far presented.

8 EXPERIMENTAL RESULTS

This Chapter presents the experimental results, which consisted in two parts. The first part presents the experimental results using the film capacitors presented in section 7.3.5.1 to validate the system's performance and acknowledge its stability. The second part presents the results of the metal plate capacitors, and, therefore, are more meaningful. Primary and secondary layout, shown in Appendixes I and J, respectively, were developed to work with either film capacitors or metal plates connected through cables.

To generate signals, it was used a DSP from Texas Instruments (LAUNCHXL-F28069M), shown in Figure 8.1. In order to supply auxiliary voltage for DSP and gate driver, it was used an AC/DC Converter 5V +/- 15 V 66 W (RT-65 Series) from Mean Well, shown in Figure 8.2 (a). Notice that the power related to the signal generation were not accounted in the overall efficiency. A 1-phase Variac, shown in Figure 8.2 (b), was used for protection. The DC voltage of the full-bridge rectifier was observed while varying the Variac, and it always set to 305.5 V dc. In Figure 8.3, it is presented the prototyped devices.

Regarding measurements, it was used a power analyzer PA400 and Scope MD3014, both from Tektronix.

Figure 8.1 – DSP LAUNCHXL-F28069M.

Source: [Texas Instruments].

Figure 8.2 – Simulated coupling capacitor voltage waveform.

(a)　　　　　　　(b)

Source: Own elaboration.

Figure 8.3 – Prototyped: (a) gate driver, (b) passive clamping circuit.

(a)   (b)
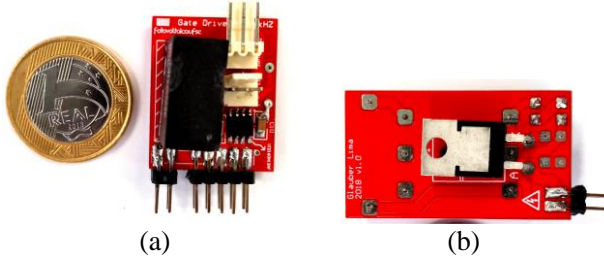
Source: Own elaboration.

8.1 Prototype's waveforms

8.1.1 First setup

The first setup, shown in Figure 8.4, had the purpose to first validate the theory using a film capacitor. In Figure 8.5, it is presented where the coupling capacitances were placed. The experimental specification is presented in Table XXII and it is in accordance with the resistive load available at the laboratory. Note that, different from simulation results, a practical 0.54 duty cycle was used. The reason for this is that the analysis presented in previous chapters did not consider the conductive and switching loss in the circuit. These non-idealities caused voltage drop in the circuit, and therefore, an actual larger duty cycle was needed to compensate. Another reason is that previous theory did not include the leakage inductance of the coupled inductor.

Table XXII – First setup's experimental specifications.

Specification	Value
Rated power (P)	201 W
Output voltage (V_o)	57.75 V
Input voltage (V_i)	305.5 V
Resistive load (R_o)	16.6 Ω
Coupling capacitance (C_1)	9.98 nF
Coupling capacitance (C_2)	10.04 nF
Switching frequency (f_s)	300 kHz

Primary inductor (L_1)	3.35 mH
Secondary inductor (L_2)	579.16 μH
Output capacitor (C_o)	15 μF
Duty cycle (D)	0.54

The first step is to check driving signal, maximum voltage across switch elements and maximum current RMS current, as presented in Figure 8.6. Notice that a filter mode was applied for the isolated voltage probes to avoid noise or unrealistic information whenever it was convenient.

Figure 8.4– First experimental Setup: complete view.

Source: Own elaboration.

Figure 8.5 – Film coupling capacitances were placed in the primary circuit.

Source: Own elaboration.

Drain-to-source peak voltage was 860 V instead of 1000 V designed to clamp. The reason is that, again, the lossless theory presented did not account for damping in the circuit. In most waveforms, it is also observed an oscillation of approximately 5 MHz due to stray inductances.

In Figure 8.7, it is presented the detailed gate waveform. High frequency spikes could only be observed during tests. Rise and fall times kept within 20 ns.

Figure 8.6 – Waveforms: Gate-to-souce voltage (dark blue), Drain-to-source voltage (purple), Reverse diode voltage (light blue) and diode current (green).
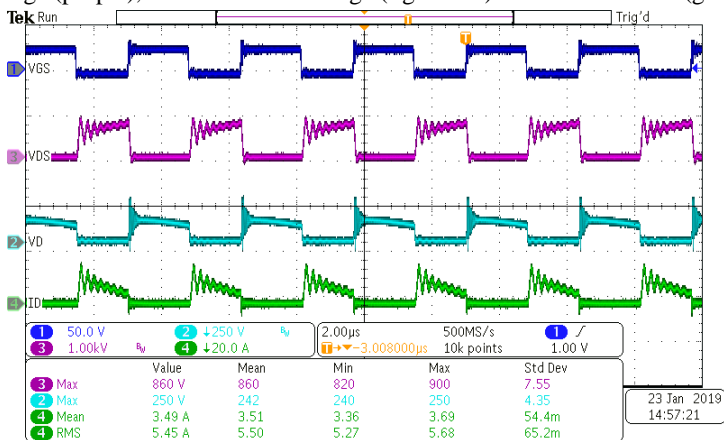
Source: Own elaboration.

Figure 8.7 – Detailed waveform: Gate-to-souce voltage (dark blue).
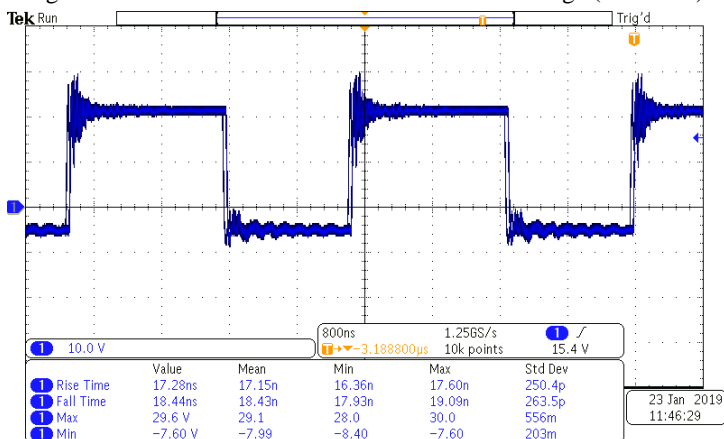
Source: Own elaboration.

In Figure 8.8, it is presented the detailed diode waveforms. A peak voltage spike of 470 V across the diode is observed, due to reverse recovery phenomenon, even though it is a SiC Schottky! Notice that,

maximum reverse voltage calculated, shown in section 7.3.3, resulted in 121.1 V, but it is not enough to size the component. The waveforms of the voltage and current across inductors L_1 and L_2 (primary values) are presented in Figure 8.9.

Figure 8.8 – Detailed waveforms: Reverse diode voltage (light blue) and diode current (green).
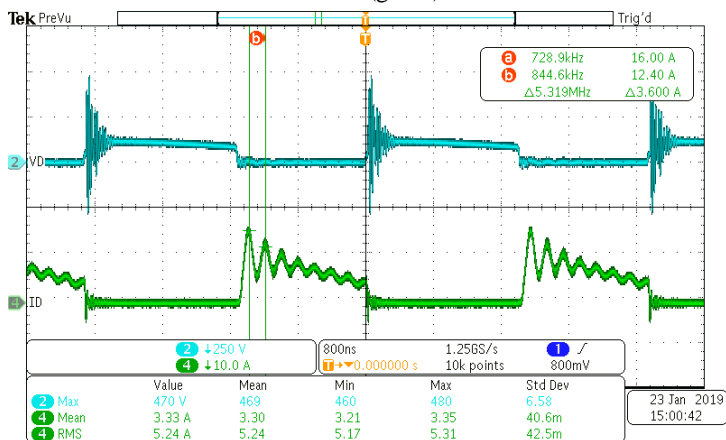
Source: Own elaboration.

Figure 8.9 – Waveforms: Voltage (purple) and current (green) across inductor L_1, and Voltage (dark blue) and current (ligh blue) across inductor L_2 (primary).
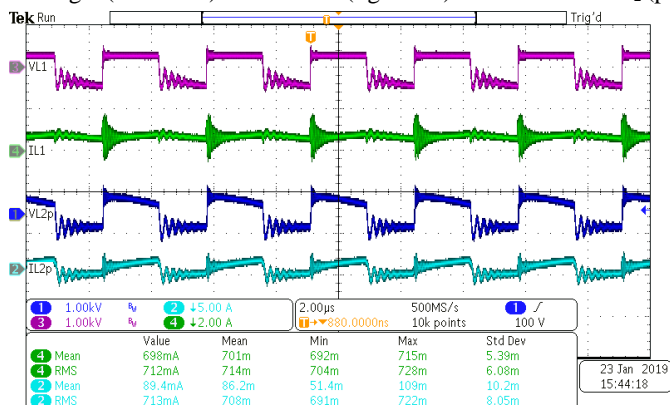
Source: Own elaboration.

In Figure 8.10 and Figure 8.11 are presented the detailed of the inductors L_1 and L_2, respectively. Again, an oscillation of approximately 5 MHz is observed during the demagnetizing (second subinterval) of the inductors. Notice that, different from a conventional Flyback, the average current value of the primary winding of L_2 is almost zero, a benefit.

Figure 8.10 – Detailed waveforms: Voltage (purple) and current (green) across inductor L_1.
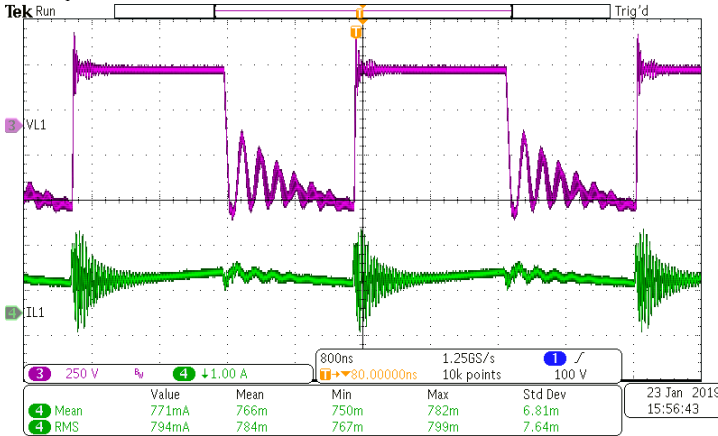
Source: Own elaboration.

Figure 8.11 – Detailed waveforms: Voltage (dark blue) and current (ligh blue) across inductor L_2.
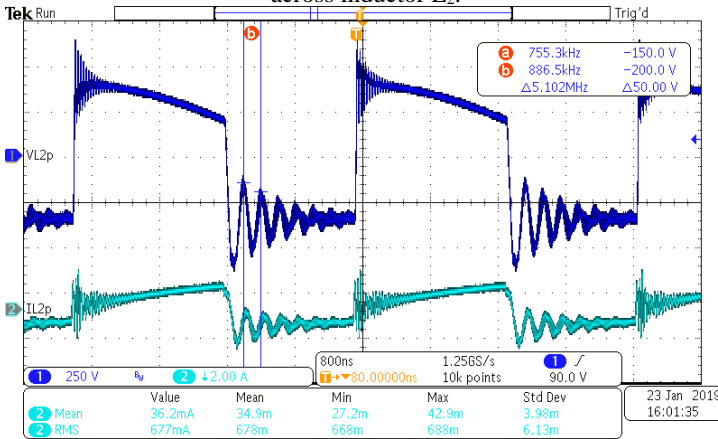
Source: Own elaboration.

The voltage and current waveforms across the coupling capacitors are shown in Figure 8.12. Current in the coupling capacitors are electrically the same, which is the same of the primary winding current in L_2. Note that the voltages were measured with opposite polarities.

Figure 8.12 – Waveforms: Voltages across the coupling capacitor C_1 (dark blue) and C_2 (ligh blue) and current across C_1 (green).
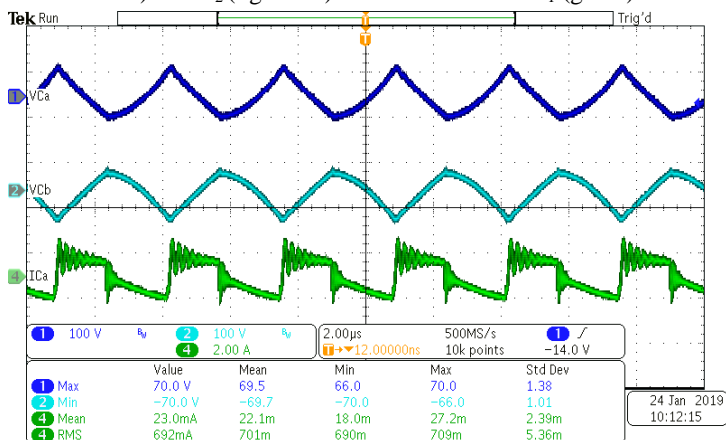
Source: Own elaboration.

Figure 8.13 – Detailed Waveforms: Voltages (dark blue) and current (gree) acrosss the coupling capacitor C_1.

Source: Own elaboration.

In Figure 8.13 the voltage and current across C_1 is presented with better details. Its peak voltage 65.6 V a and a clean waveform is observed, similar to simulation results (approximately 61 V) presented in Table XXI, an error of 6.5% On the other hand, the 5 MHz appeared in the current waveform during second subinterval. Note that the current measured is misleading, as the probe should have been used with the other polarity. The RMS value (704 mA) presented satisfactory results regarding calculated value (657 mA), an error of 7.1%.

Finally input and output waveforms of the prototype are presented in Figure 8.14. Taking the measurement from the scope, apparent power was 399.6 VA and input power was 221 W. Therefore, power factor of 0.5 and efficiency of approximately 90% is estimated through scope measurements. These results give a general idea, but can be misleading since the scope is not the proper equipment for measurements. In the following section, with metal plate capacitor setup, a power analyzer was used to measure in a proper way.

Figure 8.14 – Waveforms: Input grid voltage (dark blue), input grid current (purple), input active power (red), output voltage (light blue) and output current (green).
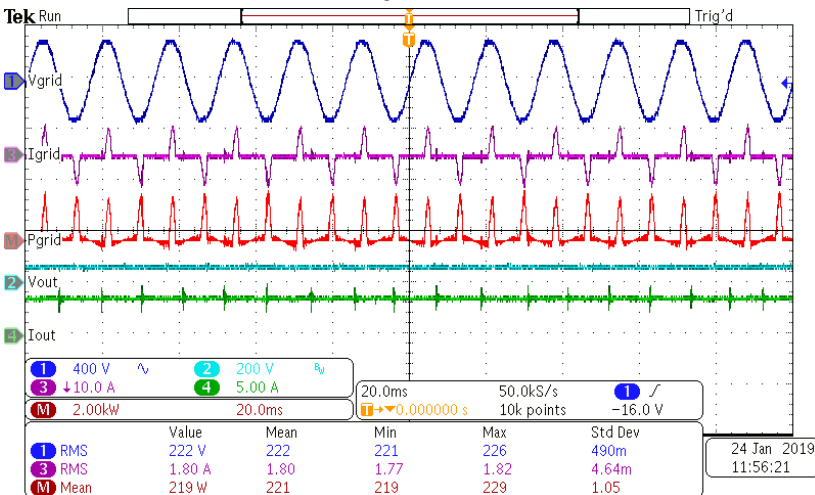
Source: Own elaboration.

8.1.2 Second setup

The second setup is presented in Figure 8.15. As it can be seen, the only difference from first setup is the use of actual metal plate capacitors. Therefore, the capacitance value of the experiment is 7.1 nF for each capacitor. As the capacitance changes from 10 nF (70%), so will slightly change static characteristics since there is a decrease in the ratios from $(\mu_1, \mu_2) = (7.72, 3.21)$ to $(\mu_1, \mu_2) = (6.5, 2.7)$. As the static gain increased, the output voltage resulted in 58.3 V. In Figure 8.16, it is shown the driving signal when the converter is not in operation, showing a clean waveform with no spikes or oscillation. Under such circumstances, the measured rise time was 26.8 ns and fall time 18.8 ns. At rated condition, however, spikes and oscillation are observed across the gate voltage, as presented in Figure 8.17.

Figure 8.15 – Second experimental setup : (a) Primary side, (b) Secondary side.

Source: Own elaboration.

It is also presented the switch waveforms: voltage and current. Notice that, the voltage is clamped at 730 V instead of 860 V in previous setup, due to decreased total voltage applied across the leakage

inductance. As shown in (7.40), passive clamping circuit is dependent of voltage across the coupling capacitors. However, the circuit has not been adjusted so that the performance of the converter could have been verified under capacitance variations.

Figure 8.16 – Detailed waveform: Gate-to-souce voltage (dark blue).
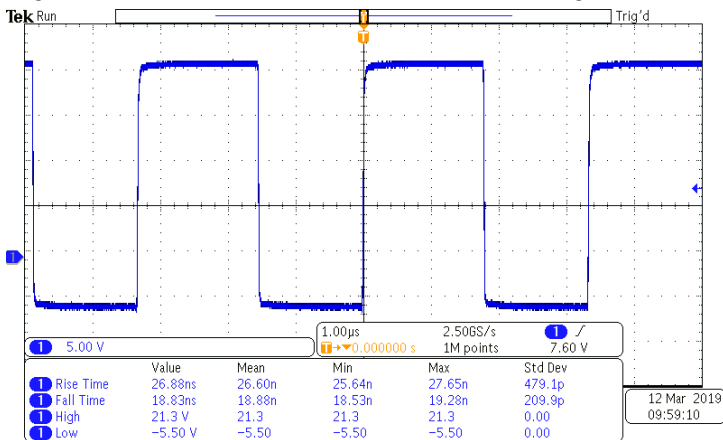
Source: Own elaboration.

Figure 8.17 – Waveforms: Gate-to-souce voltage (dark blue), Drain-to-source voltage (light blue), and switch current (red).
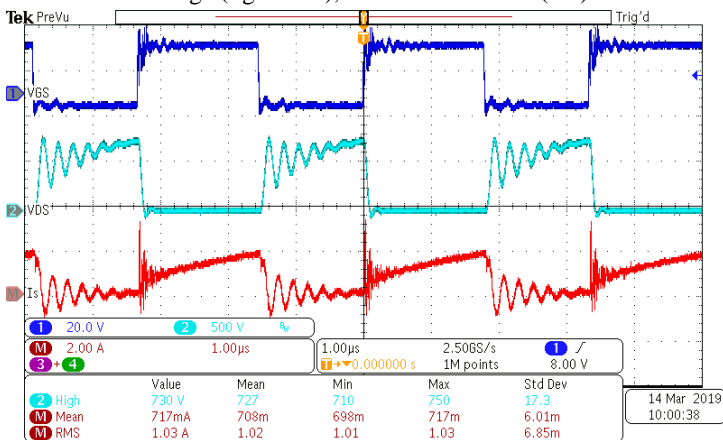
Source: Own elaboration.

In Figure 8.18, it is presented the reverse voltage across the diode and its current. A peak voltage of 404 V across the diode is observed,

which compared with previous tests, resulted in a reduction of approximately 65 V. Regarding diode current, a peak of 17.6 A is presented with oscillation kept around 5 MHz. Figure 8.19 presents the waveform across L_1, in which mean and RMS kept practically the same with respect to previous experiments, but with increased current spikes.

Figure 8.18 – Detailed waveforms: reverse biased diode voltage (dark blue) and diode current (light blue).
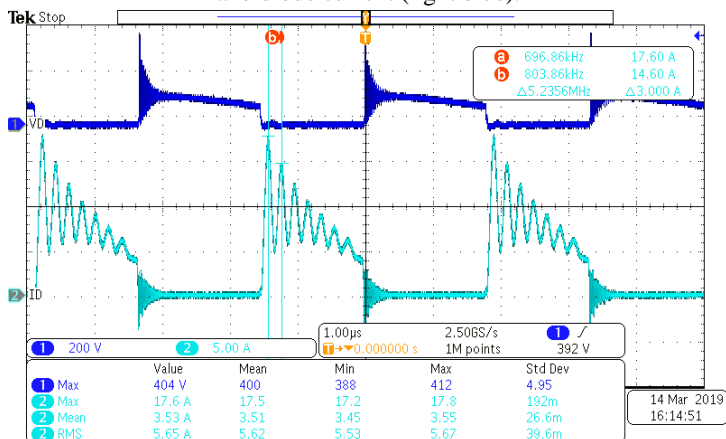
Source: Own elaboration.

Figure 8.19 – Detailed waveforms: Voltage (light blue) and current (green) across inductor L_1.
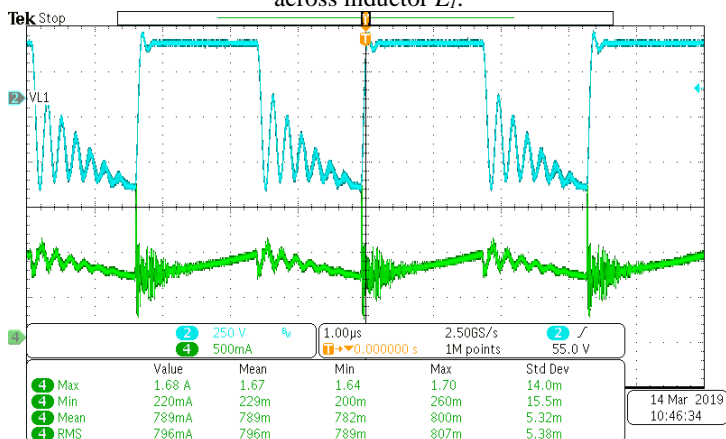
Source: Own elaboration.

In Figure 8.20 and Figure 8.21 are presented, respectively, the primary and secondary waveforms of L_2. An increase compared with first setup of the RMS values are observed (8% across primary winding and 7% across secondary winding. Average value maintains its null feature across primary winding and an increase of 1.75% in secondary.

Figure 8.20 – Detailed waveforms: Voltage (dark blue) and current (light blue) across inductor L_2 (primary side).
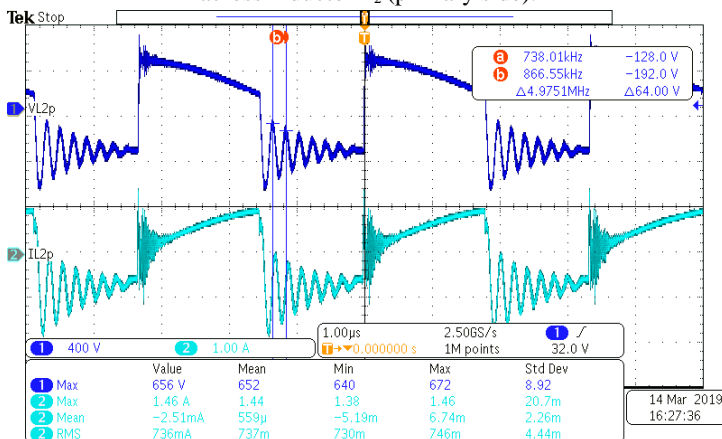
Source: Own elaboration.

Figure 8.21 – Detailed waveforms: Voltage (dark blue) and current (ligh blue) across inductor L_2 (secondary).
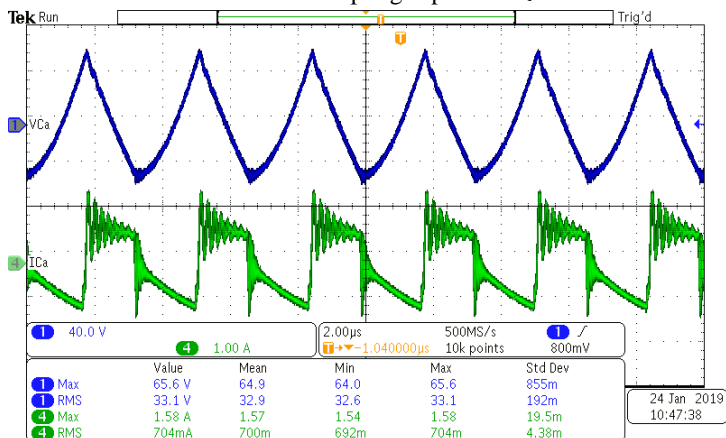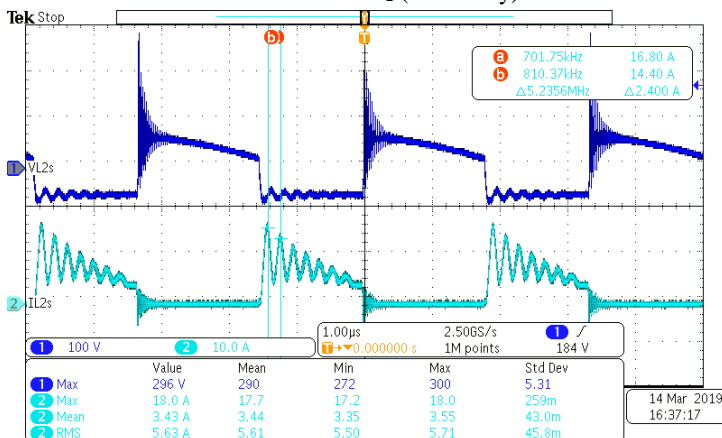

Source: Own elaboration.

Figure 8.22 – Waveforms: Voltages across the coupling capacitor C_1 (dark blue) and C_2 (light blue).
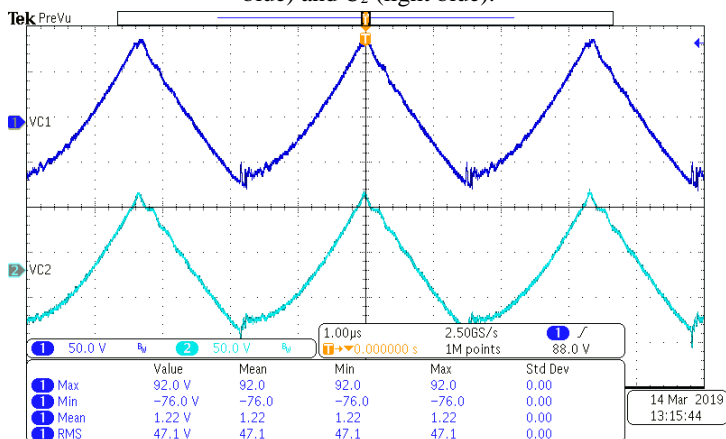
Figure 8.23 – Detailed Waveforms: Voltages (dark blue) and current (purple) acrosss the coupling capacitor C_1.
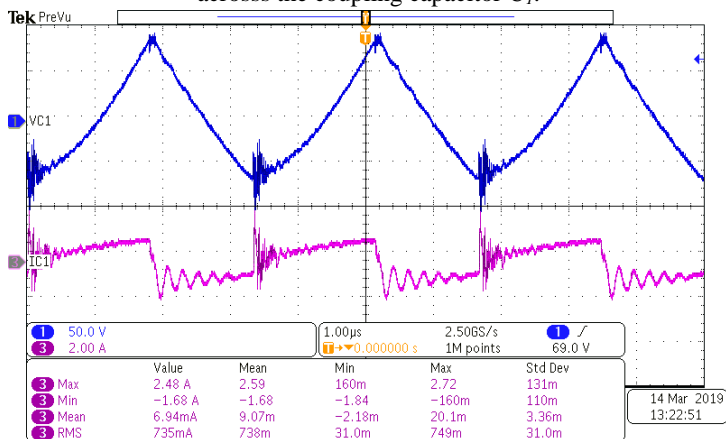
The voltage waveforms across the coupling capacitors are shown in Figure 8.22. The most significant differences between both setups are found in these waveforms. Peak voltage went from 65.6 V in previous experiment to 92 V, a variation of 42 %, whereas RMS value went from 33 V to 47 V, corresponding to a variation 27%. More spikes are noticed in the beginning of the first subinterval, when the MOSFET starts to

conduct. One reason for this to occur is that the connection of the plate capacitors is done using cables, which provokes a dynamic of very high frequencies due to stray inductances. The current in the coupling capacitor is shown in Figure 8.23, which is the same current of primary winding shown in Figure 8.20. Finally input and output waveforms are presented in Figure 8.24.

Figure 8.24 – Waveforms: Input grid voltage (dark blue), input grid current (purple), input active power (red), output voltage (light blue) and output current (green).
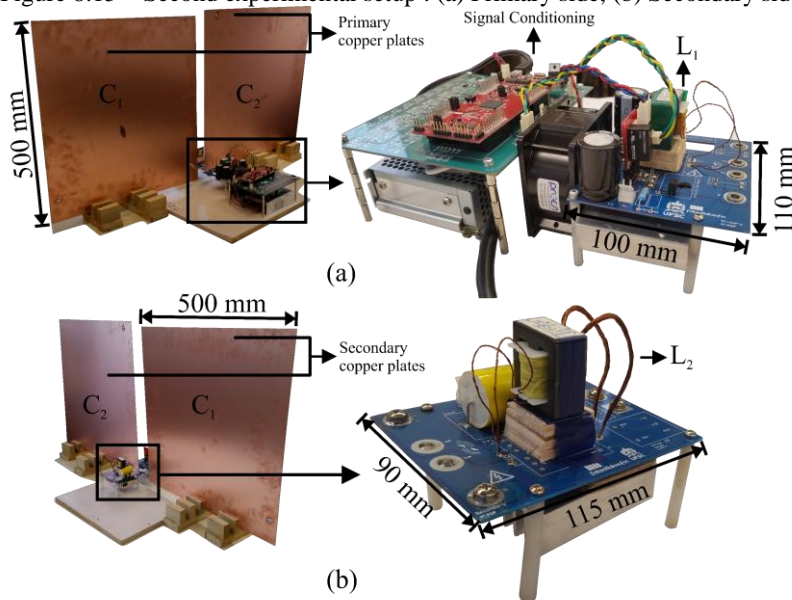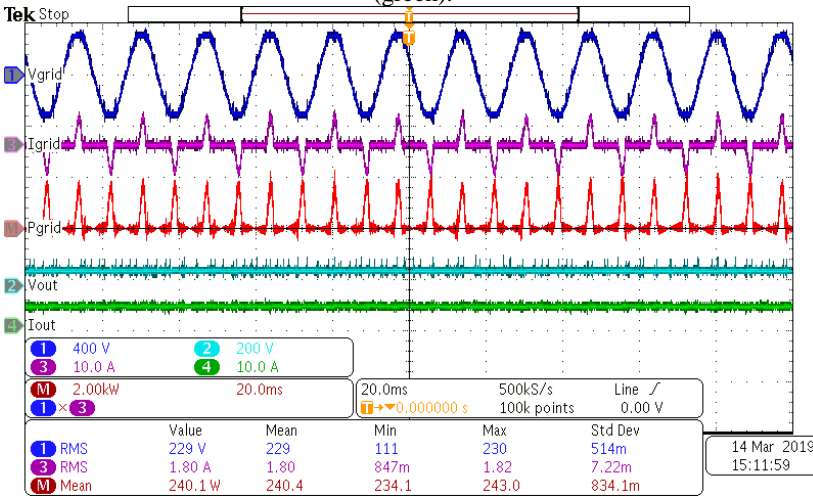

Source: Own elaboration.

8.2 Efficiency curve

Still testing second setup, the overall efficiency curve against output power was taken using a PA400 Power Analyzer from Tektronix, as shown in Figure 8.25. Output power varied from about 70 W to about rated power, 200 W. The tests consisted in keeping duty cycle and input DC voltage constant, while resistive load was varied appropriately. Maximum efficiency found was 85.9%. Regarding power quality, at rated condition, power factor was 0.6. The input voltage grid had a 3.52 % THDv , whereas current had 123.89 % THDi.

Figure 8.25 – Overall efficiency grid-to-load.
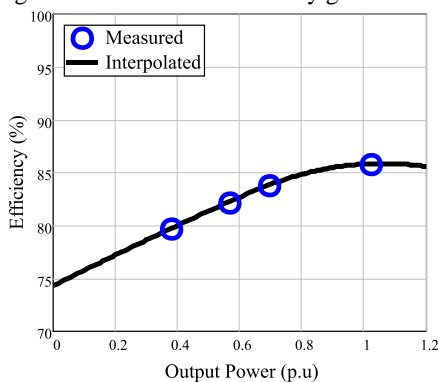
Source: Own elaboration.

As presented in Appendix G, an estimated loss trough the circuit's component is calculated. The results have shown a total loss of 23.2 W, resulting in an overall efficiency of 89.6%. Indeed, only DC loss was used in cupper loss of the circuit, indicating that more loss should be expected in the inductors and the coupling capacitors. Besides, rise and fall time of MOSFET in practice was higher than datasheet's information, misleading to lower loss. A distribution of the estimated loss is presented in Figure 8.26. Notice that the energy associated with leakage inductance and absorbed by the clamping circuit represents most of the of the loss, followed by MOSFET loss and bridge rectifier.

Figure 8.26 – Estimated loss through the converter.
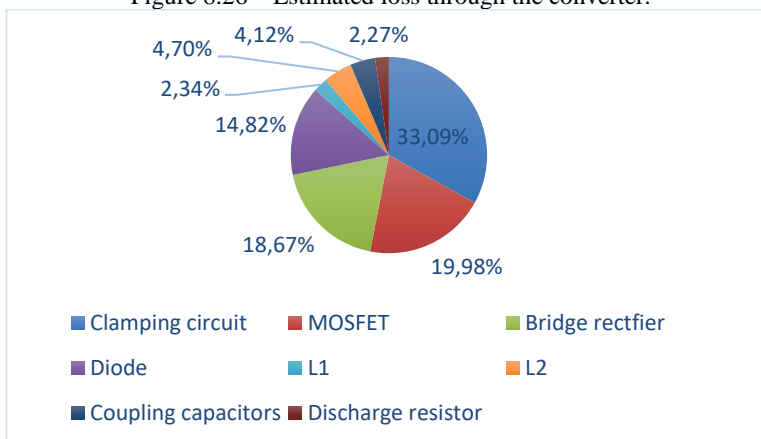
Source: Own elaboration.

8.3 Final considerations

The results presented in this Chapter validates the theory, reaching close values and waveforms. Although the converter was designed for a 10 nF coupling capacitance, it still kept its static characteristic almost constant at relatively good efficiency for a 7.1 nF coupling capacitance, that is, 70% of rated coupling condition. This result stands out with respect to resonant converters, that requires a high degree of impedance matching, meaning complex filters or frequency variation. The reason for keeping its static gain and characteristic almost constant can be observed through the load characteristic plane, where output parametrized current kept in the CCM region. It can be concluded that, by oversizing μ_1 and μ_2, the converter tends to keep its CCM characteristics if the coupling capacitances decreases.

Peak overall efficiency of 86% was really satisfactory, considering that no sophisticated switching technique was implemented to deal with leakage inductance and switching loss. It was concluded that the energy associated with leakage inductance plus the switching energy makes up to at least 50% of the total loss. Such loss can be mitigated when operating close to DVM or DQRM region, since switching operation approaches ZVS, while leakage associated loss decreases up to (7.41).

Better results can be evaluated if the passive clamping circuit is redesigned, considering now that voltage across leakage inductance is decreased, and therefore, more efficient. However, the presented results also validate the good performance of the converter over the coupling capacitance range variation.

9 CONCLUSION

A study of a 200 W modified Flyback converter, operating in CCM, with 86% overall efficiency, applied in CPT for wireless battery charging implementation and specified for a 58 V EV was presented and validated through experimental results, that confirmed theoretical and deduced equations.

Regarding classical PWM converter theory, a new approach that do not neglect neither voltage or current ripple was important to precisely express the static gain as a function of reactive elements, switching frequency and duty cycle. Indeed, such study is valid or may easily be adapted to any 4th order PWM converter, as they are a specific case of the developed theory in this thesis. Not only the static gain, but all the initial conditions in CCM has been successfully expressed, from which a clever parametrization of the output current was responsible for describing the converter in a generic way. Therefore, a multivariable problem is synthesized in two main parameters: static gain and output parametrized current. The theory presented important tools for designing and understanding the low coupling capacitance effect on 4th order PWM converters.

The strategy of using Constant Power Load (CPL) theory for DCM and DVM and their boundary conditions was responsible for easily expressing their load characteristic without the need of equating their topological states. Understanding the regions DCM, DVM and DQRM is of great importance, mainly for PWM converters applied CPT systems, in which low coupling capacitance causes high voltage excursion as well as high resonance frequency comparable with switching frequency.

The criteria of keeping low magnetizing inductance of the coupled inductor in secondary stage and large self-inductance of the primary stage was important to provide good efficiency, even though the converter is hard switched at 300 kHz and contains leakage inductance. This fact indicates that with an optimization methodology, efficiency can increase even further. It might be possible that the modified Flyback converter overcomes the conventional Flyback in terms of efficiency. That is because the modified version can operate in DVM or DQRM region, switching with ZVS or ZVS and ZCS. Close to these regions, the modified Flyback is also suitable when passive clamping is performed, as it performs clamping more efficiently.

The tests have shown that the proposed converter is ideal for low power electronic devices, in the same way that a Flyback is ideal for SMPS, at comparable efficiencies and power factor.

9.1 Future studies

It follows some proposals and future works:
1. Implement closed loop control using wireless communication between primary and secondary stages.
2. Future studies are required to understand the consequences of operating in DVM and DQRM regions applied in CPT.
3. Plotting and studying parametrized maximum, minimum and RMS values against parametrized output current plane.
4. Consider important resistances and the magnetizing inductance. Afterwards analyzing the static gain, load characteristic and efficiency of the converter.
5. Verify the cross-coupling capacitance effects on the Flyback converter.
6. Consider the magnetizing inductance during the analysis of the converter. It is also suggested the use of an active clamping circuit and performing traditional ZVS and/or ZCS technique.
7. Performing PFC.
8. Raising the frequency to MHz order.
9. Either designing a converter with larger rated power or integrate other Flybacks using interleaving structures to increase power up to Twizy rated specifications.
10. To use other topologies regarding gain level, other than the coupled inductor of the Flyback. Indeed, through simulation it was observed that a simple Buck converter connected between a Buck-boost converter and the output load was able to provide considerable gain. It is also useful as a power control converter implementation, since it can be performed in the secondary stage, mostly without the need of wireless communication between the two stages.

REFERENCES

[1]   T. Takaishi, A. Numata, R. Nakano and K. Sakaguchi, "Approach to High Efficiency Diesel and Gas Engines," Mitsubishi Heavy Industries Technical Review. 45 (1)., 2008.

[2]   C. T. C. Andrade and R. S. T. Pontes, "Three-Phase Induction Motor Energy Efficiency Standards - - A Case Study," 2013.

[3]   R. Baran, A Introdução de Veículos Elétricos no Brasil: Avaliação do Impacto no Consumo de Gasolina e Eletricidad, Universidade Federal do Rio de Janeiro: Tese de doutorado, 2012.

[4]   B. Frieske, M. Kloetzke and F. Mauser, "Trends in Vehicle Concept and Key Technology Development for Hybrid and Battery Electric Vehicles," in *EVS27 International Battery, Hybrid and Fuel Cell Electric Vehicle Symposium*, Barcelona, Spain, Nov. 2013.

[5]   D. L. Chandler, "New lithium-oxygen battery greatly improves energy efficiency, longevity," MIT, 25 July 2016. [Online]. Available: http://news.mit.edu/2016/new-lithium-oxygen-battery-greatly-improves-energy-efficiency-longevity-0725. [Accessed 17 March 2019].

[6]   E. M. Tanowe, V. L. V. Torres and R. B. Godoy, "A Straightforward Closed-Loop Wireless Power Transfer Battery Charger," *IECON 2016 - 42nd Annual Conference of the IEEE Industrial Electronics Society,* pp. 4476-4481, 2016.

[7]   R. Kochhan, S. Fuchs, B. Reuter, P. Burda, S. Matz and M. Lienkamp, "An Overview of Costs for Vehicle Components, Fuels and Greenhouse Gas Emissions," 2014.

[8]   A. Hoekstra, A. Vijayashankar and V. L. Sundrani, "Modelling the Total Cost of Ownership of Electric Vehicles in the Netherlands," in *EVS30 Symposium*, Stuttgart, Germany, Oct. 2017.

[9]   "Alternative Fueling Station Locator," U.S Departament of Energy, [Online]. Available: https://afdc.energy.gov/stations/#/find/nearest. [Accessed 01 03 2019].

[10]   Energy.gov, "Electric Vehicles: Tax Credits and Other Incentives," U.S Department of Energy, [Online]. Available:

https://www.energy.gov/eere/electricvehicles/electric-vehicles-tax-credits-and-other-incentives. [Accessed 22 04 2019].

[11]   E. A. M. Association, "Interactive map: Electric vehicle incentives per country in Europe," 03 08 2018. [Online]. Available: https://www.acea.be/statistics/article/interactive-map-electric-vehicle-incentives-per-country-in-europe-2018. [Accessed 22 04 2019].

[12]   "Centro de Mobilidade Sustentável (Mob-i)," Parque Tecnológico Itaipu, [Online]. Available: https://www.pti.org.br/pt-br/mob-i. [Accessed 23 04 2019].

[13]   "Renault Twizy brochure," [Online]. [Accessed 22 02 2019].

[14]   C. L. Liu, S. C.Wang, Y. H. Liu and M. C. Tsai, "An optimum fast charging pattern search for Li-ion batteries using particle swarm optimization," *The 6th International Conference on Soft Computing and Intelligent Systems, and The 13th International Symposium on Advanced Intelligence Systems,* pp. 727-732, Nov. 2012.

[15]   "Open Vehcile Monitoring System," OVMS, [Online]. Available: https://www.openvehicles.com/. [Accessed 23 04 2019].

[16]   G. D. Costa, "Equalização Ativa da Tensão em Baterias Conectadas em Série, Aplicando o Conversor CC – CC Flyback no Modo de Condução Descontínua," em *Master's thesis*, Universidade Federal de Santa Catarina (UFSC), 2018.

[17]   G. A. R.-M. M. Chen, "Accurate electrical battery model capable of predicting runtime and I-V performance," *IEEE Transactions on Energy Conversion,* vol. 21, pp. 504-511, 2006.

[18]   J. Shin, S. Shin, Y. Kim, S. Ahn, S. Lee, G. Jung, S. J. Jeon and D. H. Cho, "Design and implementation of shaped magnetic-resonance-based wireless power transfer system for roadway-powered moving electric vehicles," *IEEE Transactions on Industrial Electronics,* vol. 61, nº 3, p. 1179–1192, Mar. 2014.

[19]   G. d. F. Lima and R. B. Godoy, "Modeling and Prototype of a Dynamic Wireless Charging System Using LSPS Compensation Topology," *IEEE Transaction on Industry Applications,* vol. 55, no. 1, pp. 786-793, 2018.

[20]   A. Kumar, S. Pervaiz, C.-K. Chang, S. Korhummel, Z. Popovic and K. K. Afridi, "Investigation of power transfer density enhancement in large air-gap capacitive wireless power transfer systems," *2015 IEEE Wireless Power Transfer Conference (WPTC),* pp. 1-4, 02 Jul 2015.

[21]   M. J. Chabalko, M. S. and A. P. Sample, "Quasistatic Cavity Resonance for Ubiquitous Wireless Power Transfer," *PLOS ONE,* pp. 1-14, 2017.

[22]   K. Agarwal, R. Jegadeesan, Y.-X. Guo and N. V. Thakor, "Wireless Power Transfer Strategies for Implantable Bioelectronics," *IEEE Reviews in Biomedical Engineering,* vol. 10, pp. 136-161, 2017.

[23]   S. Kikuchi, T. Sakata, E. Takahashi and H. Kanno, "Development of Wireless Power Transfer System for Robot Arm with Rotary and Linear Movement," *2016 IEEE International Conference on Advanced Intelligent Mechatronics (AIM),* pp. 1616-1621, 12 Jul. 2016.

[24]   T. Zaid, S. Saat, N. Jamal, S. H. Husin, Y. Yusof and S. Nguang, "A Development of Acoustic Energy Transfer System through Air Medium using Push-Pull Power Converter," *WSEAS Transactions on Power Systems,* vol. 11, pp. 35-42, 2016.

[25]   S. Sasaki, "How Japan Plans to Build an Orbital Solar Farm," IEEE SPECTRUM, 24 04 2014. [Online]. Available: https://spectrum.ieee.org/green-tech/solar/how-japan-plans-to-build-an-orbital-solar-farm. [Accessed 25 04 2019].

[26]   "Inventions & Experiments of Nikola Tesla," [Online]. Available: https://teslaresearch.jimdo.com. [Accessed 25 04 2019].

[27]   WITRICITY, "WiTricity Drives EV Interoperability with New 11 kW Wireless Charging System," WITRICITY, 28 June 2016. [Online]. Available: http://witricity.com/witricity-drives-ev-interoperability-new-11-kw-wireless-charging-system/. [Accessed 17 03 2019].

[28]   J. Dai and D. C. Ludois, "A Survey of Wireless Power Transfer and a Critical Comparison of Inductive and a Capactive Coupling for Small Gap Applications," *IEEE Trans. Power Power Electron.,* vol. 30, no. 11, pp. 6017-6029, 2015.

[29]   V. VU, L. B. M. Kmal, V. P. J. Tay, M. Dahidah, T. Longenthiran and V. Phan, "A Multi-Output Capacitive Charger for Electric Vehicles," in *IEEE 26th International Symposion on Industrial Electronics (ISIE)*, 2017.

[30]   H. Zhang, F. Lu, H. Hoffmann, W. Liu and C. Mi, "A Large Air-Gap Capacitive Power Transfer System with a 4-Plate Capacitive Coupler Structure for Electric Vehicle Charging Applications," em *IEEE Applied Power Electronics Conference and Exposition (APEC)*, Mar. 2016.

[31]   F. Lu, H. Zhang and C. Mi, "A Two-Plate Capacitive Wireless Power Transfer System for Electric Vehicle Charging Applications," *IEEE Trans. Power Electron,* vol. 33, nº 2, pp. 964-969, 2017.

[32]   B. Regensburger, A. Kumar, S. Sinha and K. Afridi, "High-Performance 13.56-MHz Large Air-Gap Capacitive Wireless Power Transfer System for Electric Vehicle Charging," em *IEEE 19th Workshop on Control and Modeling for Power Electronics (COMPEL)*, Jun. 2108.

[33]   "IEEE Standard for Safety Levels with Respect to Human Exposure to Radio Frequency Electromagnetic Fields, 3 kHz to 300 GHz," 03 10 2005. [Online]. Available: http://emfguide.itu.int/pdfs/c95.1-2005.pdf. [Accessed 25 04 25].

[34]   J. Dai and D. C. Ludois, "Single Active Switch Power Electronics for Kilowatt Scale Capacitive Power Transfer," *IEEE Journal Of Emerging and Selected Topics in Power Electronics,* vol. 3, no. 1, pp. 315-323, 2015.

[35]   K. Hanson, J. K. Reed and D. C. Ludois, "Capacitive Power Transfer for Rotor Field Current in Synchronous Machines," *IEEE Transaction on Power Applications,* vol. 27, nº 11, pp. 4638-4645, 2012.

[36]   S. S. Hagen, Capacitive Power Transfer Through Rotational and Sliding Bearings, University of Wisconsin: Master's thesis, 2016.

[37]   E. Culurciello and G. Andreou, "Capacitive Inter-Chip Data and Power Transfer for 3-D VLSI," *IEEE Trans. Circuits and Systems.,* vol. 53, nº 12, pp. 1348-1352, 2006.

[38]   A. P. Hu, C. Liu and H. L. Li, "A Novel Contactless Battery Charging System for Soccer Playing Robot," em *15th*

International Conference on Mechatronics and Machine Vision in Practice, 2008.

[39]   A. M. Sodagar and P. Amiri, "Capacitive coupling for power and data telemetry to implantable biomedical microsystems," em *Proc. 4th Int. IEEE/EMBS Conf. Neural Eng. (NER)*, 2009.

[40]   D. Rozario, "Design of Contacless Capacitive Power Transfer Systems for Battery Charging Apllications," in *Master's thesis*, University of Ontario Institute of Technology, 2016.

[41]   J. Kim, H. Zhang and F. Bien, "Electric Field Coupling Technique of Wireless Power Transfer for Electric Vehicles," em *EEE TENCON Spring Conference*, 2013.

[42]   D. Halliday, R. Resnick and J. Walker, Fundamentos de Física: Eletromagnetismo V.3 8th edition, LTC, 2009.

[43]   H. Nishiyama and M. Nakamura, "Form and Capacitance of Parallel-Plate Capacitors," *IEEE Transactions on Components, Packaging, and Manufacturing Technology,* vol. 17, no. 3, pp. 477-484, 1994.

[44]   J. Dai and D. C. Ludois, "Capacitive Power Transfer Trough a Conformal Bumper for Electric Vehicle Charging," *IEEE Journal of Emerging and Selected Topics in Power Electronics,* vol. 4, no. 3, 2016.

[45]   "The Physics Hypertextbook," [Online]. Available: https://physics.info/dielectrics/. [Accessed 2019 03 18].

[46]   L. Huang, "Capacitive Power Transfer with Advanced Compensation and Power Flow Control," PhD's thesis, University of Auckland, October 2016.

[47]   L. Huang and A. P. Hu, "Defining the mutual coupling of capacitive power transfer for wireless power transfer," *Electronic Letters,* vol. 51, nº 22, 2015.

[48]   L. Huang and A. Hu, "Defining the mutual coupling of capacitive power transfer for wireless power transfer," *Electronic Letters,* vol. 51, no. 22, pp. 1806-1807, 2015.

[49]   F. Lu, H. H. Zhang, Hofmann and C. Mi, "A Double-Sided LCLC-Compensated Capacitive Power Transfer System for Electric Vehicle Charging," *IEEE Trans. Power Electron.,* vol. 30, nº 11, 2015.

[50]   F. Lu, H. Zhang, H. Hofmann and C. Mi, "A Double-SidedLCLC-Compensated Capacitive Power Transfer System for Electric Vehicle Charging," *IEEE Transactions on Power Electronics,* vol. 30, no. 11, pp. 6011-6014, 2015.

[51]   F. Lu, H. Zhang and C. Mi, "A Review on the Recent Development of Capacitive Wireless Power Transfer Technology," *MDPI Energies,* pp. 1-30, 01 11 2017.

[52]   C. Fang, J. Song, L. Lin and Y. Wang, "Practical considerations of series-series and series-parallel compensation topologies in wireless power transfer system application," *2017 IEEE PELS Workshop on Emerging Technologies: Wireless Power Transfer (WoW),* pp. 255-259, 29 06 2017.

[53]   J. Cho, D. T. Y. Tsururda and J. M. R. Davila, "High-Frequency, High-Power Resonant Inverter With eGaN FET for Wireless Power Transfer," *IEEE Trans. Power Electron.,* vol. 33, no. 3, 2018.

[54]   Y. Yusop, H. Husin, S. K. Nguang, S. Saat and Z. Ghan, "Class-E LCCL for Capacitive Power Transfer System," em *IEEE International Conference on Power and Energy (PECon)*, 2017.

[55]   I. Barbi and D. C. Martins, Conversores CC-CC Básicos Não Isolados, Florianópolis: Dos autores, 2006.

[56]   D. Maksimovic and S. Cuk, "A Unified Analysis of PWM Converters in Discontinuous Modes," *IEEE Transactions on Power Electronics,* vol. 6, no. 3, pp. 476-490, 1991.

[57]   I. Barbi and F. P. d. Souza, Conversores CC-CC Isolados de Alta Frequência, Florianópolis: Edição dos Autores, 1999.

[58]   S. Ćuk, "General Topological Properties of Switching Structure," *1979 IEEE Power Electronics Specialists Conference,* pp. 109-130, 18-22 June 1979.

[59]   B.-T. Lin and Y.-S. Lee, "Power-factor correction using Cuk converters in discontinuous-capacitor-voltage mode operation," *IEEE Transactions on Industrial Electronics,* vol. 44, no. 5, pp. 648-653, 1997.

[60]   D. Makismovic and S. Cuk, "A General Approach to Synthesis and Analysis of Quasi-resonant Converters," *IEEE Transactions on Power Electronics,* vol. 6, no. 1, pp. 127-140, 1991.

[61]   K. Yi, J. Jung, B.-H. Lee and Y. You, "Study on a capacitive coupling wireless power transfer with electric vehicle's dielectric substrates for charging an electric vehicle," in *EPE'17 ECCE Europe*, Warsaw, 2017.

[62]   I. Barbi, Eletronica de potencia: projetos de fontes chaveadas, Florianópolis: Ed. do autor 2001, 2001.

[63]   M. Kamil, "Switch Mode Power Supply (SMPS) Topologies (Part I) AN1114 App. Note," Microship Technology Inc., 06 01 2011. [Online]. Available: https://www.microchip.com/wwwAppNotes/AppNotes.aspx?app note=en532115. [Accessed 25 02 2019].

[64]   T. E. Ltda, "http://www.thornton.com.br," 2008. [Online]. Available: http://www.thornton.com.br/produtos/nee_ing.htm. [Accessed 25 02 2019].

[65]   J. Lloyd H. Dixon, "Unitrode Magnetics Design Handbook," Texas Instruments Incorporated, 2001. [Online]. Available: power.ti.com/seminars. [Accessed 2019 02 25].

[66]   A. A. Dauhajre, "Modelling and Estimation of Leakage Phenomena in Magnetic Circuits," Doctoral thesis, California Institute of Technology, Pasadena, California, 1986.

148

Appendix A – Modelling

This Appendix presents the dynamic modelling of the proposed converter. The State-space averaging (SSA) technique was used to find the main transfer functions with respect to duty cycle responsible for controlling a battery charger: output voltage and output current. In general, a battery charger controls the output current during CC mode and the output voltage during CV mode. Therefore, during the CC mode, the current mode control is active, whereas in CV mode is inactivated and vice-versa.

Modelling strategy:

In the modelling, it is considered non-resistive and ideal elements of the equivalent circuit presented in this thesis. Each subinterval is modeled in arrays in which the combination of the state and output equations represent the state-space system. The state vector $x(t)$ is defined by the collection of the currents in each inductor (i_{L1}, i_{L2}) and the voltages across each capacitor $(v_C, v_{C_o}^*)$ as shown in (1.1). The output capacitor is reflected by dividing by n^2 while the input or control variables are defined by the source of the input voltage V_i (1.2). The two outputs will be observed: the output voltage v_{Co} and inductor current i_{L2}. Notice that average value of i_{L2} is the output current.

$$X = \left[i_{L1}, i_{L2}, v_C, v_{Co}^* \right]^T$$
$$= \left[x_1, x_2, x_3, x_4 \right]^T \tag{1.1}$$

$$U = \left[V_i \right]^T \tag{1.2}$$

Applying Kirchhoff's voltage and current law during the first subinterval ($0 \leq t \leq DT_s$), the dynamics of four state variables are obtained through algebraic manipulations:

$$L_1 \dot{x}_1 = V_i \tag{1.3}$$

$$L_2 \overset{\bullet}{x_2} = V_i - x_3 \tag{1.4}$$

$$C_1 \overset{\bullet}{x_3} = x_2 \tag{1.5}$$

$$C_o \overset{\bullet}{x_4} = \frac{-x_4}{R_o^*} \tag{1.6}$$

$$i_{L_2} = \frac{-x_4}{R_o^*} \tag{1.7}$$

Similarly, equations are obtained during second subinterval $\left(DT_s \le t \le T_s \right)$:

$$L_1 \overset{\bullet}{x_1} = x_3 - x_4 \tag{1.8}$$

$$L_2 \overset{\bullet}{x_2} = -x_4 \tag{1.9}$$

$$C \overset{\bullet}{x_3} = -x_1 \tag{1.10}$$

$$C_o^* \overset{\bullet}{x_4} = x_1 + x_2 - \frac{x_4}{R_o^*} \tag{1.11}$$

The state-space is then represented by matrices A_1, B_1, C_a and E_1 during first subinterval are presented in (1.12) and by A_2, B_2, C_b and E_2 during second one, as presented in (1.18) The matrix K is a diagonal matrix containing the storage element.

$$0 \le t \le DT_s$$

$$\begin{cases} K \overset{\bullet}{x} = A_1 x + B_1 u \\ y = C_a x + E_1 u \end{cases} \tag{1.12}$$

$$K = \begin{bmatrix} L_1 & 0 & 0 & 0 \\ 0 & L_2 & 0 & 0 \\ 0 & 0 & C_1 & 0 \\ 0 & 0 & 0 & C_o^* \end{bmatrix} \tag{1.13}$$

$$A_1 = \begin{bmatrix} 0 & 0 & 0 & 0 \\ 0 & 0 & -1 & 0 \\ 0 & 1 & 0 & 0 \\ 0 & 0 & 0 & \dfrac{-1}{R_o^*} \end{bmatrix} \tag{1.14}$$

$$B_1 = \begin{bmatrix} 1 \\ 1 \\ 0 \\ 0 \end{bmatrix} \tag{1.15}$$

$$C_a = \begin{bmatrix} 0 & 0 & 0 & 1 \\ 0 & 1 & 0 & 0 \end{bmatrix} \tag{1.16}$$

$$E_1 = \begin{bmatrix} 0 \\ 0 \end{bmatrix} \tag{1.17}$$

$$DT_s \le t \le T_s$$
$$\begin{cases} K \overset{\bullet}{x} = A_2 x + B_2 u \\ y = C_b x + E_2 u \end{cases} \tag{1.18}$$

$$A_2 = \begin{bmatrix} 0 & 0 & 1 & -1 \\ 0 & 0 & 0 & -1 \\ -1 & 0 & 0 & 0 \\ 1 & 1 & 0 & \dfrac{-1}{R_o^*} \end{bmatrix} \tag{1.19}$$

$$B_2 = \begin{bmatrix} 0 \\ 0 \\ 0 \\ 0 \end{bmatrix} \tag{1.20}$$

$$C_b = \begin{bmatrix} 0 & 0 & 0 & 1 \\ 0 & 1 & 0 & 0 \end{bmatrix} \tag{1.21}$$

$$E_2 = \begin{bmatrix} 0 \\ 0 \end{bmatrix} \tag{1.22}$$

In order to find the behavior of the average and continuous mode, (1.12) and (1.18) are weighted over the duty cycle D, as shown in (1.23)

$$\begin{cases} K\left\langle \overset{\bullet}{x} \right\rangle = A\left\langle x \right\rangle + B\left\langle u \right\rangle \\ \left\langle y \right\rangle = C_c \left\langle x \right\rangle + E\left\langle u \right\rangle \end{cases} \tag{1.23}$$

$$\begin{cases} A = A_1 D + A_2\left(1 - D\right) \\ B = B_1 D + B_2\left(1 - D\right) \\ C_c = C_1 D + C_2\left(1 - D\right) \\ E = E_1 D + E_2\left(1 - D\right) \end{cases} \tag{1.24}$$

Finally, (1.23) is linearized, considering assumption (1.25) through the perturbation of small signals (represented by lowercase letter with symbol "^") around the desired operating point (represented by capital letter), as presented in (1.25). Note that, from this moment, small ripple approximation is assumed and, therefore, a small error is expected!

$$\langle x \rangle = X + \hat{x} \ \text{ if } X \gg \hat{x}$$
$$\langle y \rangle = Y + \hat{y} \ \text{ if } Y \gg \hat{y}$$
$$\langle u \rangle = U + \hat{u} \ \text{ if } U \gg \hat{u} \tag{1.25}$$
$$\langle D \rangle = D + \hat{d} \ \text{ if } D \gg \hat{d}$$

This perturbation and linearization results in equations of DC terms (1.26), first order AC terms (1.27). and second order non-linear AC. Second order terms are neglected as long assumption (1.25) is satisfied.

$$\begin{cases} X = AX + BU \\ Y = C_c X + EU \end{cases} \tag{1.26}$$

$$\begin{cases} K\dot{x} = A\hat{x} + B\hat{u} + \left[(A_1 - A_2)X + (B_1 - B_2)U \right]\hat{d} \\ \hat{y} = C_c\hat{x} + E\hat{u} + \left[(C_a - C_b)X + (E_1 - E_2)U \right]\hat{d} \end{cases} \tag{1.27}$$

By manipulating (1.26), it is possible to obtain the steady state values of X and Y, and hence the steady state average across X and Y, as shown in (1.28).

$$\begin{cases} X = -A^{-1}BU \\ Y = \left(-C_c A^{-1}B + E \right)U \end{cases} \tag{1.28}$$

Finally, by applying Laplace transform in (1.27), using (1.28) and manipulating this equation, it is possible to obtain the desired output transfer functions, as presented in (1.29).

$$\frac{\hat{y}(s)}{\hat{d}(s)} = C_c \left(KsI - K^{-1}A^{-1} \right)^{-1} B_p + E_p \tag{1.29}$$

$$B_P = \left[K^{-1}B^{-1} \quad K^{-1}(A_1 - A_2)X + (B_1 - B_2)U \right] \tag{1.30}$$

$$E_P = \left[E \quad (C_a - C_b)X + (E_1 - E_2)U \right] \tag{1.31}$$

Applying these equations, the transfer function of the output voltage with respect to duty cycle is presented in Eq (A-1). As it can be seen, it is a 4th order plant, as expected. Notice that the turns ratio must be applied accordingly. In Fig. (A-1), it is presented the bode diagram.

$$G_{vo\_d}(s) := \frac{1}{n} \cdot \frac{-2.932e06s^3 + 1.651s^2 + 6.203e17s + 8.035e22}{s^4 + 3856s^3 + 1.265e11s^2 + 4.834e14s + 5.664e1'} \quad Eq:(A-1)$$

Figure: (A-1) – Bode diagram of the transfer function Vo/d: (a) gain, (b) phase.

Transfer Function Vo/d (Gain)

(a)

Transfer Function Vo/d (Phase)

(b)
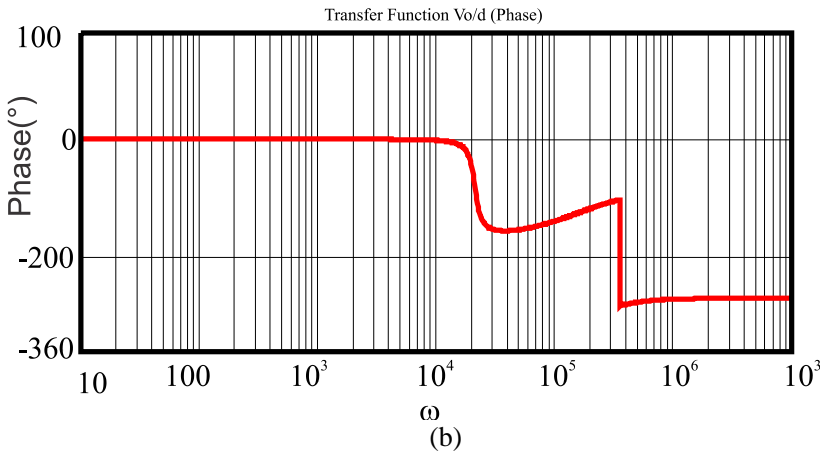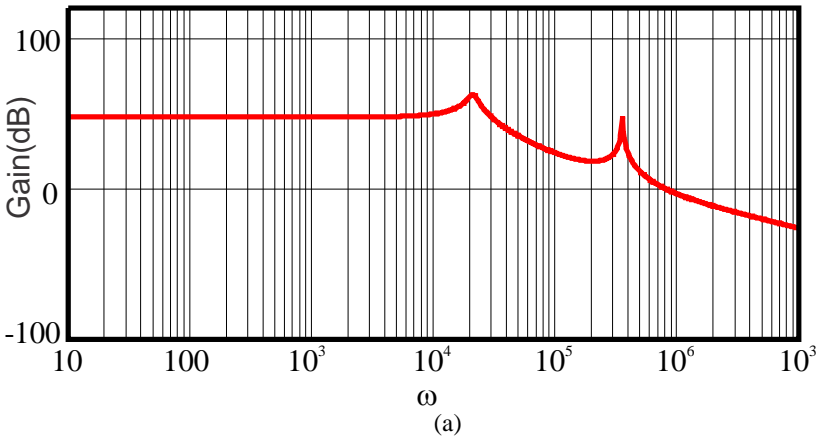
Source: Own elaboration.

The transfer function of the reflected (turns ratio factor is applied) inductor current with respect to duty cycle is presented in Eq (A-2). In Fig. (A-2), it is presented the bode diagram.

$$G_{iL2\_d}(s) := n \cdot \frac{1.299e06s^3 - 2.508e11s^2 + 3.248e16s + 1.291e20}{s^4 + 3856s^3 + 1.265e11s^2 + 4.834e14s + 5.664e19} \quad \text{Eq: (A-2)}$$

Figure: (A-2) – Bode diagram of the transfer function iL2/d: (a) gain, (b) phase.

Transfer Function iL₂/d (Gain)

(a)

Transfer Function iL₂/d (Phase)

(b)
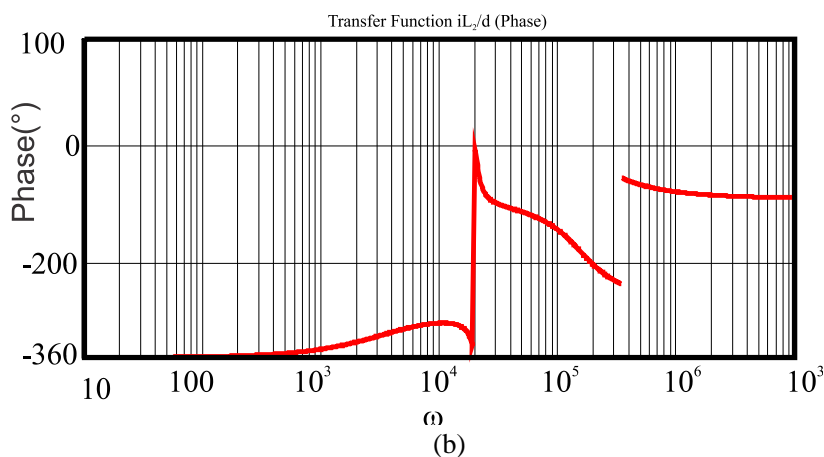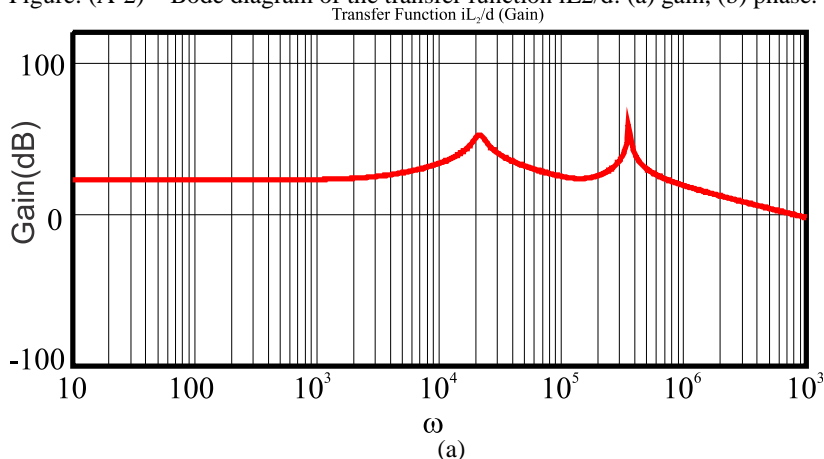
Source: Own elaboration.

Simulation results comparing switched and SSA models are presented in Fig. (A-3). It is possible to notice that, due to small ripple approximation assumption, an error is expected, which is more accentuated in voltage plant.

Figure: (A-3) – Simulation comparisons: (a) Vo/d, (b) iL2/d.

(a)

(b)
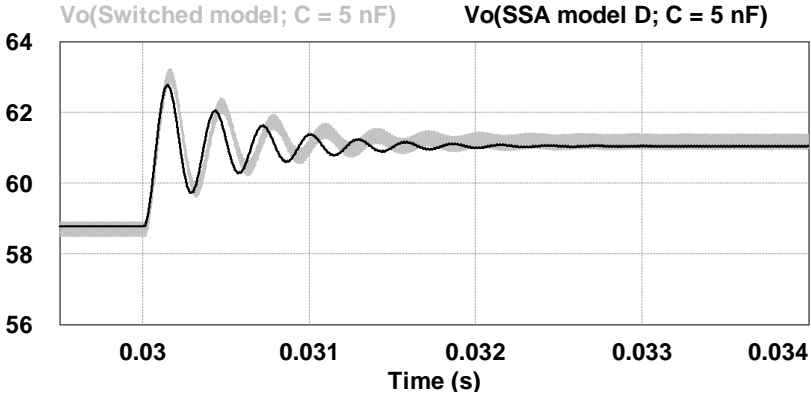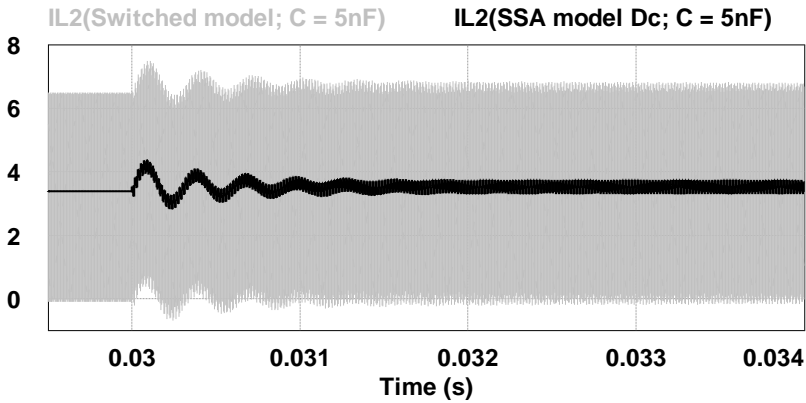
Source: Own elaboration.

Appendix B – Modified Flyback Project

Universidade Federal de Santa Catarina
Centro Tecnológico
Programa de Pós-Graduação em Engenharia Elétrica
Instituto de Eletrônica de Potência

fotovoltaicaufsc

Master's student: Glauber de Freitas Lima
Advisor: Prof. Dr. Ivo Barbi

Modified Flyback Applied in Capacitive Wireless Power Transfer Project

Fixed specifications   To simulation   Test operating mode: CCM
Calculated values   Function

FIXED PARAMETERS

$V_{in} := 220 \cdot V$ — Grid voltage RMS (V)

$V_o := 54 \cdot V$ — Nominal battery voltage @50%SOC (V)

$V_{o\_min} := 49.25 \cdot V$ — Minimum battery voltage @10% SOC (V)

$V_{o\_max} := 59.8 \cdot V$ — Maximum battery voltage @90%SOC (V)

$n := 6$ — Turns ratio

$V_D := 0 \cdot V$ — Diode forward voltage (V)

$V_{o}' := (V_o + V_D) \cdot n = 324\,V$ — Reflected nominal voltage (V)

$V_{o'\_min} := (V_{o\_min} + V_D) \cdot n = 295.5\,V$ — Reflected minimum battery voltage (V)

$V_{o'\_max} := (V_{o\_max} + V_D) \cdot n = 358.8\,V$ — Reflected maximum battery voltage (V)

$V_{i\_max} := V_{in} \cdot \sqrt{2} = 311.127\,V$ — Maximum input voltage (V)

$V_{i\_min} := 0.9 \cdot V_{i\_max} = 280.014\,V$ — Minimum input voltage (V)

$V_i := \dfrac{V_{i\_max} + V_{i\_min}}{2} = 295.571\,V$ — Nominal input voltage (V)

$G_{min} := \dfrac{V_{o'\_min}}{V_{i\_max}} = 0.95$ — Minimum static gain

$G_{max} := \dfrac{V_{o'\_max}}{V_{i\_min}} = 1.2814$ — Maximum static gain

1

158

$$G_n := \frac{V_o{'}}{V_i} = 1.096$$

Nominal static gain

$$P := 200 \cdot W$$

Rated Power (W)

$$f_s := 300 \cdot kHz$$

Switching frequency (Hz)

$$T_s := \frac{1}{f_s}$$

Switching period (s)

$$\omega_s := 2 \cdot \pi \cdot f_s = 1.885 \times 10^6 \frac{1}{s}$$

Angular switching frequency (rad/s)

$$I_o := \frac{P}{V_{o\_max}} = 3.344 \, A$$

Constant current mode (A)

$$I_o{'} := \frac{I_o}{n} = 0.557 \, A$$

Reflected constant current (A)

$$I_i := \frac{P}{V_{i\_min}} = 0.714 \, A$$

Maximum avarage input current (A)

$$D_{aprox} := \frac{G_n}{1 + G_n} = 0.523$$

Aprox. nominal duty cycle

$$D_{aprox\_min} := \frac{G_{min}}{1 + G_{min}} = 0.487$$

Aprox. minimum duty cycle

$$D_{aprox\_max} := \frac{G_{max}}{1 + G_{max}} = 0.562$$

Aprox. maximum duty cycle

$$C := 5nF$$

Equivalent coupling capacitance.

$$\gamma_o := \frac{I_o{'}}{2 \cdot f_s \cdot C \cdot V_i} = 0.629$$

Nominal output parametarized current

$$\gamma_{o\_max} := \frac{I_o{'}}{2 \cdot f_s \cdot C \cdot V_{i\_min}} = 0.664$$

Maximum output parametarized current

$$\gamma_{o\_min} := \frac{I_o{'}}{2 \cdot f_s \cdot C \cdot V_{i\_max}} = 0.597$$

Minimum output parametrized current

$$V_{i\_ch} := V_{i\_min} = 280.014 \, V$$

Chosen input voltage (V)

$$V_{o\_ch} := V_{o\_max}$$

Chosen output voltage (V)

$$V_{o'\_ch} := V_{o\_ch} \cdot n = 358.8 \, V$$

Chosen reflected output voltage (V)

$$G\_ch := \frac{V_{o'\_ch}}{V_{i\_ch}} = 1.281$$

Chosen static gain

2

$\gamma_{o\_ch} := \dfrac{I_o'}{2 \cdot f_s \cdot C \cdot V_{i\_ch}} = 0.66$ Chosen reflected output current

$R_{o'\_ch} := \dfrac{V_{o'\_ch}}{I_o'} = 643.69\,\Omega$ Chosen reflected resistive load

$P_{Max} := 2 \cdot C \cdot f_s \cdot \left(V_{o'\_ch} + V_{i\_ch}\right)^2 = 1.224 \times 10^3\,W$ **Check maximum power**

$D_{Max} := \sqrt{2 R_{o'\_ch} \cdot C \cdot f_s} = 1.39$ **Check maximum duty cycle**

$C_{Min} := \dfrac{P}{2 \cdot f_s \cdot \left(V_{o'\_ch} + V_{i\_ch}\right)^2} = 816.826 \times 10^{-12}\,F$ **Check minimum equivalent coupling capacitance**

LOAD CHARACTERISTIC

$\mu_1 := 8$ Chosen u1

$\mu_2 := 3$ Chosen u2

$L_1 := \dfrac{\mu_1^2}{\omega_s^2 \cdot C} = 3.6025 \cdot mH$ Inductor L1

$L_2 := \dfrac{\mu_2^2}{\omega_s^2 \cdot C} = 506.6059 \cdot \mu H$ Inductor L2

$L_{eq} := \dfrac{L_1 \cdot L_2}{L_1 + L_2} = 444.1477 \cdot \mu H$ Equivalent inducatance

$D_{Min} := 1 - \sqrt{\dfrac{2 L_{eq} \cdot f_s}{R_{o'\_ch}}} = 0.357$ **Check minimum duty cycle**

$P_{Min} := \left(\dfrac{V_{i\_ch} \cdot V_{o'\_ch}}{V_{i\_ch} + V_{o'\_ch}}\right)^2 \cdot \dfrac{1}{2 \cdot L_{eq} \cdot f_s} = 92.819\,W$ **Check minimum power**

$\omega_1 := \dfrac{1}{\sqrt{L_1 \cdot C}} = 2.356 \times 10^5 \dfrac{1}{s}$ *Angular frequency of L1C (rad/s)*

$\omega_2 := \dfrac{1}{\sqrt{L_2 \cdot C}} = 6.283 \times 10^5 \dfrac{1}{s}$ *Angular frequency of L2C (rad/s)*

$G_{CCM}(d, \mu_{1x}, \mu_{2x}) := \dfrac{1 + \dfrac{d \cdot \pi}{\mu_{1x}} \cdot \cot\left[\dfrac{(1-d) \cdot \pi}{\mu_{1x}}\right]}{1 + \dfrac{(1-d) \cdot (\pi)}{\mu_{2x}} \cdot \cot\left(\dfrac{d \pi}{\mu_{2x}}\right)}$ *Static gain function Vo'/Vin*

3

- -

$D_{min} := \text{root}\left(G_{CCM}(d, \mu_1, \mu_2) - G_{min}, d, 0.001, 0.999\right) = 0.4775$ *Minimum duty cycle*

$D := \text{root}\left(G_{CCM}(d, \mu_1, \mu_2) - G\_ch, d, 0.001, 0.999\right) = 0.5502$ *Chosen Duty cycle, which is maximum*

$$\frac{G\_ch + \dfrac{G\_ch \cdot \pi}{\mu_2} \cot\left(\dfrac{D\pi}{\mu_2}\right) - 1}{\left[\dfrac{G\_ch \cdot \pi}{\mu_2} \cdot \cot\left(\dfrac{D\pi}{\mu_2}\right) + \dfrac{\pi}{\mu_1}\left[\cot\left((1-D)\cdot\dfrac{\pi}{\mu_1}\right)\right]\right]} = 0.5502$$

Check duty cycle. If = D => CCM

Normalized static gain
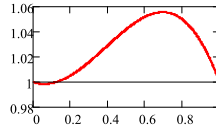
D

Parameterized Maximum and Minimum current and voltage values in reactive elements

$$\varepsilon_{m\gamma}(d, Gama, \mu_{1x}, \mu_{2x}) := 1 - \left[G_{CCM}(d, \mu_{1x}, \mu_{2x})\frac{\pi \cdot (1-d)}{\mu_{2x}} \cdot \cot\left(\frac{\pi \cdot d}{\mu_{2x}}\right) + \frac{Gama}{\left[1 + \frac{\pi \cdot (1-d)}{\mu_{2x}} \cdot \cot\left(\frac{\pi d}{\mu_{2x}}\right)\right]}\right]$$

$$\varepsilon_{M\gamma}(d, Gama, \mu_{1x}, \mu_{2x}) := 1 - \left[G_{CCM}(d, \mu_{1x}, \mu_{2x})\frac{\pi \cdot (1-d)}{\mu_{2x}} \cdot \cot\left(\frac{\pi \cdot d}{\mu_{2x}}\right) - \frac{Gama}{\left[1 + \frac{\pi \cdot (1-d)}{\mu_{2x}} \cdot \cot\left(\frac{\pi d}{\mu_{2x}}\right)\right]}\right]$$

$$I_{L2m\gamma}(d, Gama, \mu_{1x}, \mu_{2x}) := \frac{\pi}{Gama} \cdot \cot\left(\frac{\pi \cdot d}{\mu_{2x}}\right) \cdot \left[\frac{(1 - \varepsilon_{m\gamma}(d, Gama, \mu_{1x}, \mu_{2x}))}{\mu_{2x}} - \frac{2 \cdot \pi \cdot (1-d)}{\mu_{2x}^2} \cdot \frac{G_{CCM}(d, \mu_{1x}, \mu_{2x})}{\sin\left(\frac{2\pi \cdot d}{\mu_{2x}}\right)}\right]$$

$$I_{L2M\gamma}(d, Gama, \mu_{1x}, \mu_{2x}) := \frac{\pi}{Gama} \cdot \cot\left(\frac{\pi \cdot d}{\mu_{2x}}\right) \cdot \left[\frac{(1 - \varepsilon_{m\gamma}(d, Gama, \mu_{1x}, \mu_{2x}))}{\mu_{2x}} - \frac{2 \cdot \pi \cdot (1-d)}{\mu_{2x}^2} \cdot G_{CCM}(d, \mu_{1x}, \mu_{2x}) \cot\left(\frac{2\pi \cdot d}{\mu_{2x}}\right)\right]$$

$$I_{L1m\gamma}(d, Gama, \mu_{1x}, \mu_{2x}) := \frac{\pi}{Gama} \cdot \cot\left[\frac{\pi \cdot (1-d)}{\mu_{1x}}\right] \cdot \left[\frac{(\varepsilon_{M\gamma}(d, Gama, \mu_{1x}, \mu_{2x}) - G_{CCM}(d, \mu_{1x}, \mu_{2x}))}{\mu_{1x}} + \frac{2 \cdot \pi \cdot d}{\mu_{1x}^2} \cdot \cot\left[\frac{2\pi \cdot (1-d)}{\mu_{1x}}\right]\right]$$

$$I_{L1M\gamma}(d, Gama, \mu_{1x}, \mu_{2x}) := \frac{\pi}{Gama} \cdot \cot\left[\frac{\pi \cdot (1-d)}{\mu_{1x}}\right] \cdot \left[\frac{(\varepsilon_{M\gamma}(d, Gama, \mu_{1x}, \mu_{2x}) - G_{CCM}(d, \mu_{1x}, \mu_{2x}))}{\mu_{1x}} + \frac{2 \cdot \pi \cdot d}{\mu_{1x}^2} \cdot \frac{1}{\sin\left[\frac{2\pi \cdot (1-d)}{\mu_{1x}}\right]}\right]$$

Static gain as a function of parametrized output current

$d := 0, 0.01 .. 1$

$\gamma_{DVM}(d, \mu_{1x}, \mu_{2x}) := \text{root}\left(G_{CCM}(d, \mu_{1x}, \mu_{2x}) + 1 - \varepsilon_{M\gamma}(d, Gama, \mu_{1x}, \mu_{2x}), Gama, 10^{-9}, 10^6\right)$ CCM-DVM Boundary

$\gamma_{DCM}(d, \mu_{1x}, \mu_{2x}) := \text{root}\left(I_{L1m\gamma}(d, Gama, \mu_{1x}, \mu_{2x}) + I_{L2m\gamma}(d, Gama, \mu_{1x}, \mu_{2x}), Gama, 10^{-9}, 10^6\right)$ CCM-Dcm Boundary

$$G_x(d, Gama, \mu_{1x}, \mu_{2x}) := \begin{cases} G_{CCM}(d, \mu_{1x}, \mu_{2x}) & \text{if } \gamma_{DCM}(d, \mu_{1x}, \mu_{2x}) \le Gama \le \gamma_{DVM}(d, \mu_{1x}, \mu_{2x}) \\ \left(G_{CCM}(d, \mu_{1x}, \mu_{2x})\frac{\gamma_{DCM}(d, \mu_{1x}, \mu_{2x})}{Gama}\right) & \text{if } Gama < \gamma_{DCM}(d, \mu_{1x}, \mu_{2x}) \\ \left(G_{CCM}(d, \mu_{1x}, \mu_{2x})\frac{\gamma_{DVM}(d, \mu_{1x}, \mu_{2x})}{Gama}\right) & \text{if } Gama > \gamma_{DVM}(d, \mu_{1x}, \mu_{2x}) \end{cases}$$

Load characteristic

4

Gama

Gama
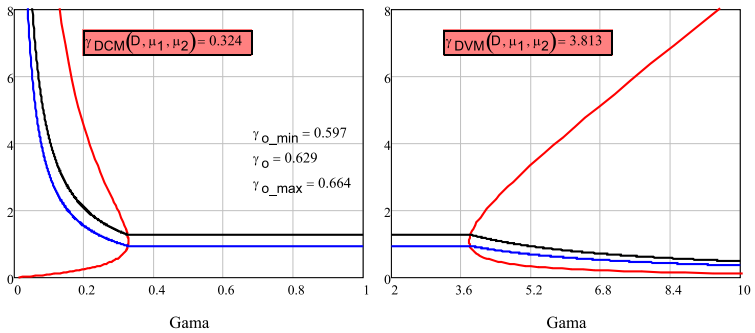
Maximum and minimum critical values

$\gamma_{DCM}(D, \mu_1, \mu_2) = 0.324$ Critical minimum parametrized output currente

$\gamma_{DVM}(D, \mu_1, \mu_2) = 3.813$ Critical maximum parametrized output currente

$P_{DCM} := G_{CCM}(D, \mu_1, \mu_2) V_{i\_ch}^2 \cdot 2 \cdot f_s \cdot C \cdot \gamma_{DCM}(D, \mu_1, \mu_2) = 97.788\,W$ Minimum power

$P_{DVM} := G_{CCM}(D, \mu_1, \mu_2) V_{i\_ch}^2 \cdot 2 \cdot f_s \cdot C \cdot \gamma_{DVM}(D, \mu_1, \mu_2) = 1.149 \times 10^3\,W$ Maximum power

MAXIMUM AND MINIMUM VALUES

Maximum and minimum voltage value across coupling capacitor

$V_{CM} := \varepsilon_{M\gamma}(D, \gamma_{o\_ch}, \mu_1, \mu_2) V_{i\_ch} = 127.583\,V$ VC1max => $V_{C1M} := \dfrac{V_{CM}}{2} = 63.791\,V$

$V_{Cm} := \varepsilon_{m\gamma}(D, \gamma_{o\_ch}, \mu_1, \mu_2) V_{i\_ch} = -87.839\,V$ VC1min => $V_{C1m} := \dfrac{V_{Cm}}{2} = -43.919\,V$

$V_{i\_ch} + V_{o'\_ch} - V_{CM} = 511.231\,V$ If > 0 => ok. Otherwise, DVM or DQRM

Maximum and minimum voltage value across the switching elements

$V_{SM} := \left[\left(1 + G_{CCM}(D, \mu_1, \mu_2)\right) - \varepsilon_{m\gamma}(D, \gamma_{o\_ch}, \mu_1, \mu_2)\right] \cdot V_{i\_ch} = 726.653\,V$

$V_{Sm} := \left[\left(1 + G_{CCM}(D, \mu_1, \mu_2)\right) - \varepsilon_{M\gamma}(D, \gamma_{o\_ch}, \mu_1, \mu_2)\right] \cdot V_{i\_ch} = 511.231\,V$

$V_{DM} := \dfrac{V_{SM}}{n} = 121.109\,V$

$V_{Dm} := \dfrac{V_{Sm}}{n} = 85.205\,V$

Maximum and minimum current values in the inductors

$$I_{L1M} := I_{L1M\gamma}\left(D, \gamma_{o\_ch}, \mu_1, \mu_2\right) I_{o'} = 0.782\,A$$

$$I_{L1m} := I_{L1m\gamma}\left(D, \gamma_{o\_ch}, \mu_1, \mu_2\right) I_{o'} = 0.64\,A$$

$$I_{L2M} := I_{L2M\gamma}\left(D, \gamma_{o\_ch}, \mu_1, \mu_2\right) I_{o'} = 1.052\,A$$

$$I_{L2m} := I_{L2m\gamma}\left(D, \gamma_{o\_ch}, \mu_1, \mu_2\right) I_{o'} = -0.01\,A$$

$$I_{L1m} + I_{L2m} = 0.629\,A \qquad \textit{If > 0 => ok. Otherwise, DCM or DQRMS}$$

Maximum and minimum current values in the switch

$$I_{SM} := I_{L1M} + I_{L2M} = 1.834\,A$$

$$I_{Sm} := I_{L1m} + I_{L2m} = 0.629\,A$$

RMS Values in the switching elements

Switch S

$$I_{SRMS} := \sqrt{\frac{1}{T_s} \cdot \int_0^{D \cdot T_s} \left[\sqrt{\frac{C}{L_2}} \cdot \left(V_{i\_ch} - V_{Cm}\right)\sin\left(\omega_2 \cdot t\right) + I_{L2m}\cdot\cos\left(\omega_2 \cdot t\right) + \left(\frac{V_{i\_ch} \cdot t}{L_1} + I_{L1m}\right)\right]^2 dt} = 0.998\,A$$

Diode D

$$I_{DRMS} := \sqrt{\frac{1}{T_s} \cdot \int_0^{(1-D) \cdot T_s} \left[n \cdot \left[I_{L1M}\cdot\cos\left(\omega_1 \cdot t\right) + \sqrt{\frac{C}{L_1}} \cdot \left(V_{CM} - V_{o'\_ch}\right)\sin\left(\omega_1 \cdot t\right) + \left(-\frac{V_{o'\_ch} \cdot t}{L_2} + I_{L2M}\right)\right]\right]^2 dt} = 5.179\,A$$

RMS Values in the energy storage elements

Inductor L1

$$I_{L1aRMS} := \sqrt{\frac{1}{T_s} \cdot \int_0^{D \cdot T_s} \left(\frac{V_{i\_ch} \cdot t}{L_1} + I_{L1m}\right)^2 dt} = 0.528\,A$$

$$I_{L1bRMS} := \sqrt{\frac{1}{T_s} \cdot \int_0^{(1-D) \cdot T_s} \left[I_{L1M}\cdot\cos\left(\omega_1 \cdot t\right) + \sqrt{\frac{C}{L_1}} \cdot \left(V_{CM} - V_{o'\_ch}\right)\sin\left(\omega_1 \cdot t\right)\right]^2 dt} = 0.483\,A$$

$$I_{L1RMS} := \sqrt{I_{L1aRMS}^2 + I_{L1bRMS}^2} = 0.715\,A$$

_____

Indcutor L2

$$I_{L2aRMS} := \sqrt{\frac{1}{T_s} \cdot \int_0^{D \cdot T_s} \left[\sqrt{\frac{C}{L_2}} \cdot \left(V_{i\_ch} - V_{Cm}\right) \sin\left(\omega_2 \cdot t\right) + I_{L2m} \cdot \cos\left(\omega_2 \cdot t\right) \right]^2 dt} = 0.494\,A$$

$$I_{L2bRMS} := \sqrt{\frac{1}{T_s} \cdot \int_0^{(1-D) \cdot T_s} \left(-\frac{V_{o'\_ch} \cdot t}{L_2} + I_{L2M} \right)^2 dt} = 0.405\,A$$

$$I_{L2RMSp} := \sqrt{I_{L2aRMS}^2 + I_{L1bRMS}^2} = 0.691\,A$$

$$I_{L2RMSs} := I_{DRMS} = 5.179\,A$$

Coupling Capacitor Current

$$I_{CRMS} := I_{L2RMSp} = 0.691\,A$$

Coupling Capacitor Voltage

$$V_{CRMSa} := \sqrt{\frac{1}{T_s} \cdot \int_0^{D \cdot T_s} \left[\left[V_{i\_ch} + \left(V_{Cm} - V_{i\_ch}\right)\cos\left(\omega_2 \cdot t\right)\right] + I_{L2m} \cdot \sqrt{\frac{L_2}{C}} \cdot \sin\left(\omega_2 \cdot t\right) \right]^2 dt} = 49.476\,V$$

$$V_{CRMSb} := \sqrt{\frac{1}{T_s} \cdot \int_0^{(1-D)T_s} \left[\left[V_{o'\_ch} + \left(V_{CM} - V_{o'\_ch}\right)\cos\left(\omega_1 \cdot t\right)\right] - I_{L1M} \cdot \sqrt{\frac{L_1}{C}} \cdot \sin\left(\omega_1 \cdot t\right) \right]^2 dt} = 43.21\,V$$

$$V_{CRMS} := \sqrt{V_{CRMSa}^2 + V_{CRMSb}^2} = 65.692\,V \qquad VC1.rms => \qquad V_{C1RMS} := \frac{V_{CRMS}}{2} = 32.846\,V$$

Output Capacitorr Co

$$V_{o\%} := 1\%$$
Maximum Output voltage ripple

$$C_o := \frac{I_o \cdot D}{f_s \cdot V_{o\%} \cdot V_{o\_min}} = 12.45 \cdot \mu F$$
Output capacitor

$$ESR := \frac{f_s \cdot L_{eq} \cdot V_{o\%}}{n^2 \cdot \left(1 - D_{min}\right)} = 0.07\,\Omega$$
Minimum ESR

$$I_{CoRMS} := \sqrt{I_{DRMS}^2 - I_o^2} = 3.955\,A$$
RMS current value in the output capacitor

164

SOME REPRODUCED WAVEFORMS

Initializing variables for plotting

$t_{sim} := T_s \cdot \dfrac{1}{s}$ *Sampled period*

$step := 10^d$ *Step time*

$t := 0, 1 .. t_{sim} \cdot step$ *Time*

$x_t := \omega_2 \cdot \dfrac{t}{step} \cdot \dfrac{1}{\frac{rad}{s}}$ *Angular frequency w2*

$y_t := \omega_1 \cdot \left(\dfrac{t}{step} - D \cdot t_{sim} \right) \cdot \dfrac{1}{\frac{rad}{s}}$ *Angular frequency w1*

Voltage across coupling capacitance

$$V_{c_t} := \begin{cases} V_{i\_ch} + \left(V_{Cm} - V_{i\_ch} \right) \cos\left(x_t \right) + I_{L2m} \sqrt{\dfrac{L_2}{C}} \cdot \sin\left(x_t \right) & \text{if} \quad \left(0 < t < D \cdot t_{sim} \cdot step \right) \\ V_{o'\_ch} + \left(V_{CM} - V_{o'\_ch} \right) \cos\left(y_t \right) - I_{L1M} \sqrt{\dfrac{L_1}{C}} \cdot \sin\left(y_t \right) & \text{otherwise} \end{cases}$$

S on

S off

8

_____
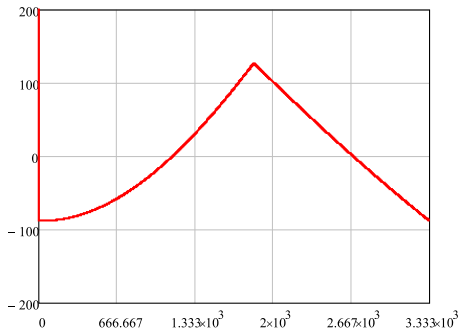
Current in the coupling capacitor

$$I_{c_t} := \left| \begin{array}{l} \sqrt{\dfrac{C}{L_2}} \cdot \left(V_{i\_ch} - V_{Cm}\right) \sin(x_t) + I_{L2m} \cdot \cos(x_t) \quad \text{if} \quad \left(0 < t < D \cdot t_{sim} \cdot \text{step}\right) \qquad \text{S on} \\ \\ \left| \sqrt{\dfrac{C}{L_1}} \cdot \left(V_{o'\_ch} - V_{CM}\right) \sin(y_t) - I_{L1M} \cdot \cos(y_t) \right| \quad \text{otherwise} \qquad \text{S off} \end{array} \right.$$
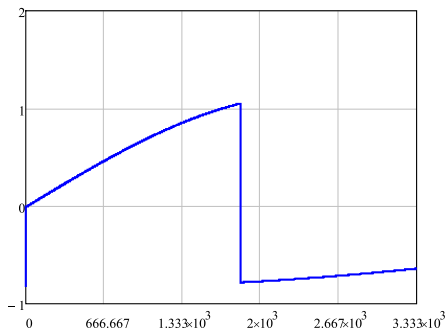
Voltage across the switch

$$V_{S_t} := \left| \begin{array}{l} 0 \quad \text{if} \quad \left(0 < t < D \cdot t_{sim} \cdot \text{step}\right) \qquad \text{S on} \\ \\ V_{i\_ch} - \left[\left(V_{CM} - V_{o'\_ch}\right) \cos(y_t) - I_{L1M} \cdot \sqrt{\dfrac{L_1}{C}} \cdot \sin(y_t) \right] \quad \text{otherwise} \qquad \text{S off} \end{array} \right.$$

Author: Glauber de Freitas Lima
March, 2019
9

166
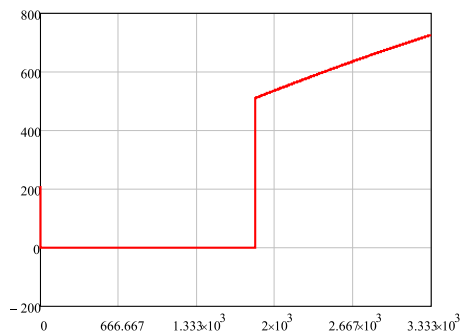
Appendix C – Magnetic Elements

Universidade Federal de Santa Catarina
Centro Tecnológico
Programa de Pós-Graduação em Engenharia Elétrica
Instituto de Eletrônica de Potência

fotovoltaicaufsc

Master's student: Glauber de Freitas Lima
Advisor: Prof. Dr. Ivo Barbi

Magnetic Elements

Calculated values | Fixed specifications* (change it iteratively whenever convinently)

DESIGN

Initial and fixed parameters

$T_a := 40 \Delta °C$ Ambient temperature

$\rho_{cu} := 2.3 \cdot 10^{-8} m \cdot \Omega$ Cupper resistivity @ 100 ºC

$K_{wL2} := 0.4$ Effecitve cupper area factor for L2 (Transformer)

$K_{wL1} := 0.7$ Effective cupper area factor for L1 (Inductor)

$K_{u2} := \dfrac{1}{1 + n \cdot \dfrac{I_{L2RMSp}}{I_{L2RMSs}}} = 0.555$ Secondary use factor (Transformer)

$J_{maxL2} := 465 \dfrac{A}{cm^2}$ Current density for L2

$J_{maxL1} := 470 \dfrac{A}{cm^2}$ Current density for L1

$\Delta B_{maxL2} := 0.1 T$ Maximum peak flux density for L2

$\Delta B_{maxL1} := 0.05 T$ Maximum peak flux density for L1

$\mu o := 4 \cdot \pi \cdot 10^{-7} \dfrac{H}{m}$ Magnetic permeability in the air

---

Product area AeAw

$AeAw_{L2} := \dfrac{(V_{o\_ch} + V_D) \cdot (1 - D) \cdot I_{L2RMSs}}{K_{wL2} \cdot K_{u2} \cdot J_{maxL2} \cdot f_s \cdot \Delta B_{maxL2}} = 0.449 \cdot cm^4$ Product area AeAw for L2

$AeAw_{L1} := \dfrac{V_{i\_ch} \cdot D \cdot I_{L1RMS}}{K_{wL1} \cdot J_{maxL1} \cdot f_s \cdot \Delta B_{maxL1}} = 0.223 \cdot cm^4$ Product area AeAw for L1

_____

Bobbin and core specification

$V_{Core} := 8.174 cm^3$ — NEE-30/15/14 Core volume

$A_e := 1.22 cm^2$ — NEE-30/15/14 Cross sectional area

$A_w := 0.85 cm^2$ — NEE-30/15/14 Bobin window area

$AeAw := A_e \cdot A_w = 1.037 \cdot cm^4$ — NEE-30/15/14 Product area

$l_{turn} := 67mm$ — NEE-30/15/14 Mean length turn

$Weight := 21g$ — NEE-30/15/14 weight

Number of turns

L2

$$N_{L2s} := floor\left[\frac{(V_{o\_ch} + V_D)(1 - D)}{A_e \cdot \Delta B_{maxL2} \cdot f_s}\right] = 7$$

Number of secondary turns:
Rounding down increase magnetic loss, but decrease cupper loss.

$$N_{L2p} := n \cdot N_{L2s} = 42$$

Number of primary turns.

$$\Delta B_{max.L2New} := \frac{(V_{o\_ch} + V_D)(1 - D)}{A_e \cdot N_{L2s} \cdot f_s} = 0.105\ T$$

New flux swing density

L1

$$N_{L1} := ceil\left(\frac{V_{i\_ch} \cdot D}{A_e \cdot \Delta B_{maxL1} \cdot f_s}\right) = 85$$

Number of turns of L1

$$\Delta B_{maxL1.New} := \frac{V_{i\_ch} \cdot D}{A_e \cdot N_{L1} \cdot f_s} = 0.04952\ T$$

New flux swing density

Air gap

L2

Adding air gap introduces reluctance much larger than core's reluctance, making L less sensible to magnetic permeability variations.

$$\delta_{gap} := \frac{\mu_0 \cdot A_e N_{L2s}^2}{\left(\dfrac{L_2}{n^2}\right)} = 0.534 \cdot mm$$

L2 total airgap.

$$l_{gap} := \frac{\delta_{gap}}{4} = 0.133 \cdot mm$$

Gap divided in "4" legs: E core

L1

$$\delta_{gapL1} := \frac{\mu_0 \cdot A_e N_{L1}^2}{L_1} = 0.307 \cdot mm$$

L1 total airgap.

2

$$l_{gapL1} := \frac{\delta_{gapL1}}{4} = 0.077 \cdot mm$$

Gap divided in "4" legs: E core

Cross sectional wire

$$\Delta := \frac{2 \cdot 7.5}{\sqrt{f_s \cdot \frac{1}{Hz}}} = 0.027$$

Diameter in cm to avoid skin effect. AWG 30 = 0.025 cm < 0.027

$$S_\Delta := 0.000509 cm^2$$

AWG 30 cupper area

$$S_p := \frac{I_{L2RMSp}}{J_{maxL2}} = 0.00149 \cdot cm^2$$

L2: Needed primary cable area to follow JmaxL2
criteria = AWG 25

$$S_s := \frac{I_{L2RMSs}}{J_{maxL2}} = 0.01114 \cdot cm^2$$

L2: Needed secondary cable area to follow JmaxL2
criteria = AWG 16

$$S_{L1} := \frac{I_{L1RMS}}{J_{maxL1}} = 0.00152 \cdot cm^2$$

L1: Needed cable area to follow JmaxL1 criteria = AWG 25

Number of conductors in parallel

$$N_{con\_L2p} := ceil\left(\frac{S_p}{S_\Delta}\right) = 3$$

L2: Number of conductors in parallel for the primary

$$N_{con\_L2s} := ceil\left(\frac{S_s}{S_\Delta}\right) = 22$$

L2: Number of conductors in parallel for the secondary

$$N_{con\_L1} := ceil\left(\frac{S_{L1}}{S_\Delta}\right) = 3$$

L1: Number of conductors in parallel

Fullfilment performance

$$S_{cu} := 0.000704 cm^2$$

AWG 30 smalted area

$$k_{uL2} := \frac{(S_{cu} \cdot N_{con\_L2p}) \cdot N_{L2p} + (S_{cu} \cdot N_{con\_L2s}) \cdot N_{L2s}}{A_w \cdot K_{wL2}} = 0.58$$

L2: Fullfiment

Desirable to be 0.3<ku<1. If is larger than 1, then
one must ajust Bmax, Jmax or choose another core
in an iterative process.

$$k_{uL1} := \frac{(S_{cu} \cdot N_{con\_L1}) \cdot N_{L1}}{A_w \cdot K_{wL1}} = 0.302$$

L1: Fullfiment

─ ─

POWER LOSS AND TEMPERATURE RISE

a) Cupper loss

$$l_{turn\_L2p} := N_{L2p} \cdot l_{turn} = 2.814\,m$$

L2: Total primary winding length

$$l_{turn\_L2s} := N_{L2s} \cdot l_{turn} = 0.469\,m$$

L2: Total primary winding length

$$l_{turn\_L1} := N_{L1} \cdot l_{turn} = 5.695\,m$$

L1: Total winding length

$$R_{L2p} := \frac{\rho_{cu} \cdot l_{turn\_L2p}}{N_{con\_L2p} \cdot S\Delta} = 0.424 \cdot \Omega$$

L2: DC primary resistance

$$R_{L2s} := \frac{\rho_{cu} \cdot l_{turn\_L2s}}{N_{con\_L2s} \cdot S\Delta} = 9.633 \times 10^{-3}\,\Omega$$

L2: DC secondary resistance

$$R_{L1} := \frac{\rho_{cu} \cdot l_{turn\_L1}}{N_{con\_L1} \cdot S\Delta} = 857.793 \cdot 10^{-3} \cdot \Omega$$

L1: DC resistance

$$P_{cuL2} := \left(R_{L2p} \cdot l_{L2RMSp}{}^2 + R_{L2s} \cdot l_{L2RMSs}{}^2 \right) = 0.461\,W$$

L2: DC Cupper loss

$$P_{cuL1} := \left(R_{L1} \cdot l_{L1RMS}{}^2 \right) = 0.439\,W$$

L1: DC Cupper loss

b) Core loss

$$K_h := 4 \times 10^{-3}$$

Histeresys loss coeficient

$$K_f := 4 \times 10^{-10}$$

Parasit current coeficient

$$P_{\Delta B.max.NewL2} := 30 \cdot 10^{-3} \frac{W}{g}$$

Magnetic loss for $\Delta B_{max.NewL2}$ OBS: Enter the curve in the catalogue using $0.5 \times \Delta B_{max.NewL2}$, therefore $0.0525\,T$

$$P_{\Delta B.max.NewL1} := 5 \cdot 10^{-3} \frac{W}{g}$$

Magnetic loss for $\Delta B_{max.NewL1}$

$$P_{CoreL2} := \frac{\left(\Delta B_{max.L2New} \right)^{2.4}}{T^{2.4}} \cdot \left[K_h \cdot \frac{f_s}{Hz} + K_f \cdot \left(\frac{f_s}{Hz} \right)^2 \right] \cdot \frac{V_{Core}}{cm^3} \cdot W = 1.756\,W$$

L2: Calculated Magnetic Loss* (Over estimated?)

$$P_{CoreCatL2} := P_{\Delta B.max.NewL2} \cdot Weight = 0.63\,W$$

L2: Magnetic loss using ferrite core datasheett

$$P_{CoreL1} := \frac{\left(\Delta B_{maxL1.New} \right)^{2.4}}{T^{2.4}} \cdot \left[K_h \cdot \frac{f_s}{Hz} + K_f \cdot \left(\frac{f_s}{Hz} \right)^2 \right] \cdot \frac{V_{Core}}{cm^3} \cdot W = 0.289\,W$$

L1: Calculated Magnetic Loss* (Over estimated?)

$$P_{CoreCatL1} := P_{\Delta B.max.NewL1} \cdot Weight = 0.105\,W$$

L1: Magnetic loss using ferrite core datasheett

4

c) Estimated efficiency

$$P_{Mag} := P_{CoreCatL2} + P_{CoreCatL1} + P_{cuL1} + P_{cuL2} = 1.635\,W$$

Estimated Power Loss in the magnetic elements

$$\eta_{Mag} := \frac{P}{P + P_{Mag}} = 0.992$$

Estimated efficiency in the magnetic elements**.** Notice the AC Loss is not being considered, which decreases efficiency largely**.**

d) Temperature rise

$$Rt_{nucleo} := 23 \cdot \left(\frac{A_e \cdot A_w}{cm^4}\right)^{-0.37} \cdot \frac{K}{W} = 22.693 \cdot \frac{K}{W}$$

Thermal resistance for $A_e \cdot A_w = 1.037 \cdot cm^4$

$$\Delta TL2 := \left(P_{cuL2} + P_{CoreCatL2}\right) Rt_{nucleo} = 24.751\,K$$

L2: Temperature variation

$$\Delta TL1 := \left(P_{cuL1} + P_{CoreCatL1}\right) Rt_{nucleo} = 12.347\,K$$

L1: Temperature variation

Appendix D – Passive Clamping Desing

Universidade Federal de Santa Catarina
Centro Tecnológico
Programa de Pós-Graduação em Engenharia Elétrica
Instituto de Eletrônica de Potência

fotovoltaicaufsc

Master's student: Glauber de Freitas Lima
Advisor: Prof. Dr. Ivo Barbi

Passive Clamping Circuit

Calculated values   Fixed specifications   Go to simulation

DESIGN

Please, for accuracy, use practical values for inductances in Appendix B - Modified Flyback Project
recalculating maximum switch current and maximum voltage across coupling capacitance.

$L_{lkpercent} := 1.468\%$

Leakage inductance percentage. Design it as low as possible!

$L_{leak} := L_{lkpercent} \cdot L_2 = 7.437 \cdot \mu H$

Leakage inductance. If high magnetizing inductance L2 is designed, the converter is inefficient. Try using u1 =u2 = 8 and Extrem Power Loss in the clamping circuit is expected

$V_{Clamp} := 1000 \cdot V$

Clampped voltage. Protect the MOSFET. High levels improves efficiency, but keep in mind that it also decreases hard switching efficiency.

$P_{g\_inf} := 0.5 \cdot L_{leak} \cdot I_{SM}^2 \cdot f_s = 3.752 \, W$

Dissipated power in the clamping circuit considering Vg infinity

$P_g := \dfrac{1}{1 - \dfrac{\left(V_{i\_ch} + V_{o'\_ch} - V_{CM}\right)}{V_{Clamp}}} \cdot P_{g\_inf} = 7.677 \, W$

Actual power dissipated. Notice, different from a conventional Flyback, V.CM must also be accounted in the equation! Notice as well, that the closer to DVM, Pg tends to dissimated only Pg_inf. The modified Flyback has, therefore, better performance regarding passive clamping circuit than its conventional one.

$R_g := \dfrac{\left(V_{Clamp} - V_{i\_ch}\right)^2}{P_g} = 67.528 \cdot k\Omega$

Resistance

$\Delta_{V\%} := \dfrac{5}{100}$

Voltage ripple across the capacitor

$Cg := \dfrac{P_g}{f_s \cdot V_{Clamp}^2 \cdot \Delta_{V\%}} = 511.767 \cdot pF$

Capacitance of the clamping circuit

$\eta_{Clm} := \dfrac{P}{P + P_g} = 0.963$

Estimated efficiency

Appendix E – Switching Element Loss

Universidade Federal de Santa Catarina
Centro Tecnológico
Programa de Pós-Graduação em Engenharia Elétrica
Instituto de Eletrônica de Potência

fotovoltaicaufsc

Master's student: Glauber de Freitas Lima
Advisor Professor: Prof. Dr. Ivo Barbi

Power Loss in the Switchg Elements

Calculated values   Fixed specifications   Go to simulation

MOSFET POWER LOSS

Used **MOSFET - CREE C2M0280120D**

Idrain = 6A@ Tc = 100 **—- Vgs** = 20V **—- RDS(on)** = 0.28O **—- VDS** = 1200V
tr = 7.6ns **-— tf** = 9.9ns

$R_{DSon} := 0.28 \cdot 1.4 \cdot \Omega = 0.392 \, \Omega$ @ Tj = 100

$t_r := 7.6 \cdot ns$ Rise time

$t_f := 9.9 \cdot ns$ Fall time

$Q_{Gtotal} := 20.4 \cdot nC$ Gate-to-source + Drain-to-source charge

$V_{Gs} := 25 \cdot V$ Gate-to-source voltage (absolute value)

$C_{oss} := 23 \cdot pF$ Output Capacitance

1) Conducting loss

$P_{con} := R_{DSon} \cdot I_{SRMS}^2 = 0.391 \, W$ Conducting Lossise time

2) Switching Loss

$P_{sw} := \dfrac{f_s}{2} \cdot \left[t_r \cdot \left(I_{SM} \cdot V_{Clamp} \right) + t_f \cdot I_{Sm} \cdot V_{SM} \right] = 2.77 \, W$

Switching loss: Considering the voltage and current excursions. Again, close to DCM or DVM, the switching loss tend to decreases as ZCS or ZVS is naturally performed. Is there a value for u1 or u2 that will have an optimimum performance?

3) Coss Loss

$P_{Coss} := \dfrac{1}{2} \cdot \left(\dfrac{V_{SM} + V_{Sm}}{2} \right)^2 \cdot C_{oss} \cdot f_s = 1.322 \, W$ Conducting Lossise time

4) Gate Driver power

$P_{Gate} := Q_{Gtotal} \cdot V_{Gs} \cdot f_s = 0.153 \, W$ Power to size gate driver

---

5) Total Mosfet loss

$$P_{MosfetLoss} := P_{con} + P_{sw} + P_{Gate} + P_{Coss} = 4.635\,W$$ Total Power Loss in the MOSFET

6) Mosfet efficiency

$$\eta_{Mosf} := \frac{P}{P + P_{MosfetLoss}} = 0.977$$ Estimated Efficiency in the MOSFET

DIODE POWER LOSS

Used **Sic Schottky INFINEON DIODE - IDH20G65C6**

If = 20A@ Tc = 135 **--- Vrrm** = 650V **--- Vf(If=20A, Tj=25)** = 1.25V

$$T_j := 40$$ Ambient Tempearature

$$X := 6.19 \cdot 10^{-7}$$ Datasheet parameter to find Forward voltage (VF) and RDiff

$$Y := 4.5 \cdot 10^{-5}$$ Datasheet parameter to find Forward voltage (VF) and RDiff

$$Z := 2.38 \cdot 10^{-2}$$ Datasheet parameter to find Forward voltage (VF) and RDiff

1) Forward Voltage and differential resistance

$$R_{Diff} := \left(X \cdot T_j^2 + Y \cdot T_j + Z \right) \cdot \Omega = 0.027\,\Omega$$ Calculated RDiff

$$V_{Th} := \left(-0.001 \cdot T_j + 0.766 \right) V = 0.726\,V$$ Calculated Vth. Interestingly, Vth decreases with the increment of temperature, therefore, increasing temperature will improve diode's efficiency.

$$V_F := V_{Th} + R_{Diff} \cdot I_o = 0.815\,V$$ Calculated Vth

2) Diode Power Loss

$$P_{DLoss} := I_o \cdot V_F + I_{DRMS}^2 \cdot R_{Diff} = 3.439\,W$$ Diode Power Loss

3) Diode Efficiency

$$\eta_{Diode} := \frac{P}{P + P_{DLoss}} = 0.983$$ Estimated Efficiency in the Diode

Author: Glauber de Freitas Lima
March, 2019

Appendix F – 1-Phase bridge rectifier

Universidade Federal de Santa Catarina
Centro Tecnológico
Programa de Pós-Graduação em Engenharia Elétrica
Instituto de Eletrônica de Potência

fotovoltaicaufsc

UNIVERSIDADE FEDERAL
DE SANTA CATARINA

Master's student: Glauber de Freitas Lima
Advisor: Prof. Dr. Ivo Barbi

Single-Phase Bridge Rectfier

Calculated values   Fixed specifications   Go to simulation

DESIGN

Used **Single-Phase 15 A GBU1506**

Io = 15 --- **Vrms** = 420V --- **Vf(If=7.5)** = 1V --- **Rja = 25ºC/W -- Rjl = 2.2ºC/W -- Tj = 150ºC**

$$\eta_{worst} := 40\%$$

Considered efficiency to design

$$P_{in} := \frac{P}{\eta_{worst}} = 500\,W$$

Bridge Recfier rated power

$$V_{ipk} := 220 \cdot \sqrt{2}V = 311.127\,V$$

Peak grid voltage

$$V_{FBrg} := 1V$$

Forward diode voltge

$$f_{grid} := 60Hz$$

Grid frequency

$$\omega := 2 \cdot \pi \cdot f_{grid} = 376.991 \cdot \frac{rad}{s}$$

Angular Grid frequency

$$\Delta V_{cIN\%} := 5 \cdot \%$$

Allowed Voltage ripple %

$$\Delta V_{cIN} := \frac{5}{100} \cdot V_{ipk} = 15.556\,V$$

Voltage ripple absolut

$$V_{cINMax} := V_{ipk} - 2 \cdot V_{FBrg} = 309.127\,V$$

Maximum input voltage

$$V_{cINMin} := V_{cINMax} - \Delta V_{cIN} = 293.571\,V$$

Minimum input voltage

$$V_{LoadAvg} := \frac{V_{cINMax} + V_{cINMin}}{2} = 301.349\,V$$

Nominal input voltage

$$R_{oBrg} := \frac{V_{LoadAvg}^2}{P_{in}} = 181.622\,\Omega$$

Reflected Resistance

$$C_{IN} := \frac{P_{in}}{2 \cdot f_{grid} \cdot \Delta V_{cIN} \cdot V_{cINMax}} = 866.451 \cdot \mu F$$

Input Capacitance

1

━━━

$C_{IN\_Market} := 3 \cdot 330 \ \mu F$

Avialable Capacitance (3 Capacitors in parallel)

$\omega CR := \omega \cdot C_{IN\_Market} \cdot R_{oBrg} = 67.785$

Pag 32 Book Projeto de Fontes Chaveadas, Ivo Barbi: To find Parameter to calculate RMS ICIN

$Parameter := 3.48$

Found parameter

$I_{CIN\_RMS} := \dfrac{1}{3} \dfrac{Parameter \cdot V_{cINMax}}{R_{oBrg}} = 1.974 \ A$

RMS in each electrolytic Capacitor

$I_{IN\_RMS} := \sqrt{\left(3 I_{CIN\_RMS}\right)^2 + \left(\dfrac{V_{cINMax}}{R_{oBrg}}\right)^2} = 6.163 \ A$

RMS Grid Current

$I_{Dbrig\_RMS} := \dfrac{I_{IN\_RMS}}{\sqrt{2}} = 4.358 \ A$

RMS current value in each diode

$I_{DBrg\_Avg} := \dfrac{V_{LoadAvg}}{R_{oBrg}} \cdot \dfrac{1}{2} = 0.83 \ A$

RMS current value in each diode

$t_c := \dfrac{acos\left(\dfrac{V_{cINMin}}{V_{cINMax}}\right)}{2 \cdot \pi \cdot f_{grid}} = 8.451 \times 10^{-4} \ s$

Conducting period

Bridge Rectfier Loss and Temperature Rise

1) Power Loss

$r_{fwdBrg} := \dfrac{(1.1 - 1) \cdot V}{(15 - 7.5) A} = 0.013 \ \Omega$

Forward resistance

$P_{DBrg} := V_{FBrg} \cdot I_{DBrg\_Avg} + I_{Dbrig\_RMS}^2 \cdot r_{fwdBrg} = 1.083 \ W$

Power dissipated in each diode

$P_{TBrg} := 4 \cdot P_{DBrg} = 4.331 \ W$

Total Power dissipated in the Bridge Rectfier

$\eta_{Brg} := \dfrac{P_{in}}{P_{in} + P_{TBrg}} = 0.991$

Estimated Efficiency in the Bridge Rectifer

$pf := \dfrac{P_{in}}{V_{in} \cdot I_{IN\_RMS}} = 0.369$

Power factor

2) Temperature Rise

$R_{ja} := 25 \cdot \dfrac{\Delta {}^\circ C}{W}$

Junction to Ambient Thermal Resistance per leg

$T_{jDBrg} := P_{DBrg} \cdot R_{ja} + \left(T_a + 273.16 \cdot \Delta {}^\circ C\right) = 67.08 \ {}^\circ C$

Junction temperature. No need for heatsink, therefore.

Discharge Resistor

$t_{Discharge} := 300 \cdot s$

Discharge time for safety

$V_{ipk} = 311.127\,V$

Conducting period

$V_{imin} := 50 \cdot V$

Minimum safe discharged

$C_{IN\_Market} = 990 \cdot \mu F$

Minimum safe discharged

$$R_{IN} := \frac{-t_{Discharge}}{\ln\left(\dfrac{V_{imin}}{V_{ipk}}\right) \cdot C_{IN\_Market}} = 1.658 \times 10^5\,\Omega$$

Resistance to discharged

$$P_{RIN} := \frac{V_i^{\,2}}{R_{IN}} = 0.527\,W$$

Dissipated power throug RIN

180

Appendix G – Heatsink, Temperature Rise and Efficiency

Universidade Federal de Santa Catarina
Centro Tecnológico
Programa de Pós-Graduação em Engenharia Elétrica
Instituto de Eletrônica de Potência

fotovoltaicaufsc

Master's student: Glauber de Freitas Lima
Advisor Professor: Prof. Dr. Ivo Barbi

Heat Sink and Overall Estimated Efficiency

Calculated values   Fixed specifications

MOSFET Heatink and Temperature Rise

Temperature disspipation is analgous to an electric circuit as shown in ----->
The initial step is to define a heatsink maximum temperature heatsink temperature

$T_a = 40 \cdot \Delta°C$ Ambient temperature

$T_d := 60 \Delta°C$ Heatsink temperature

$\Delta T_{d\_a} := T_d - T_a = 20 \cdot \Delta°C$ Temperature variation between ambient and heatsink.
It has to do with dissipation efficiency for 60ºC

$FC := 1.257$ Correcting factor for temperature variation
according to datasheet

$FS := 1.5$ Safe factor to apply.

$P_{MosfetLoss} = 4.635\ W$ Mosfet Power Loss dissipated in
heatsink

$R_{da\_Mosfet} := FC \cdot \dfrac{T_d - T_a}{FS\ P_{MosfetLoss}} = 3.616 \cdot \dfrac{\Delta°C}{W}$ Heatsink thermic resistance calculated.

$R_{da\_Hs} = 2.92\ \dfrac{\Delta°C}{W}$ Thermic resistance of Heatsink from HS,
HS-15559, considering 4"

$CC := 1.43$ Factor to correct to real size 5 cm

$R_{da\_Hs\_real} := CC \cdot R_{da\_Hs} = 4.176 \cdot \dfrac{\Delta°C}{W}$

Código: HS 8620

Perímetro: 530 mm
Resistência Térmica: 2,92 ℃ / W / 4"

As the chosen heatsink thermic resistance (Rda_Hs_real) is < Calculated value (Rda) , then it is meets requiremente. Otherwise,
chosse another Heatsink or Forced ventilation.

$T_{Hs} := T_a + R_{da\_Hs\_real}\ P_{MosfetLoss} = 59.356 \cdot \Delta°C$ Temperature in the Heatsink

Verify Junction and Case temperature

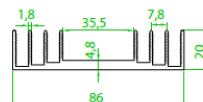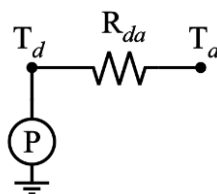$R_{jc\_MOSFET} := 2\ \dfrac{\Delta°C}{W}$ Thermic resistance JC $R_{cd\_mica} := 1\ \dfrac{\Delta°C}{W}$ Thermic resistance of mica

$T_{c\_MOSFET} := T_{Hs} + R_{cd\_mica} \cdot P_{MosfetLoss} = 63.991 \cdot \Delta°C$ Case Temperature MOSFET

$T_{j\_MOSFET} := T_{c\_MOSFET} + R_{jc\_MOSFET} \cdot P_{MosfetLoss} = 73.262 \cdot \Delta°C$ Junction Temperature MOSFET

Diode Heatink and Temperature Rise

Temperature disspipation is analgous to an electric circuit as shown in --->
The initial step is to define a heatsink maximum temperature heatsink temperature

$T_a = 40 \cdot \Delta°C$ — Ambient temperature

$T_d = 60 \cdot \Delta°C$ — Desired Heatsink temperature

$\Delta T_{d\_a} = 20 \cdot \Delta°C$ — Temperature variation between ambient and heatsink. It has to do with dissipation efficiency for 60ºC

$FC = 1.257$ — Correcting factor for temperature variation according to datasheet

$FS = 1.5$ — Safe factor to apply.

$P_{DLoss} = 3.439\,W$ — Mosfet Power Loss dissipated in heatsink

$R_{da\_Diode} := FC \cdot \dfrac{T_d - T_a}{FS\, P_{DLoss}} = 4.874 \cdot \dfrac{\Delta°C}{W}$ — Heatsink thermic resistance calculated.

$R_{da\_Hs} = 2.92 \cdot \dfrac{\Delta°C}{W}$ — Thermic resistance of Heatsink from HS, HS-15559, considering 4"

$CC = 1.43$ — Factor to correct to real size 5 cm

$R_{da\_Hs\_real} = 4.176 \cdot \dfrac{\Delta°C}{W}$

Código: HS 8620

Perímetro: 530 mm
Resistência Térmica: 2,92 ℃ / W / 4"

As the chosen heatsink thermic resistance (Rda_Hs_real) is < Calculated value (Rda) , then it is meets requiremente. Otherwise, chosse another Heatsink or Forced ventilation.

$T_{Hs} := T_a + R_{da\_Hs\_real} \cdot P_{DLoss} = 54.359 \cdot \Delta°C$ — Temperature in the Heatsink

Verify Junction and Case temperature

$R_{jc\_Diode} := 1.3 \dfrac{\Delta°C}{W}$ — Thermic resistance JC
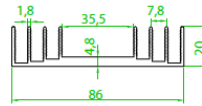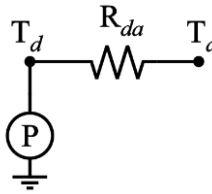
$R_{cd\_mica} = 1 \cdot \dfrac{\Delta°C}{W}$ — Thermic resistance of mica

$T_{c\_Diode} := T_{Hs} + R_{cd\_mica} \cdot P_{DLoss} = 57.798 \cdot \Delta°C$ — Diode Case Temperature

$T_{j\_Diode} := T_{c\_Diode} + R_{jc\_Diode} \cdot P_{DLoss} = 62.269 \cdot \Delta°C$ — Diode JunctionTemperature

Total Efficiency

Estimated total efficiency will account all power loss so far.

$P_{CouplingCLoss} := 2 \cdot 1 \cdot \Omega \cdot I_{CRMS}{}^2 = 0.955\,W$ — Estimated Coupling Capacitors power Loss

$P_{TotalLoss} := P_{Mag} + P_g + P_{MosfetLoss} + P_{DLoss} + P_{TBrg} + P_{RIN} + P_{CouplingCLoss} = 23.198\,W$ — Total Power Loss

$\eta_{Global} := \dfrac{P}{P_{TotalLoss} + P} = 0.896$ — Estimated Global Efficiency

Author: Glauber de Freitas Lima
March, 2019

Appendix H – Gate Driver Desing

Universidade Federal de Santa Catarina
Centro Tecnológico
Programa de Pós-Graduação em Engenharia Elétrica
Instituto de Eletrônica de Potência

fotovoltaicaufsc

Master's student: Glauber de Freitas Lima
Advisor Professor: Prof. Dr. Ivo Barbi

GATE DRIVER

Calculated values   Fixed specifications

Fixed parameters

MOSFET - **CREE C2M0280120D**

Idrain = 6A@ Tc = 100 --- **Vgs** = 25V
VDS = 1200V --**tr** = 7.6s --- **tf** = 9.9ns

$t_r = 7.6 \cdot ns$ — rise time given in datasheet

$t_f = 9.9 \cdot ns$ — fall time given in datasheet

$Q_{Gtotal} = 20.4 \cdot nC$ — Gate charge

$V_{Gs} = 25\,V$ — Absolute VGS

$C_G := \dfrac{Q_{Gtotal}}{V_{Gs}} = 816 \cdot pF$ — Gate Capacitance

$V_{Gsp} := 20 \cdot V$ — Positive voltage

$V_{Gsn} := -5 \cdot V$ — Negative voltage

$R_{Gin} := 11.4\Omega$ — Inner gate resistance

$C_{rss} := 3pF$ — Reverse Transfer Capacitance

$C_{iss} := 259pF$ — Reverse Transfer Capacitance

$V_{th} := 2.6V$ — Threshold Voltage

$I_{GH.Capable} := \dfrac{Q_{Gtotal}}{t_r} = 2.684\,A$ — Gate driver must be able to supply this current during turn-ON

$I_{GL.Capable} := \dfrac{Q_{Gtotal}}{t_f} = 2.061\,A$ — Gate driver must be able to supply this current durring turn-OFF

$f_s = 300 \cdot KHz$ — switching frequency

Single Channel Mosfet Gate Driver IC DRIVER **-1EDI60N12AF**

Iout+Peak = 10 A Typ --- **Iout-Peak** = 9.4 A Typ --> at Vcc =15 V

$R_{DH} := 1.4 \cdot \Omega$ — Output source resistance

$R_{DL} := 1.7 \cdot \Omega$ — Output sink resistance

$V_{cc1} := 5 \cdot V$ — Input signal voltage

$I_{Q1} := 1 \cdot mA$ — Maximum Quiescent input current

$I_{Q2} := 2 \cdot mA$ — Maximum Quiescent output curent

$Q_{int} := 1 \cdot nC$ — Considered internal gate charge of the IC

$R_{JA} := 165 \cdot \dfrac{K}{W}$ — Positve voltage

184

Gate Driver Design

$R_{GH} := 0.1 \cdot \Omega$ High Gate resistance +. This resistance was set low due to the high inner gate resistance

$R_{GL} := 0.1 \cdot \Omega$ Low Gate resistance -. This resistance was set low due to the high inner gate resistance

$t_{riseCalculated} := \dfrac{R_{GH} + R_{DH} + R_{Gin}}{V_{Gs}} \cdot Q_{Gtotal} = 10.526 \cdot ns$ rise time calculated

$t_{fallCalculated} := \dfrac{R_{GL} + R_{DL} + R_{Gin}}{V_{Gs}} \cdot Q_{Gtotal} = 10.771 \cdot ns$ fall time calculated

$R_{TotalLow} := R_{GL} + R_{DL} + R_{Gin} = 13.2\,\Omega$ Total equivalent resistance LOW

$R_{GtotalMax} := \dfrac{V_{th}}{C_{rss} \cdot \dfrac{V_{SM}}{t_{riseCalculated}}} = 12.555\,\Omega$

Maximum total gate resistance to avoid self-turn on. Notice it is less than RTotalLow, but in practice t.rise is larger and self-turn on might not occur. Regardless, there is not much that can ben done here, since the gate resistance combined with other ESR is already too large. The self-turn on is extremely harmful in half-bridge and H-bridge structures or, in the case of a DC-DC converter, synchronous rectification!

$I_{GH.peak} := \dfrac{Q_{Gtotal}}{t_{riseCalculated}} = 1.938\,A$ High Peak current calculated

$I_{GL.peak} := \dfrac{Q_{Gtotal}}{t_{fallCalculated}} = 1.894\,A$ Low Peak current calculated

$P_{GatePout} := f_s \cdot Q_{Gtotal} \cdot V_{Gs} = 153 \cdot mW$ Total Power Gate Driver delivered: half to charge Mosfet Capacitance and half power dissipated.

$P_{D\_RGH} := \dfrac{1}{2} \cdot f_s \cdot Q_{Gtotal} \cdot V_{Gs} \cdot \left(\dfrac{R_{GH}}{R_{DH} + R_{GH} + R_{Gin}} \right) = 0.593 \cdot mW$ Power dissipated through High Gate resistor

$P_{D\_RGL} := \dfrac{1}{2} \cdot f_s \cdot Q_{Gtotal} \cdot V_{Gs} \cdot \left(\dfrac{R_{GL}}{R_{DL} + R_{GL} + R_{Gin}} \right) = 0.58 \cdot mW$ Power dissipated through Low Gate resistor

$P_{D\_RDH} := \dfrac{1}{2} \cdot f_s \cdot Q_{Gtotal} \cdot V_{Gs} \cdot \left(\dfrac{R_{DH}}{R_{DH} + R_{GH} + R_{Gin}} \right) = 8.302 \cdot mW$ Power dissipated through High Driver resistor

$P_{D\_RDL} := \dfrac{1}{2} \cdot f_s \cdot Q_{Gtotal} \cdot V_{Gs} \cdot \left(\dfrac{R_{DL}}{R_{DL} + R_{GL} + R_{Gin}} \right) = 9.852 \cdot mW$ Power dissipated through Low Driver resistor

$P_{G\_RGin} := \dfrac{1}{2} \cdot f_s \cdot Q_{Gtotal} \cdot V_{Gs} \cdot \left(\dfrac{R_{Gin}}{R_{DH} + R_{GH} + R_{Gin}} + \dfrac{R_{Gin}}{R_{DL} + R_{GL} + R_{Gin}} \right) = 133.673 \cdot mW$

Power dissipated through inner gate resistance. Notice, due to the high resistance, most power is disspated in the MOSFET! Be aware!

$P_{ICDriver} := V_{cc1} \cdot I_{Q1} + V_{Gs} \cdot I_{Q2} + f_s \cdot Q_{int} \cdot V_{Gs} + P_{D\_RDH} + P_{D\_RDL} = 80.655 \cdot mW$ ICDriver must handle this power

$P_{GatePin} := P_{ICDriver} + P_{G\_RGin} + P_{D\_RGL} + P_{D\_RGH} = 215.5 \cdot mW$ Total Power Gate Driver: Specify the DC-DC voltage supply for this Power/Ef of the dc-dc

$\Delta T_{IC} := R_{JA} \cdot P_{GatePin} = 35.557\,K$ Rise temperature variation. In an ambient temperature of 40ºC => T = 75ºC, Tj maximum is 150ºC. Beware of maximum power in the IC Gate Driver, as maximum frequency can be limited by Maximum Power dissipation, which is at 400 mW
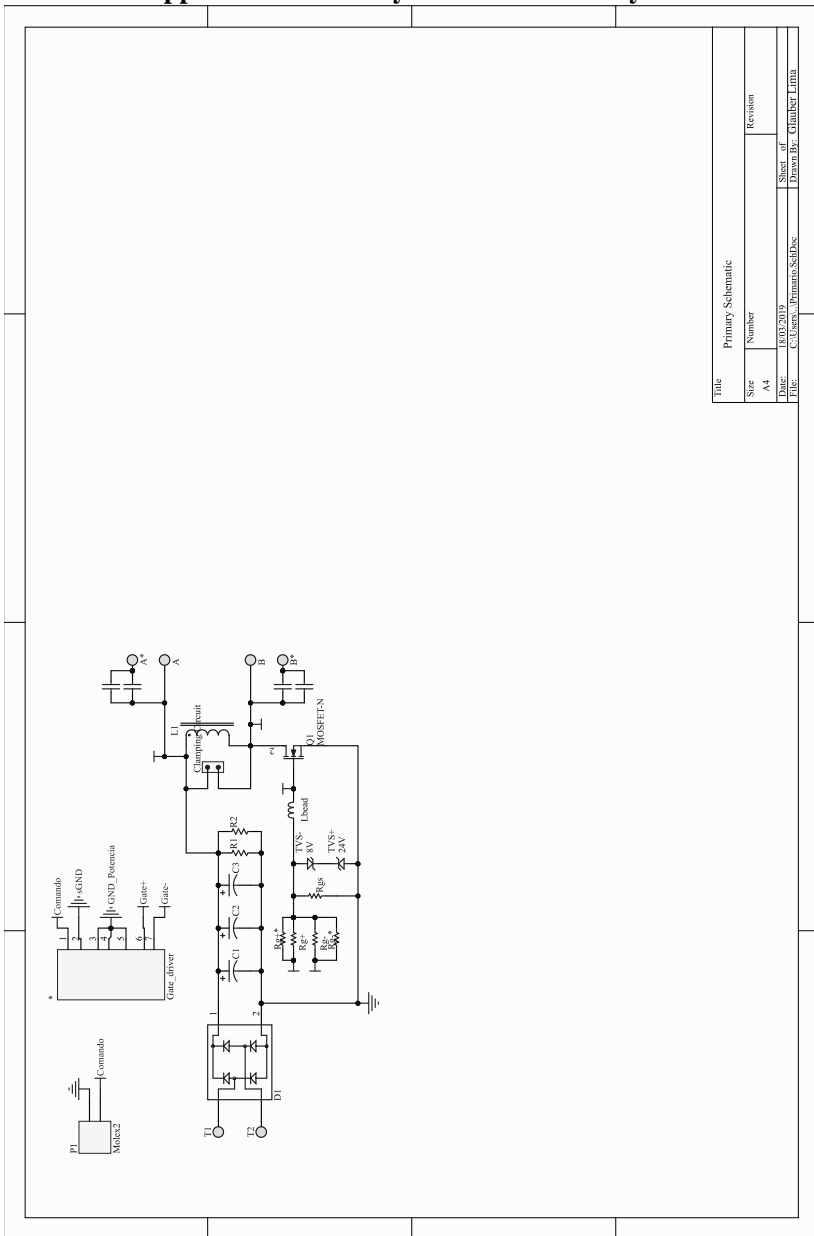
Isolated DC-DC Voltage Supply **MURATA DC DC CONVERTER MGJ2D152005SC**

V+ = 20 V –•- **V-** =-5V –•- **P** = 2W –•- **Ef** = 81%

$$C_{Bypass} := \frac{I_{Q2} \cdot \frac{D}{f_s} + Q_{Gtotal}}{0.1\% \cdot V_{Gs}} = 0.963 \cdot \mu F$$
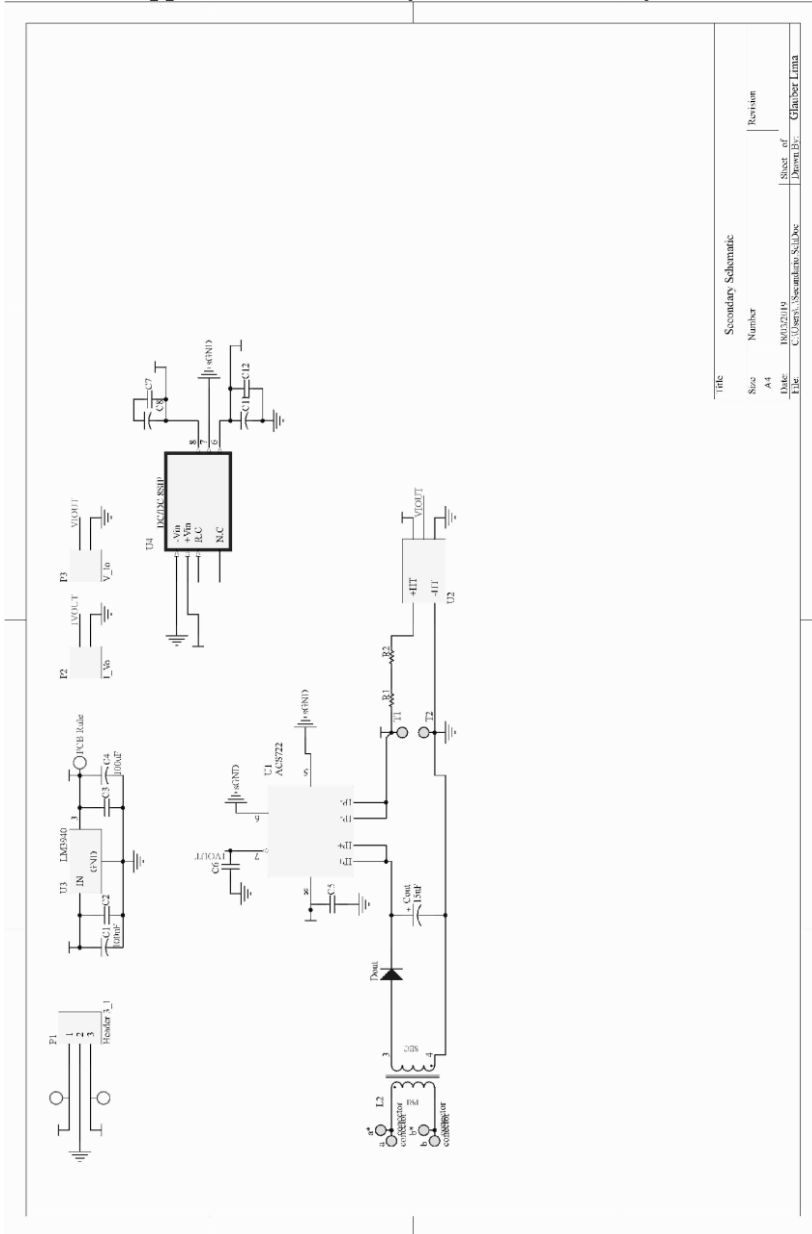
Capacitance to maintain constant voltage

Appendix I – Primary Schematic and Layout
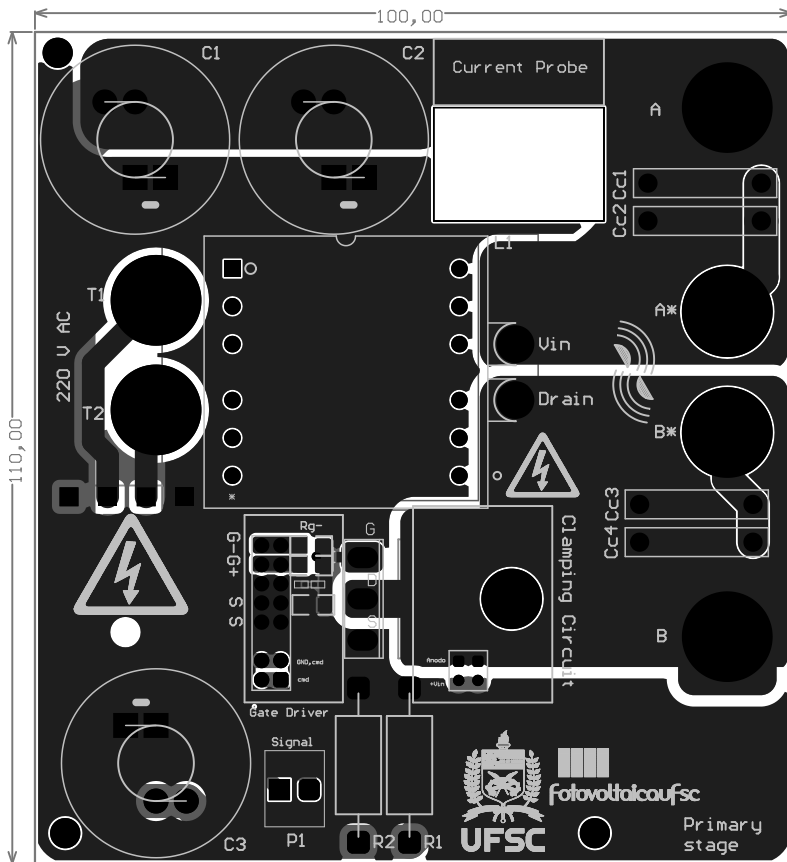
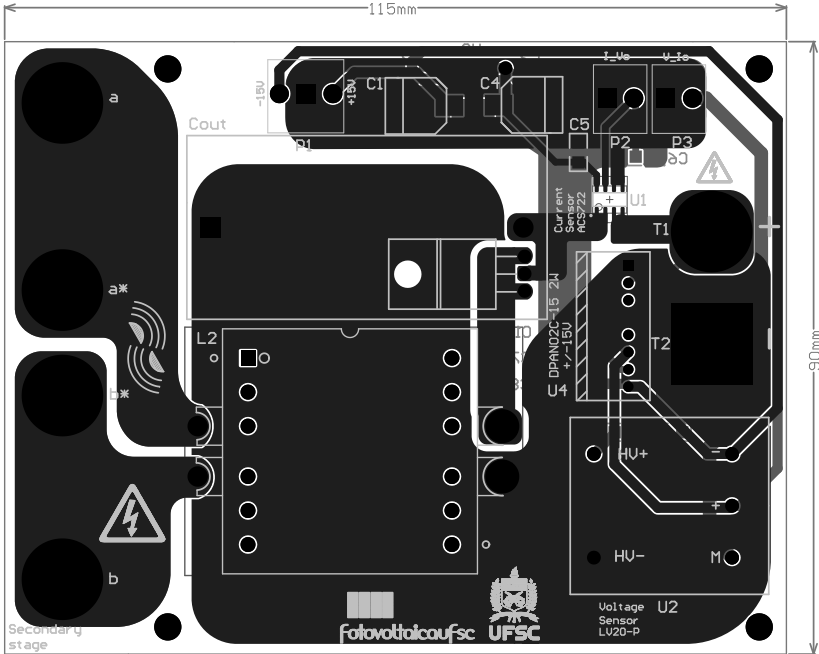# Appendix J – Secondary Schematic and Layout

Appendix K – Gate driver Schematic and Layout
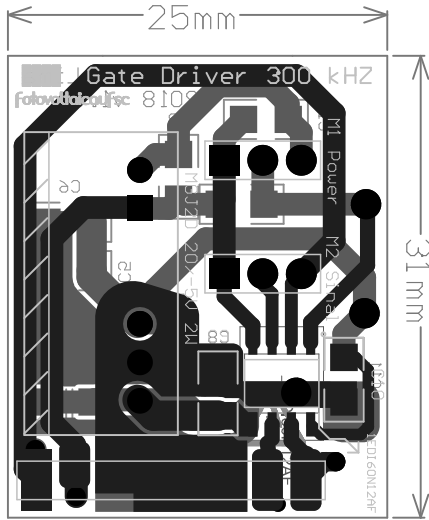
Appendix L – Clamping circuit Schematic and Layout
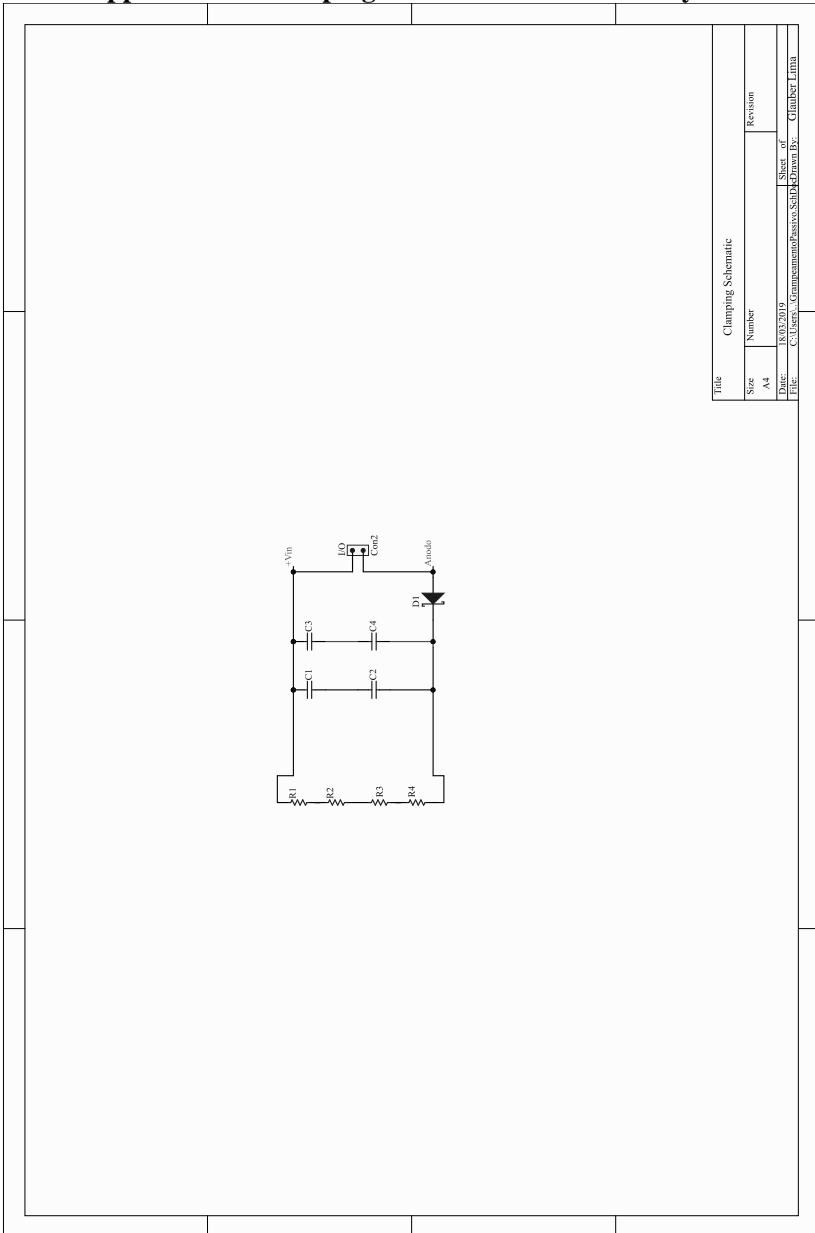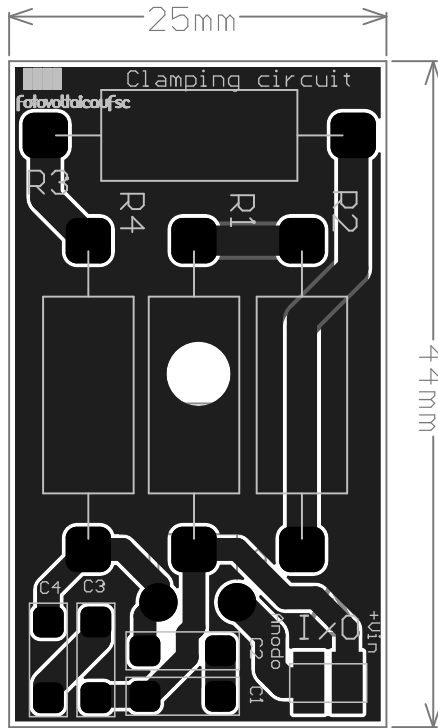
Appendix M – Bill of material

BILL OF MATERIAL

Category	PRODUTO	BRAND	Needed for one Prototype	Amount acquired	Prince in Dollar	Total DOLAR	Store	Part Number
Switch	MOSFET SIC CREE C2M0280120D N-CH 1200V 10A	CREE	1	6	7,12	42,72	DIGIKEY	C2M0280120D-ND
Capacitors Cr, Cg, Cce e Co	CAPACITOR ELETROLITICO LLS2V331MELA 330uF 20% 350VDC	Nichicon	3	6	3,98	23,88	DIGIKEY	493-6175-ND
	CAPACITOR FILME 1000pF B32529C8102J000 0.1uF 5% 630VDC	EPCOS (TDK)	2	10	0,32	3,20	DIGIKEY	495-1255-ND
	CAPACITOR FILME 10000pF R76TN3100SE40K 0.01uF 5% 700VAC	EPCOS (TDK)	2	10	0,59	5,89	DIGIKEY	495-3232-ND
	CAPACITOR FILME 15uF C4GADUDS150AA11 15uF 5% 250VDC	KEMET	1	2	7,06	14,12	DIGIKEY	399-13088-ND
Sensors	SENSOR CORRENTE ACS722 10 DC	Allegro MicroSystems	1	3	5,54	16,62	DIGIKEY	620-1636-1-ND
	SENSOR TENSÃO LEM LV 20-P	LEM	1	2	45,54	91,08	DIGIKEY	LV 20-P
Bridge Rectifier, Dg e D	BRIDGE RECTIFIER GBU1510TB 15A 600V	SMC Diode Solutions	1	5	1,05	5,25	DIGIKEY	1655-1845-ND
	Diodo SCHOTTKY 1.2KV 1A Grampeamento	GeneSiC Semic.	1	3	3,75	11,25	DIGIKEY	1242-1125-ND
	DIODE SCHOTTKY 650V 41A TO220-2	Infineon Technologies	1	3	8,43	25,29	DIGIKEY	IDH20G65C6XKSA1-ND
	Diode Schottky 200V 15A TEM	Taiwan Semic. Corp.	1	5	1,58	7,90	DIGIKEY	TST30H200CWCQG-ND
GATE DRIVER	Gate Driver IC IGBT DVR 1200V DSO8	Infineon Technologies	1	5	2,33	11,65	DIGIKEY	1ED160N12AFXUMA1CT-ND
	MURATA DC DC CONVERTER 20V -5V 2W	Murata Power Solutions Inc.	1	2	8,46	16,92	DIGIKEY	811-3006-5-ND
	TVS DIODE 24V 50V SLP1006P2T	Semtech Corporation	1	3	1,25	3,75	DIGIKEY	RCLAMP2431TQTCTCT-ND
	TVS DIODE 8V 25V SLP1006P2	Semtech Corporation	1	3	0,95	2,85	DIGIKEY	RCLAMP0821P1TCTCT-ND
	3.3 Ohms ±5% 1W Through Hole	Yageo	1	25	0,11	2,66	DIGIKEY	3.3WCT-ND
	7.5 Ohms ±5% 1W Through Hole	Yageo	1	25	0,13	3,27	DIGIKEY	7.5WCT-ND
	Zener Diode 30V 1W ±5% Surface Mount	Diodes Incorporated	1	10	0,40	3,97	DIGIKEY	SMAZ30-FDICT-ND
	1µF ±10% 100V Ceramic Capacitor X7R 1206	TDK Corporation	1	100	0,24	23,68	DIGIKEY	445-4467-1-ND
	0.1µF ±10% 100V Ceramic Capacitor 1206	KEMET	1	100	0,12	12,22	DIGIKEY	399-1805-1-ND
	IC GATE AND 1CH 2-INP SOT23-5	Texas Instruments	1	3	0,43	1,29	DIGIKEY	296-1113-1-ND
					Total	329,46		